The Dissertation Committee for Jong Yeon Park Certifies that this is the approved version of the following dissertation:

Wavelength Selective and 3D Stacked Microbolometers For Multispectral Infrared Detection

Committee:

Dean P. Neikirk, Supervisor

Ananth Dodabalapur

Seth Bank

Neal Hall

Li Shi

WAVELENGTH SELECTIVE AND 3D STACKED MICROBOLOMETERS FOR MULTISPECTRAL INFRARED DETECTION

by

JONG YEON PARK, B.E., M.E.

DISSERTATION

Presented to the Faculty of the Graduate School of

The University of Texas at Austin

in Partial Fulfillment

of the Requirements

for the Degree of

DOCTOR OF PHILOSOPHY

The University of Texas at Austin

May 2012

Dedication

This dissertation is dedicated to my parents, my beloved wife,
Heejin and my lovely daughter, Celine
for their patience, support, and love.

Acknowledgements

It is difficult to acknowledge all those people who make a dissertation such as this possible. First and foremost I would like to deepest appreciation to my advisor, Dr. Dean P. Neikirk, for providing me the opportunity to pursue this research under his creative guidance and warmly support over the years as a member of "Team Neikirk". It would have been very difficult to find a person with whom I could have worked better.

I would like to acknowledge the committee members of my dissertation, Dr. Ananth Dodabalapur, Dr. Seth Bank, Dr. Neal Hall and Dr. Li Shi. I also appreciate the members of Team Neikirk, Dr. Praveen Pasupathy (special thanks to valuable technical discussion and friendship), Sheng Zhang, Ye Chen, Hoo Kim, Tanuj Trivedi, and former group members, Dr. Junwan Kim and Dr. Jooyun Jung. I would like to thank Prof. James Gardner, Junghwan Yum and Dr. Ji Won Suk for providing device characterization equipments and technical discussion. I would like to special thank Prof. Sang Young Son (University of Cincinnati) and Prof. Deok Ho Kim (University of Washington at Seattle) for providing smart answers, encouragement and friendship and I'm also express my appreciation and gratitude to all my friends (special thank to KW Yang and BT Kim).

I would like to deeply appreciation to my parents for their continued enthusiastic support, and finally, to my beloved wife, Heejin and my lovely daughter, Celine for their invaluable support, patience and love.

This research supported by US Army ARDEC.

Wavelength Selective and 3D Stacked Microbolometers For Multispectral Infrared Detection

Jong Yeon Park, Ph.D.

The University of Texas at Austin, 2012

Supervisor: Dean Paul Neikirk

Development of wavelength selective detection, tunable multi-spectral capability with functionality in the infrared spectral region is highly desirable for a variety of applications such as thermography, chemical processing and environmental monitoring, spectroradiometry, medical diagnosis, Fourier transform infrared spectroscopy, night vision, mine detection, military defense and astronomy. Infrared detector with wavelength selective functionality have emerged as next generation infrared detectors.

This study presents fabrication and characterization of wavelength selective Germanium dielectric coated Salisbury screen and novel 3D stacked microbolometer for multispectral infrared detection. This novel fabrication process helps produce much flatter, more robust device structure by using an un-patterned sacrificial layer to produce device legs that hold the central structural layer above the reflective mirror supported by a completely flat sacrificial layer with sufficient thermal isolation to allow microbolometer operation. For the fabricated wavelength selective Germanium dielectric coated Salisbury screen microbolometer using self aligned process, the FTIR measured spectral responses and numerical simulation results show excellent agreement with wavelength selectivity (9μm, 10μm, 11μm) in long wave infrared (LWIR) region.

To achieve multicolor infrared detection, recently a few device concepts using uncooled detectors have been reported. However, none of the proposed device designs have demonstrated fabrication. Moreover, Commercial Fabry-perot resonant cavity based uncooled microbolometers (Air gap: 2 to 2.5μm) have limited design parameters due to multicolor narrow band spectral response. In this study, a feasible device fabrication method for novel 3D stacked microbolometer is demonstrated for multispectral uncooled infrared detector that can achieve tunable narrowband absorption in mid-wave infrared (MWIR) and long-wave infrared (LWIR) spectral regions.

Table of Contents

List of Tables

List of Figures

Chapter 1: Introduction

The infrared detection technologies for thermal imaging have been the subject of research and development for many decades in a wide variety of different applications.

Infrared focal plane arrays (FPAs) are now fast emerging in military, civilian, scientific and medical applications such as defense, security and surveillance, medical thermography and diagnosis, building diagnostics, environmental and chemical process monitoring, forensic drug analysis, microscopy, mine detection, Fourier transform infrared spectroscopy, spectroradiometry, astronomy, night vision in vehicles, and industrial thermography (e.g., microelectronics: inspection of microchip and circuits, electrical and mechanical equipment fault detection) [1].

Currently, developing of infrared detection for enhanced capabilities such as high thermal resolution, wavelength selective detection, tunable multispectral functionality in the infrared spectral region would be highly desirable for a variety of applications. This capability has emerged as a next generation infrared detectors [2].

The infrared detectors are typically divided into two principally different devices: thermal detectors and photon detectors. In contrast to photon detectors, which are sensitive only to wavelengths shorter than the cutoff, the widely used thermal detector is the uncooled microbolometer, which is sensitive to all wavelengths. The absorption of incident infrared radiation raises the temperature of the device, which can be result in a change in a temperature-dependent parameter such as electrical conductivity.

As a consequence, the output of a conventional uncooled microbolometer is usually proportional to the amount of energy absorbed per unit time by the detector and,

provided the absorption efficiency is same for the all wavelengths, is independent of the wavelength of the light. In addition, dark current does not limit thermal detectors. Therefore, microbolometer can be operated inexpensively at room temperature. Uncooled microbolometer focal plane arrays have significant weight, power and cost advantages over cooled infrared focal plane arrays which allows for compact infrared detector system designs [3].

Currently, in the development of multispectral infrared detector systems, narrow bandwidth absorption for infrared wavelength selectivity can be achieved using infrared photon detectors such as HgCdTe (Mercury Cadmium Telluride: MCT) photodiodes, quantum well infrared photodetectors (QWIPs), strained layer super lattices (SLs), and quantum dot infrared photodetectors (QDIPs)[4].

However, photon detectors typically require cryogenic cooling systems. Since these quantum detectors use intrinsic photoelectric effect, the materials of a quantum detector respond to infrared by absorbing photons that elevate the electrons to a higher energy state, causing a change in conductivity, current or voltage. By cooling down the quantum detector to a certain cryogenic temperature, quantum detectors can be made very sensitive to the infrared. The reason is that when a quantum detector's material cooled to a low temperature, the thermal energy of the electrons may be too low such that there are no electrons in the conduction band. Therefore the material cannot carry any current. When detectors have incident photons, this energy can stimulate an electron in the valence band to move to the conduction band.

Another common method uses classical optical techniques, such as either dispersing the optical signal across multiple infrared focal plane arrays (FPAs) or a filter wheel to spectrally discriminate the image focused on a single infrared focal plane array (FPA). These systems use optical components such as bandpass filters, grating, lenses,

and beam splitters in the optical path to focus the images onto separate focal plane arrays responding to multispectral infrared [5].

By using a conventional uncooled microbolometer based on a simple Fabry-Perot cavity structure, wavelength selectivity in infrared spectral region is hard to achieve, since a simple Fabry-Perot microbolometer typically produces a fairly broad spectral response in long wavelength infrared region (LWIR, 8μm to 12 μm).

In this study, we present narrow bandwidth absorption for wavelength selectivity in infrared spectral region using wavelength selective Germanium dielectric coated Salisbury screen microbolometers and novel 3D stacked microbolometer. This device should enable efficient multi-color infrared uncooled microbolometer focal plane arrays.

Chapter 2 describes background and motivation of research. The fundamentals of infrared radiation, theory of conventional infrared detectors and application of infrared detector technologies for thermal imaging, background and theory of uncooled infrared microbolometers, as well as multispectral infrared detection for research motivation are reviewed.

Chapter 3 describes fabrication of wavelength selective Germanium dielectric coated Salisbury screen microbolometers. In this chapter, the process for polyimide as sacrificial layer, Germanium dielectric structural layer, air gap formation using oxygen plasma ashing, electrical contact pads and self align methods are presented in detail.

Chapter 4 discusses the measurement results. For the device characterization, 3D optical surface profiles to evaluate air gap device structure, spectral responses using Fourier transform infrared (FTIR) spectrometer with focusing systems and electrical measurements are performed.

Chapter 5 present novel 3D stacked microbolometer for two color infrared detection. Fabrication methods capable of 3D stacked microbolometer and simulation results for device design enabling to two color detection in mid wavelength infrared (MWIR) and long wavelength infrared (LWIR), are described.

Chapter 6 concludes the dissertation with a summary of the achievements of this research and presents ideas for future work in this area.

Chapter 2: Background and Motivation

In this chapter, fundamentals of infrared radiation, theory of conventional infrared detectors and its applications, and motivation of research based on multispectral infrared detection for the advanced infrared detectors are covered.

2.1 INFRARED RADIATION

"INFRA" from the Latin prefix means beneath or below and infrared refers to the region beyond the visible spectral region. Infrared radiation was discovered in 1666 by Issac Newton, when he separated the electromagnetic energy form sunlight by passing light through a prism that separated the beam into rainbow colors. Sir William Herschel measured the relative energy of color using a prism and thermometers in 1800. He found that thermometer temperature increased from above the violet color to under the red color. He concluded that invisible light must be related between wavelength and temperature and energy of light beyond the red color does indeed exist. This energy would eventually be called the infrared [6].

Kirchhoff (Kirchhoff's law, 1859), Wilhelm Wien (Wien's displacement law, 1893), Stefan and Boltzmann, (Stefan-Boltzmann law, 1897), and Plank (Plank's radiation law, 1900) much further investigated the electromagnetic spectrum activities and developed equations to define infrared [7].

Infrared is electromagnetic radiation with a wavelength between 0.3 and 300μm which equates to approximately 1 to 430 THz in frequency range. Infrared wavelengths can be classified into several categories. Visible and short wavelength infrared (near infrared, NIR or SWIR: 0.35 to 2.5μm spectral region) corresponds to a band of light atmospheric transmission and peak solar illumination, yielding detectors with the best

clarity and resolution of the three bands. Without moonlight or artificial illumination, however, SWIR imagers provide poor or no imagery of objects at 300K. The mid-wave infrared band (MIR or MWIR: 3 to 5 μm spectral region) can be almost transmitted with the added background noise, lower, ambient benefits. The long wavelength infrared band (LWIR: 8 to 12 μm spectral region) can be nearly transmitted and it also offers excellent visibility regarding to terrestrial objects.

Figure 2.1 shows atmospheric attenuation in the infrared spectral regions (NIR, SWIR, MWIR, and LWIR). Between the infrared detector system and the object is the atmosphere which tends to attenuate radiation because of scattering by particles as well as absorption by gases.

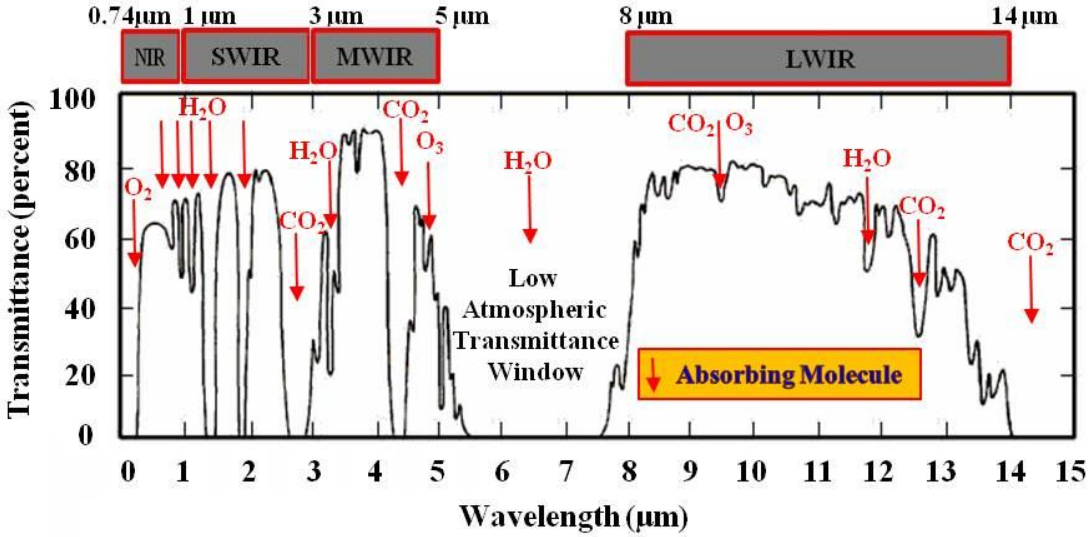

Figure 2.1: Atmospheric attenuation in the infrared spectral region. The area under the curve shows the highest infrared transmittance. Atmospheric attenuation prevents an object's total radiation from the reaching the infrared detector [8].

2.2 FUNDAMENTALS OF INFRARED RADIATION

Every single object whose temperature is not absolute zero (the theoretical temperature at which entropy reaches its minimum value: 0K on the Kelvin scale and 273.15° on the Celsius scale) emits, which is defined "thermal radiation". Thermal radiation at terrestrial temperatures consists of self emitted radiation from vibrational and rotational quantum energy level transitions in molecules, and reflection of radiation from the heated sources.

The intensity of the emitted energy from an object varies with radiation wavelength and temperature. Total radiation law can be simplified to $\alpha + \rho + \tau = 1$, where α = absorptance, ρ = reflectance, τ = transmittance. If there is no transmitted or reflected radiation and all incident radiation is absorbed it is defined a perfect blackbody.

A perfect blackbody is an idealization and it can emit and absorb the maximum theoretical amount of thermal radiation at a given temperature. Fundamentals of blackbody can be described by Kirchhoff's law. According to Kirchhoff's law, α (absorptance) = ε (emissivity) and both values vary with the radiation wavelength, $\alpha(\lambda, T) = \varepsilon(\lambda, T)$.

The amount of radiation power properties from a perfect black body will follow Planck's radiation law, which can described the radiation power intensity of a perfect blackbody at certain temperature as a function of wavelength or frequency.

$$M_\lambda(\lambda, T) = \frac{2\pi hc^2}{\lambda^5[e^{hc/\lambda kT} - 1]}[W/cm^2 - \mu m] \qquad \text{Eq. 2.1}$$

where

M: Spectral radiant exitance

λ: Wavelength;

T: Absolute temperature in Kevin [K];

c: Speed of light in a vacuum = 2.998 x 10^{10} cm/s;

h: Planck's constant=6.626 x 10^{-34}Js;

k: Boltzmann's constant=1.3807 x 10^{-23}J/K.

From Plank's radiation law, the total radiated power energy from a backbody at temperature T is the integral over all wavelengths. This result is the Stefan-Boltzmann law;

$$M(T) = \int_0^\infty M_\lambda(\lambda, T) d\lambda = \sigma T^4 [W / m^2] \qquad \text{Eq. 2.2}$$

where

M: Total exitance

σ: Stefan-Boltzmann's constant=5.6696 x 10^{-8} W/m^2;

T: Absolute temperature in Kevin [K].

The decrease in the wavelength of peak exitance as the temperature increases is quantified in the Wien Displacement law and can be expression for the wavelength of maximum exitance at certain temperature.

$$\lambda_{\max} = \frac{2898 \mu m K}{T} \qquad \text{Eq.2.3}$$

where

λ_{max}: Wavelength of maximum radiation [μm];

T: Absolute temperature in Kevin [K].

2.3 INFRARED DETECTORS

There are two fundamental methods of infrared detector: thermal detection and photon detection. Thermal detection mechanism is where the radiation incident on a thermal detector causes the detector temperature to increase due to absorbed radiation and this temperature rise cause physical parameters to change such as resistance or voltage. The spectral response of thermal detector is determined by the spectral dependence of the surface absorptance. Thermal mass and thermal conductance are associated with the thermal detector, and determine the response time of thermal detector.

Photon detectors generate free electrical carriers through the interaction of photons and bound electrons results in photo effects such as photovoltaic, photoconductive, photoelectromagnetic and photon drag.

The current responsivity of a photodetector is determined by the quantum efficiency (η). The photoelectric gain and quantum efficiency describe the performance of the detector which is coupled to the radiation to be detected. As a result, it turns out as number of electron-hole pairs generated per incident photon. In the results, the photon detector can carry a photocurrent which is proportional to the power intensity of the incident radiation. However photovoltaic (Schottky barrier) and photoconductive (p-n junction) detectors have been widely exploited. Photon detectors use general semiconductor materials such as HgCdTe, InGaAs, InSb, PtSi, PbS, PbSe, SiGa, SiAs, SiSb, etc. Figure 2.2 shows infrared detector technology and comparison of different infrared detector materials using the noise equivalent temperature difference (NETD) measured I degrees K.

For more demanding applications, advanced infrared detection systems have led to the use of photon detectors. On the other hand, thermal detectors are low cost and commonly used for a variety of detector applications.

Recent advances in microfabrication techniques and materials science have led to the exciting field of uncooled detectors which promise lower cost of system operation and functionality of portable system.

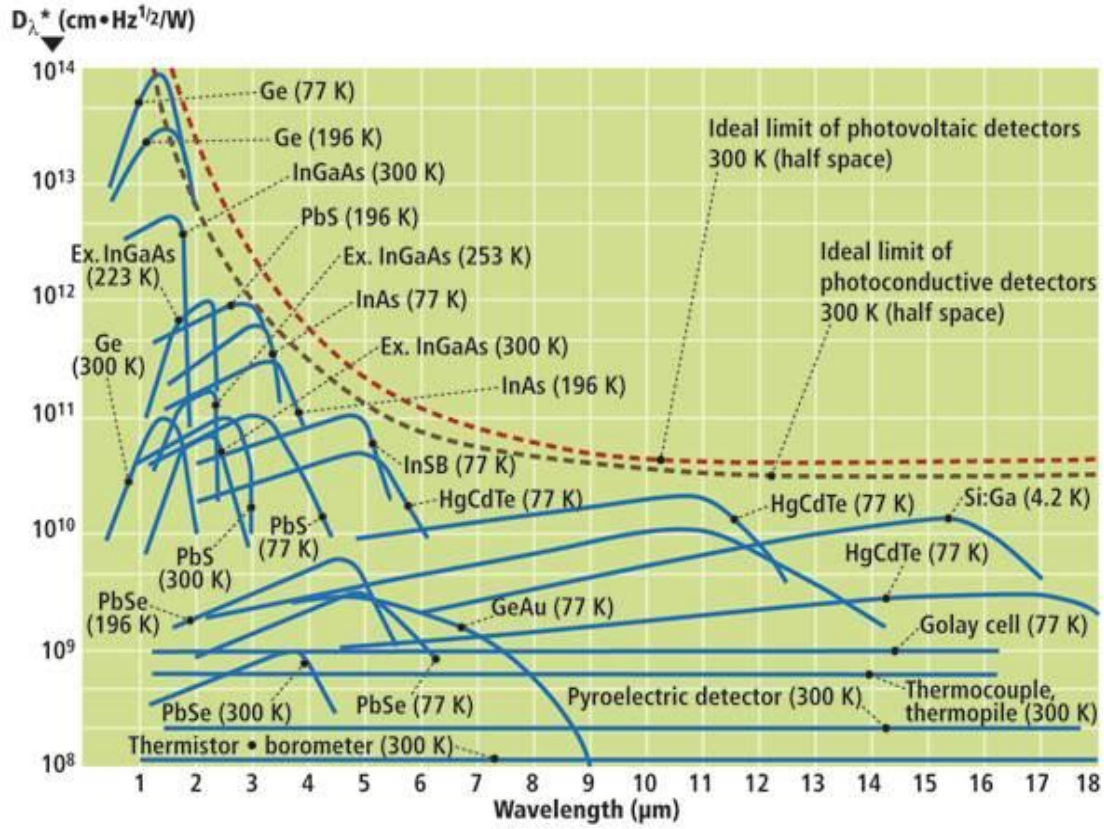

Figure 2.2: Infrared detector technology. Comparison of different infrared detector materials using the noise equivalent temperature difference (NETD) measured in degrees K. [9] (Courtesy of Hamamatsu)

2.4 APPLICATIONS OF INFRARED DETECTOR TECHNOLOGIES FOR THERMAL IMAGING

Infrared detector technologies for thermal imaging have been the subject of research and development for many decades in a wide variety of different applications and infrared focal plane arrays (FPAs) are now fast emerging in military, civilian, scientific and medical applications such as medical diagnosis, environmental and chemical process monitoring, forensic drug analysis, building diagnostics, microscopy, Fourier transform infrared spectroscopy, spectroradiometry, astronomy, night vision in vehicles, and industrial thermography (e.g., microelectronics: inspection of microchip and circuits, electrical and mechanical equipment fault detection). Figure 2.3 shows a variety of applications of infrared thermal imaging.

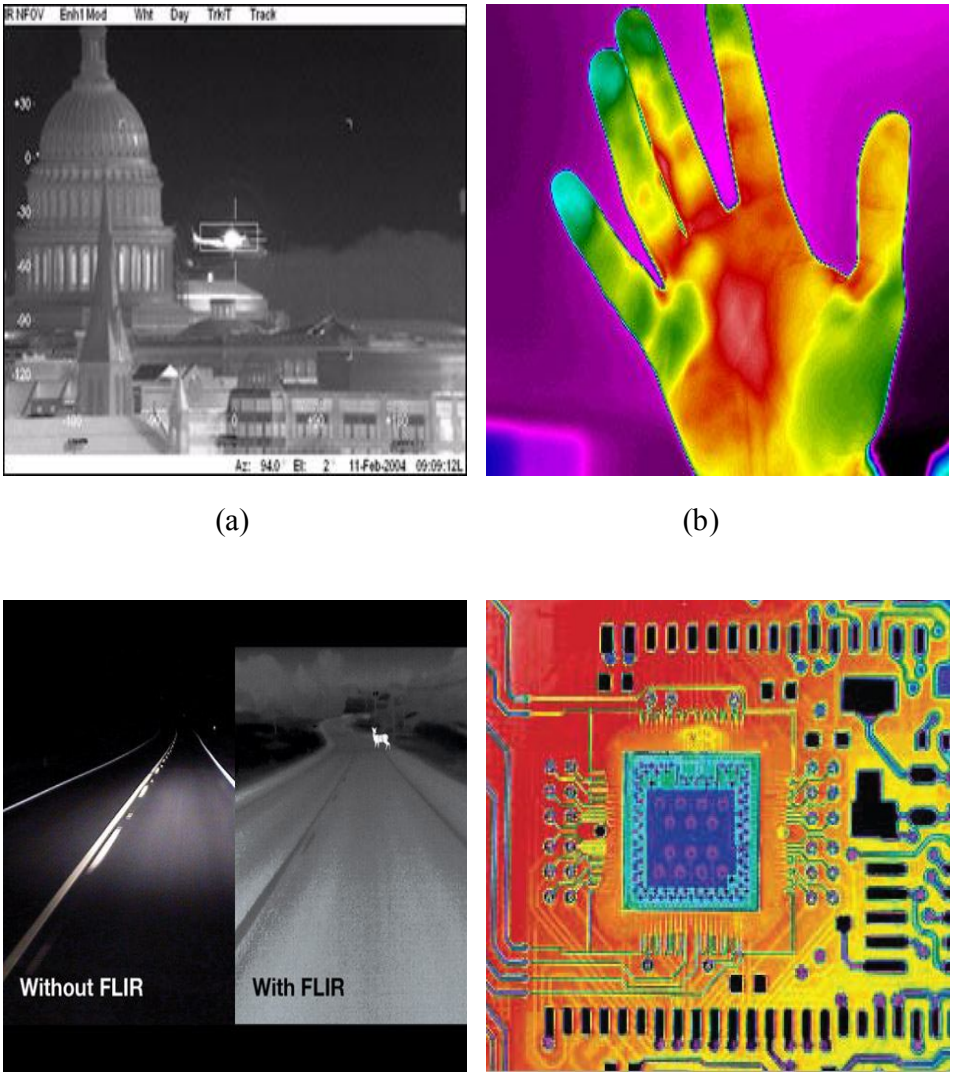

(a) (b)

(c) (d)

Figure 2.3: Applications of infrared thermal imaging. (a) Security and defense (b) Medical diagnosis (c) night vision (d) micro chip inspection (Courtesy of FLIR) [10].

2.5 BACKGROUND OF UNCOOLED INFRARED MICROBOLOMETERS

The name bolometer comes from the ancient Greek word *bole*, for something thrown, as with a ray of light. Bolometer was invented by American astronomer Samuel Pierpont Langley in 1878 and his bolometer was the first to measure the energy flow in form of electromagnetic radiation from the sun using a blackened platinum absorber element, which consisted of two platinum strips covered with lampblack and a simple Wheatstone bridge sensing circuit. The circuit was fitted with a sensitive galvanometer and connected to a battery. As a result, electromagnetic radiation falling on the exposed strip would heat it and change its resistance.

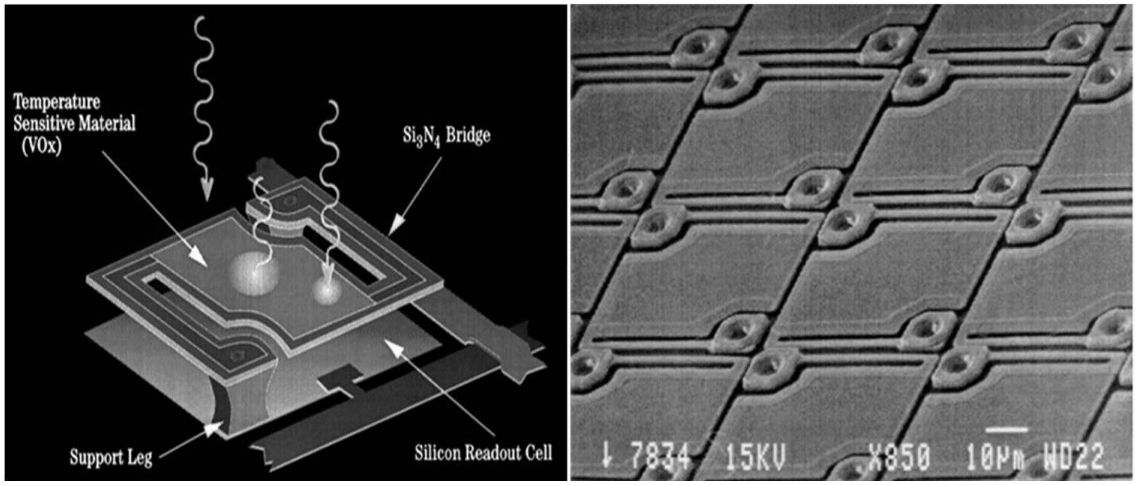

(a) (b)

Figure 2.4: Conventional microbolometer (a) Microbolometer Unit cell depiction (b) SEM image of Microbolometer FPA [11].

Conventional microbolometer technology was originally developed by Honeywell in the mid 1980's as a classified contract for the US Department of Defense. The United States government declassified the technology in 1992. After declassification Honeywell

licensed their technology to several manufacturers. Figure 2.4 shows illustration of conventional uncooled infrared microbolometer and fabricated uncooled infrared microbolometer FPAs.

At present, the majority of infrared detector systems have an uncooled infrared microbolometer focal plane array due to cost consideration. Table 2.1 shows commercial and state-of-the-art R&D uncooled infrared microbolometer FPAs. Microbolometer FPAs do not require a cooling system which allows for compact infrared system designs that are relatively lower cost. Uncooled infrared microbolometer FPAs can be fabricated with metal or semiconductors based materials and are able to operate with non-quantum efficiency at room temperature [12][13] .

Company	Bolometer Type	Array Format	Pixel pitch [μm]	Detector NETD [mk] (f/1, 20-60Hz)
FLIR (USA)	VOx	160x120-640x480	25	35
	VOx	320x240	37.5	50
L-3 (USA)	α-Si	160x120-640x480	30	50
	α-Si/α-SiGe	320x240-1024x768	R&D:17	30-50
	VOx	320x240-640x480	28	30-50
BAE (USA)	VOx (Standard design)	160x120-640x480	17	50
	VOx (Standard design)	1024x768	R&D:17	
	VOx (umbrella design)	320x240	25	35
DRS (USA)	VOx (Standard design)	320x240	17	50
	VOx (umbrella design)	640x480	R&D:17	
	VOx	320x240-640x480	25	30-40
Raytheon (USA)	VOx (umbrella design)	320x240-640x480	17	50
	VOx (umbrella design)	640X480,1024X768	R&D:17	
ULIS (France)	α-Si	160x120-640x480	25-50	35-80
	α-Si	1024x768	R&D:17	
Mitsubishi (Japan)	Si diode	320x240-640x480	25	50
SCD (Israel)	VOx	384x288	25	50
	VOx	640x480	25	50
NEC (JAPAN)	VOx	320x240	23.5	75

Table 2.1: Commercial and state-of-the-art R&D uncooled infrared microbolometer focal plane arrays (FPAs) [14].

2.6 THEORY OF CONVENTIONAL UNCOOLED INFRARED MICROBOLOMETERS

2.6.1 Responsivity

The responsivity parameter $\Re$, a function of the blackbody temperature, is the output signal voltage from detector (a pixel of an array) divided by the incident radiant power falling on that pixel.

$$\Re_{\mathrm{v}} = \frac{V_s}{P_o} \qquad \text{Eq.2.4}$$

$$\Re_{\mathrm{i}} = \frac{I_s}{P_o} \qquad \text{Eq.2.5}$$

where V_s: Output signal voltage [V], P_o: Radiant input power [W], I_s: Output signal current [A].

2.6.2 Noise Equivalent Power (NEP)

The Noise Equivalent Power (NEP) is defined as the absorbed power change that produces a signal equal to the total (root mean square: rms) noise.

$$\mathrm{NEP} = V_n / \Re_{\mathrm{v}} \qquad \text{Eq.2.6}$$

$$\mathrm{NEP} = I_n / \Re_{\mathrm{i}} \qquad \text{Eq.2.7}$$

where V_n is the root mean square (rms) noise voltage within the system bandwidth and I_n is the root mean square (rms) noise current within the system bandwidth.

2.6.3 Noise Equivalent Temperature Difference (NETD)

The Noise Equivalent Temperature Difference (NETD) is defined as the temperature change at the target that produces a signal in the microbolometer equal to the total (root mean square: rms) noise.

$$\text{NETD} = \frac{4F^2 V_n}{\tau_0 A_D \Re(\Delta P / \Delta T)_{\lambda_1 - \lambda_2}} \qquad \text{Eq.2.8}$$

where τ_0 is the transmittance of the optics, $(\Delta P / \Delta T)_{\lambda_1 - \lambda_2}$ is the change in power per unit area radiated by a blackbody at temperature T (with respect to T measured within the spectral band width from λ_1 to λ_2, A_D) ,is the total area of a pixel and F is a function of distance from the optics to the scene being viewed and it defined by

$$\text{F} = \frac{1}{2\sin\theta} \qquad \text{Eq.2.9}$$

where θ is the angle which the marginal rays from the optics make, with the axis of the optics at the focal point of the image.

2.6.4 Detectivity

The Detectivity D is the reciprocal of the parameter Noise Equivalent Power (NEP):

$$\text{D} = \frac{1}{NEP} \qquad \text{Eq.2.10}$$

The signal to noise ratio depends on the square root of the active area of a pixel of the detector. It means that both NEP and Detectivity are function of electrical bandwidth and detector area. Thus a normalized Detectivity D^* is defined to be

$$D^* = \frac{(A_D \Delta f)^{1/2}}{NEP} = \frac{(A_D \Delta f)^{1/2} \Re_v}{V_n} = \frac{(A_D \Delta f)^{1/2} \Re_i}{I_n} \qquad \text{Eq.2.11}$$

where A_D is the active (absorbing) area of the pixel and Δf is signal bandwidth. The unit of D^* is $cmHz^{1/2}/W$.

2.6.5 Temperature Coefficient of Resistance (TCR)

The temperature coefficient of resistance (TCR) is defined as

$$\alpha = \frac{1}{R_0} \frac{dR}{dT} \qquad \text{Eq.2.12}$$

where R_0 is the initial resistance of a pixel, dR is the change in resistance, and dT is the change in temperature. The temperature coefficient of resistance (TCR) can be either positive or negative. For metals at room temperature and superconductors their transition edges have positive TCRs. For semiconductors at room temperature, it has typically negative TCRs. The main reason is that semiconductor materials have mobile carrier densities that increase with temperature increase. The resistance of semiconductors depends on the activation energy for thermal excitation across a bandgap which is defined by

$$R(T) = R_0 \exp(\frac{\Delta E}{kT}) \qquad \text{Eq.2.13}$$

where ΔE is the activation energy and is equal to half the bandgap and R_0 is a constant. As a result, temperature coefficient of resistance (TCR) of semiconductor materials can be defined by

$$\alpha = -\frac{\Delta E}{kT^2} \qquad \text{Eq.2.14}$$

2.6.6 Thermal Response Time

The thermal response time τ_T is defined as the ratio of the heat capacitance of the detector to its effective thermal conductance.

$$\tau_T = \frac{C}{G_{eff}} \qquad \text{Eq.2.15}$$

where C is the heat capacitance of the pixel of detector and G is the total thermal conductance of all the heat-loss from the pixel of the detector. The units of C are joule/deg K, G are W/deg K. So, the units of τ_T are seconds.

Detector materials	α [K^{-1}]
Platinum (Pt)	**0.0018**
Ni-Fe	**0.0023**
Au	**0.0036**
Ag	**0.0037**
Ti	**0.0042**
Ni	**0.005**
Y-Ba-Cu-O (YBCO)	**0.5~1**
Semiconducting YBCO	**-0.0299 ~ -0.0337**
Vanadium Oxide (VO_x)	**-0.02 ~ -0.03**
Bi	**-0.003**
V-W-O	**-1.5 ~ -4.0**

Table 2.2: Infrared detector materials: Temperature Coefficient of Resistance (TCR) [15].

2.7 MOTIVATION OF RESEARCH

2.7.1 Multispectral Infrared Detection

The multispectral infrared detector simultaneously detects infrared radiation emitted by the target in more than one spectral response. Multispectral (Multicolor) capabilities are highly desirable for advanced infrared imaging systems since multispectral detection provide efficient and rapid understanding of the scene due to enhanced target discrimination and identification. Systems that gather data in separate infrared spectral bands can discriminate both absolute temperature and unique spectral signatures of objects in the scene. Using this new dimension of contrast, multispectral detection facilitates advanced color processing algorithms to further improve sensitivity above that of single color detector. Multispectral infrared focal plane arrays (FPAs) are extremely important for a variety of applications such as advanced night vision systems, biomedical thermal imaging, target detection, acquisition and tracking in military and defense areas, airborne surveillance and so on.

The difference between multispectral and hyperspectral imagers is nuanced and both provide data from multitude of wavelengths. Multispectral imager acquires imaging data from discreet wavelengths only, whereas hyperspectral devices provide both imaging data and full spectral at each pixel as well as scanning within a range of wavelengths.

Figure 2.5 shows example of hyperspectral image compared to natural image. (a) is field image and (b) is a hyperspectral image, which is data derived from the airborne hyperspectral imager. This image shows mineralogy of the area. The reddish colors are likely areas with gold mineralization. Green areas are predominantly with the mineral illite at lower temperatures and pressures. Blue areas are sedimentary rocks and red colors shows rocks and the presence of minerals such as alunite and kaolinite.

(a) (b)

Figure 2.5: Applications of mineral identification using hyperspectral imaging (a) Field photograph, (b) Hyperspectral image (Courtesy of University of Twente) [16].

2.7.2 Multispectral Infrared Detectors

Commercial multispectral infrared detector systems are bulky, complex, and extensive in system size, relatively high cost and require cooling systems [17].

Conventional multispectral infrared detector systems use classical optic techniques such as either dispersing the optical signal across multiple infrared focal plane arrays (FPAs) or using filter wheel to spectrally discriminate the image focused on a single infrared focal plane arrays (FPAs). These systems use optical components such as bandpass filters, grating, lenses, and beam splitters in the optical path to focus images onto separate focal plane arrays responding to multispectral infrared.

Recently, development of multispectral infrared detectors is focused on focal plane arrays, such as HgCdTe (Mercury Cadmium Telluride: MCT) photodiodes, strained

layer superlattice (SLs), quantum well infrared photodetectors (QWIPs)[18] and quantum dot infrared photodetectors (QDIPs). Comparison of current competitive 3rd generation infrared detector technologies are shown in Table 2.3. However, these multispectral infrared detectors are facing major challenges, which are concerned with complicated device structure, multilayer material growth, lower operational temperature, requiring cryogenic cooling systems and more difficult device fabrication.

	Micro Bolometer	HgCdTe	InSb	QWIPs	QDIPs	Superlattices (SLs)
Multispectral Detection	**No**	**Yes**	**No**	**Yes**	**Yes**	**Yes**
Operational Temperature	**Uncooled**	**77K (PV), 193K(PC)**	**77K**	**70K**	**135K, 250K**	**77K**
Quantum Efficiency (%)	**Not Applicable**	**89.2**	**85**	**~19 @65K**	**~10**	**~60**
High Detectivity	**No**	**Yes**	**Yes**	**Yes**	**Yes**	**Yes**
Homogenity	**Yes**	**No**	**Yes**	**Yes**	**Yes**	**Yes**
Status	**Practically implemented**			**Theoretically predicted**		

Table 2.3: Comparison of competitive third generation infrared detectors [19]

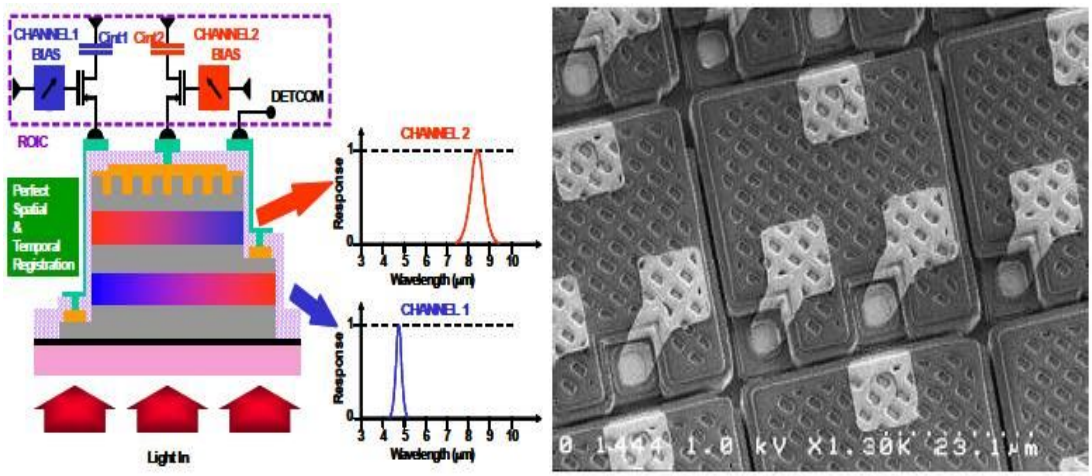

(a) (b)

Figure 2.6: Two-color quantum well photodetector (QWIP) focal plane arrays: (a) Illustration of a dual-band quantum well photodetector (QWIP), (b) SEM image of fabricated two-color quantum well photodetector (QWIP) FPAs [20].

Figure 2.5 shows schematic and fabricated devices for dual band (MWIR/LWIR) quantum well infrared photodetectors (QWIPs) focal plane arrays. They integrate within each pixel both MWIR and LWIR spectral sensitivity. Vertically stacked two color focal plane arrays eliminate internal band optical distortions and temperature induced alignment errors. In addition, quantum well infrared photodetectors (QWIPs) focal plane arrays have demonstrated an improvement in measurement accuracy, high pixel functionality, high yield, high thermal and spatial resolution, excellent homogeneity, low fixed-pattern noise and low1/f noise. However, structure layer thickness (operating wavelengths are determined by each layer thickness) of dual-band quantum well infrared photodetectors (QWIPs) is controlled by molecular beam Epitaxy (MBE) growth.

Example of dual band infrared image using quantum well infrared photodetectors (QWIPs) focal plane arrays is shown in Figure 2.6 (Yellow area indicate above 27 °C and green area indicate above 29°C).

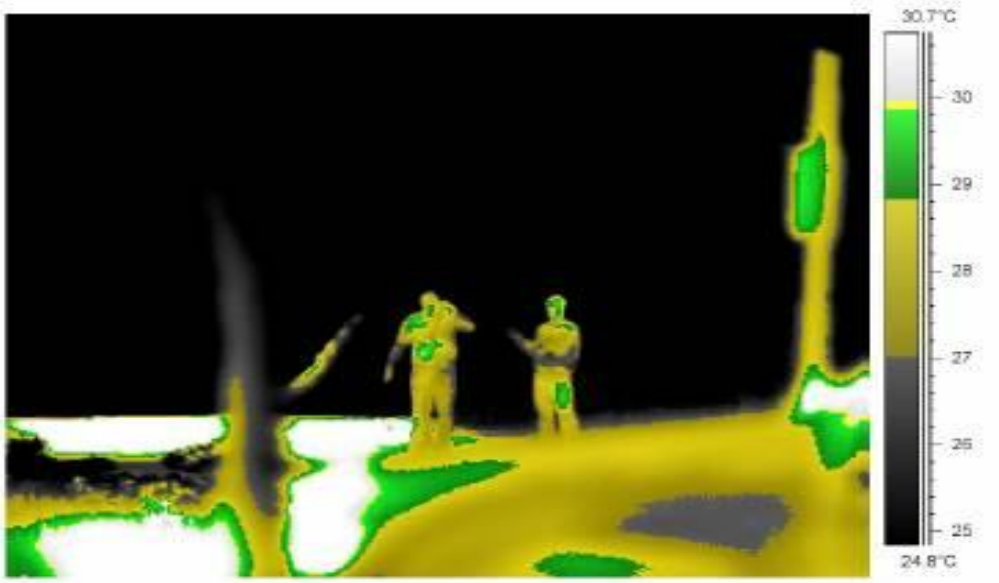

Figure 2.7: Dual band infrared image using quantum well photodetector (QWIP) focal plane arrays [21].

After the success of quantum-well structures for infrared detection, quantum dot infrared photodetectors (QDIPs) have emerged. Generally quantum dot infrared photodetectors (QDIPs) are similar to quantum well infrared photodetectors (QWIPs), however QWIPs replaced by QDIPs due to size confinement in spatial directions.

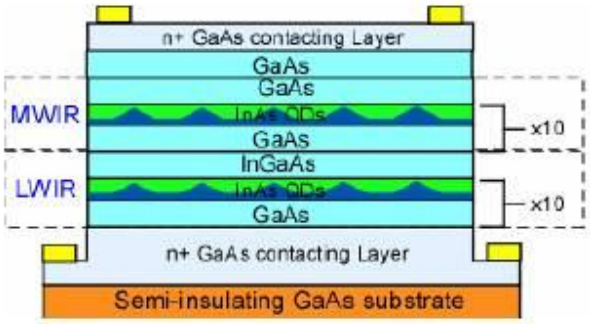

Figure 2.8: Schematic of multispectral quantum dot infrared photodetectors (QDIPs) [22].

Figure 2.7 shows schematic of multispectral quantum dot infrared photodetectors (QDIPs). This device consists of InAs quantum dots layers in two different cap layers, InGaAs and GaAs for mid-wave infrared (MWIR) and long-wave infrared (LWIR) absorption, respectively. This multispectral quantum dot infrared photodetectors (QDIPs) absorption band consists of 10 periods of InAs/InGaAs quantum dot layers stacked between the top and bottom electrode. Theoretically, is better performance (lower dark current, higher responsivity, etc) for is predicted QDIPs, compared with QWIPs. However, multispectral quantum dot infrared photodetectors (QDIPs) potential has not yet been realized completely.

Chapter 3: Fabrication of Wavelength Selective Germanium Dielectric Coated Salisbury Screen Microbolometers

In this chapter, fabrication of a wavelength selective Germanium dielectric coated Salisbury screen microbolometer is described. Device fabrication methods and related issues are covered.

3.1 The Process for Polyimide as Sacrificial Layer

3.1.1 Curing Process of Polyimide with Thickness Control

Polyimide was developed by DuPont Chemical Company in the 1950s as a high temperature polymer, designed and manufactured for functional and structural properties for electrical, mechanical and medical applications. Polyimide is liquid (resin) prior to undergoing a curing process with applied heat. Curing process irreversibly changes the resin in a rigid material by cross linking the polymer molecules and simultaneously removing the solvent carriers and other volatiles.

The processes of polyimide in semiconductor area are generally spin coated on the substrates. The polyimide resin is applied to similar processes as conventional photoresist and its applications are mainly in protective over-coatings for thin or fragile films of layers and used as interlayer dielectrics in thin film microchip modules.

A sacrificial layer is typically used to provide support to a structural layer on which device layers can be deposited; the sacrificial layer is subsequently removed to leave a suspended or freestanding device. There are several sacrificial layers commonly used in NEMS/MEMS device fabrication such as silicon dioxide, polysilicon and polyimide.

In this study, polyimide was used as a sacrificial layer for forming an air gap. It can be removed by an oxygen plasma ashing process. In addition, the polyimide can be applied by spin coating, it can provide some surface planarization for the silicon circuitry underneath, and after curing it is stable at the temperatures involved in later processing steps. In device fabrication, a layer of PI-2610 and PI-2611 polyimide (HD Microsystems) was used as a sacrificial layer [23].

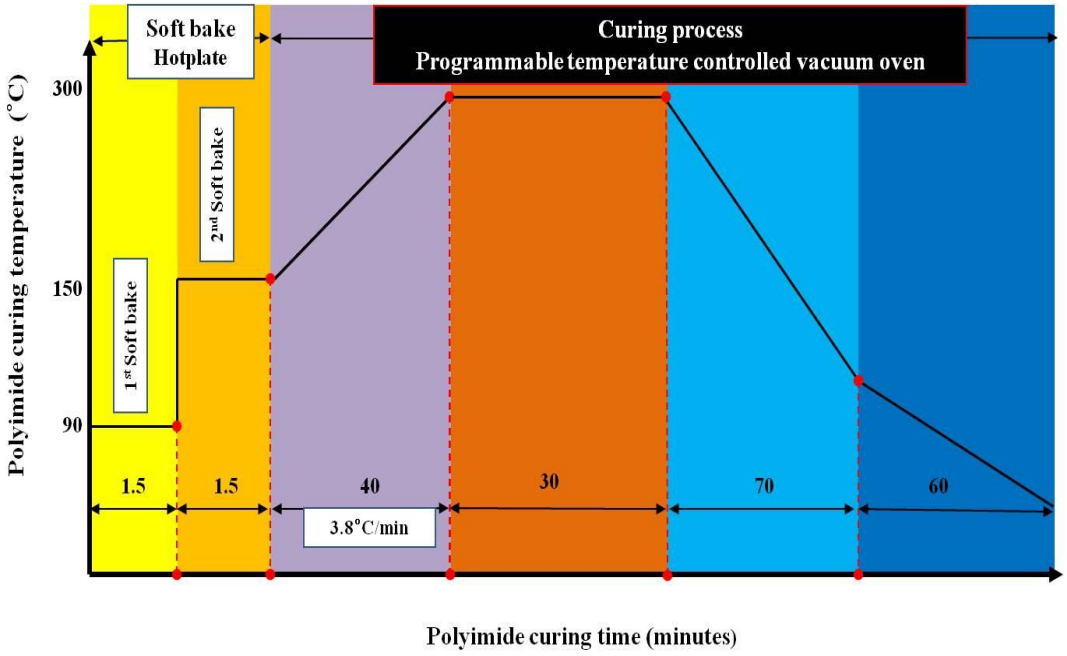

Figure 3.1: Illustration of the curing process use to produce polyimide as sacrificial layer due to formation of air gap.

For the best results, the resin material of polyimide should be stored in refrigerator. After spin coating, a soft bake is generally done on hot plates. The soft bake of polyimide consists of two different temperatures. First step of soft bake is at a

temperature of 90°C for 90 seconds and second step of soft bake is at a temperature of 150°C for 90 seconds. After the spinning step and during the soft bake step the substrate should be kept in a horizontal position. Soft bake time is 30-40 minutes using convection ovens.

For PI-2610 and PI-2611, standard polyimide curing process converts the polyamic acid into a fully aromatic, insoluble polyimide and drives off solvent carrier. This curing process requires increased temperatures and controlled environments to achieve the best polyimide thin films. There is enough energy at 200°C to nearly complete the polyimide imidization process, though higher temperatures are needed to completely dissociate the carrier solvent, fully imidize the polyimide film and complete polymer orientation for optimizing film properties. Curing process can be done in a programmable temperature controlled vacuum oven.

For the optimized results, ramp rate of temperature is ambient up to 300°C in steps of 3.8°C per minute and final curing time is 30 min for desired cured film properties. Figure 3.1 shows the curing process to produce the polyimide as sacrificial layers using two steps: hotplate and programmable temperature controlled vacuum oven.

3.1.2 Patterning Process of Polyimide using Plasma Dry Etching

Plasma dry etching process by reactive ion etching (RIE) and laser ablation processes are possible for polyimide film patterning. Since polyimide film patterning uses general wet etching process, it is very difficult for the formation of molecular structure and inherent film density.

For the dry etching processing, an AZ series photoresist is spin coated over the cured polyimide film. This photoresist etch mask should have a lower etch rate than the

polyimide in an oxygen based plasma dry etching. Plasma etch conditions depend on the plasma etch equipment, polyimide film thickness and resolution. The gas composition of 90-95% Oxygen and 5-10% CF_4 is used. The power density of RIE is usually 200W and vacuum pressure in the range of 200 mTorr. After plasma dry etching it may be necessary to clean the pattern of residuals. Figure 3.2 shows results of polyimide pattern arrays using oxygen plasma dry etching such as 140 μm by 140 μm square pattern arrays, 190 μm by 190 μm square pattern arrays and 5 μm and 10 μm line width patterns.

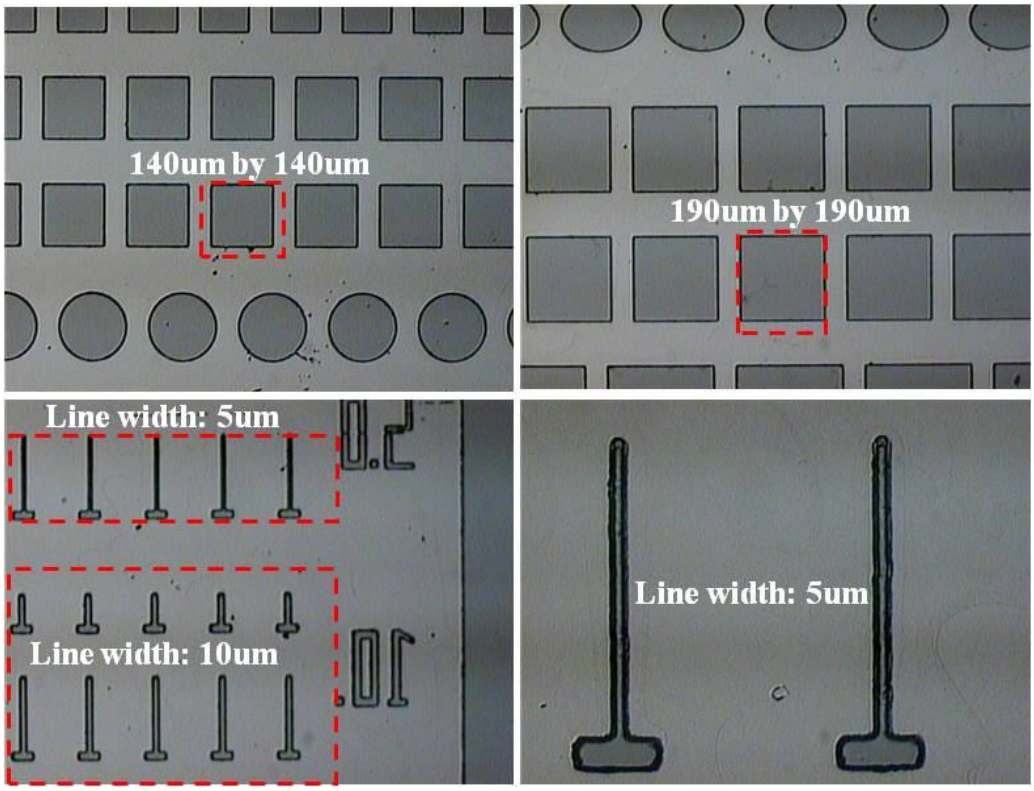

Figure 3.2: SEM images of polyimide patterning using oxygen based plasma dry etching: 140 μm by 140 μm square pattern arrays, 190 μm by 190 μm square pattern arrays, etched polyimide line width (5 μm and 10μm).

AZ series photoresist is used as oxygen plasma dry etch mask. For a successful masking using AZ series photoresist, we need a relatively longer hard baking process due to increased time of polyimide protection against oxygen plasma etch. Figure 3.3 shows optimized plasma dry etching process results.

The Group A indicates results of relatively thin polyimide film (target film etch depth: around 2µm thickness using PI2610) etch rate using RIE and the Group B indicates results of thick polyimide film (target film etch depth: around 5µm thickness using PI2611) etch rate. The etch rate is approximately 0.15 µm per minute.

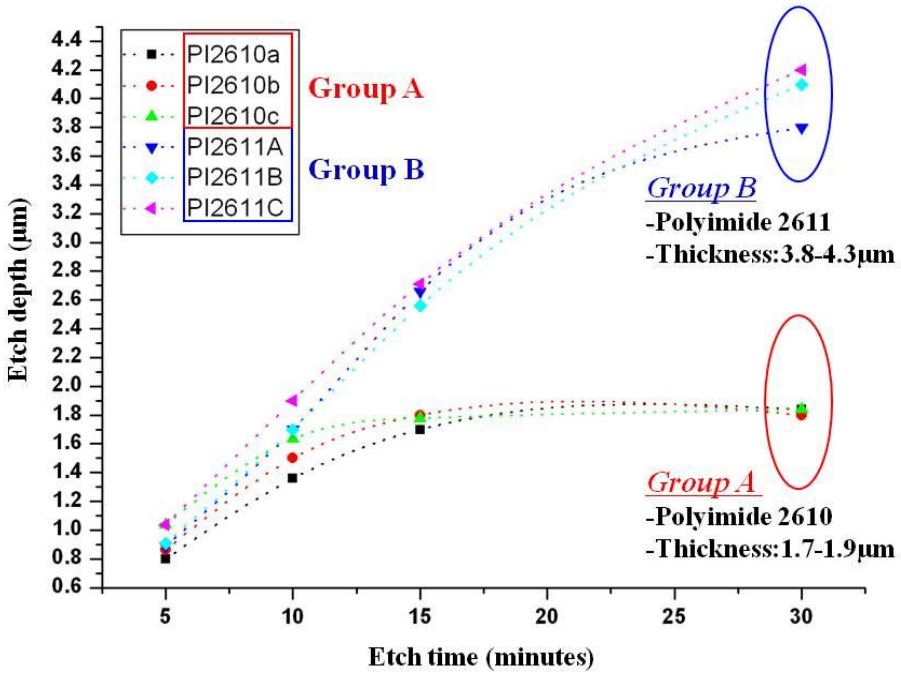

Figure 3.3: Results of polyimide plasma dry etch study for two different polyimide resins. Group A: Thin polyimide films (PI2610), targeted etch depth around 2 µm, Group B: Thin polyimide films (PI2611), targeted etch depth around 5 µm.

The SEM images of over etched pattern arrays are show in Figure 3.5. These results suggest that an undesired process occurred during the overall fabrication process. Understanding of these problems requires process evaluation studies, with every step in the process isolated and SEM examinations done after each step. Figure 3.4 shows SEM images of initial status of over-etching done by plasma dry etch (before removing photoresist mask layer). This led to the discovery that for polyimide sacrificial layer we have two potential issues in the plasma dry etching process. First issue is that the masking layer (AZ series photoresist), used to pattern the polyimide, might not survive the full polyimide etch time. Second issue is that the actual reactive ions etching (RIE) of the polyimide can lead to extremely rough and textured layers.

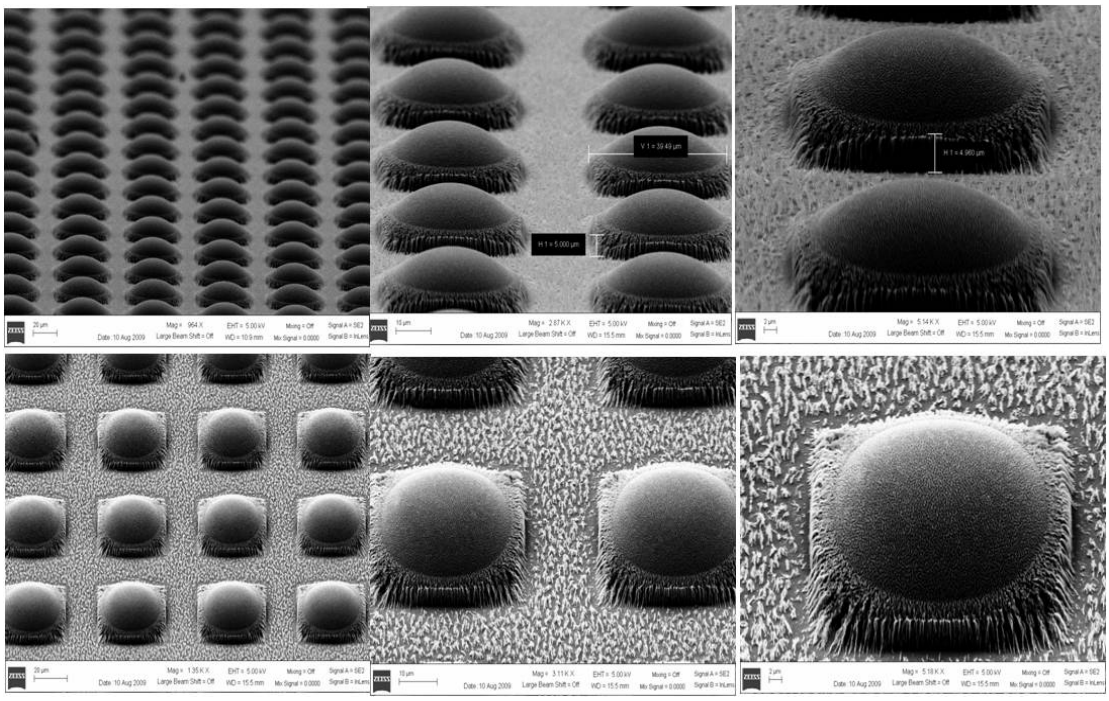

Figure 3.4: SEM images of thick polyimide etching process: initial status before over oxygen plasma dry etching.

Figure 3.5 shows a SEM of a square of polyimide that has been partially etched. In this case the square area should have been protected by a photoresist mask, but instead the mask did not survive long enough to complete the polyimide etch, leading to erosion of the square. As the mask layer was removed and the polyimide below began to etch, the polyimide removal was very non-uniform at the sub-micron scale, producing a very rough, textured layer. Even in the areas around the square that should have been cleanly etched we observed very rough, textured residue.

To understand what might have caused this roughening, we performed a literature search; we found that RIE etching of polyimide can in fact produce such a textured layer [24].

In order to determine infrared spectral absorption characteristics, textured polyimide samples were measured using vacuum Fourier transform infrared spectroscopy (FTIR). There were fourteen different samples prepared with either Au-Cr or Al mirror layers with polyimide spacer layers, subjected to varying degrees of etch process using reactive ion etching (RIE) in Figure 3.6.

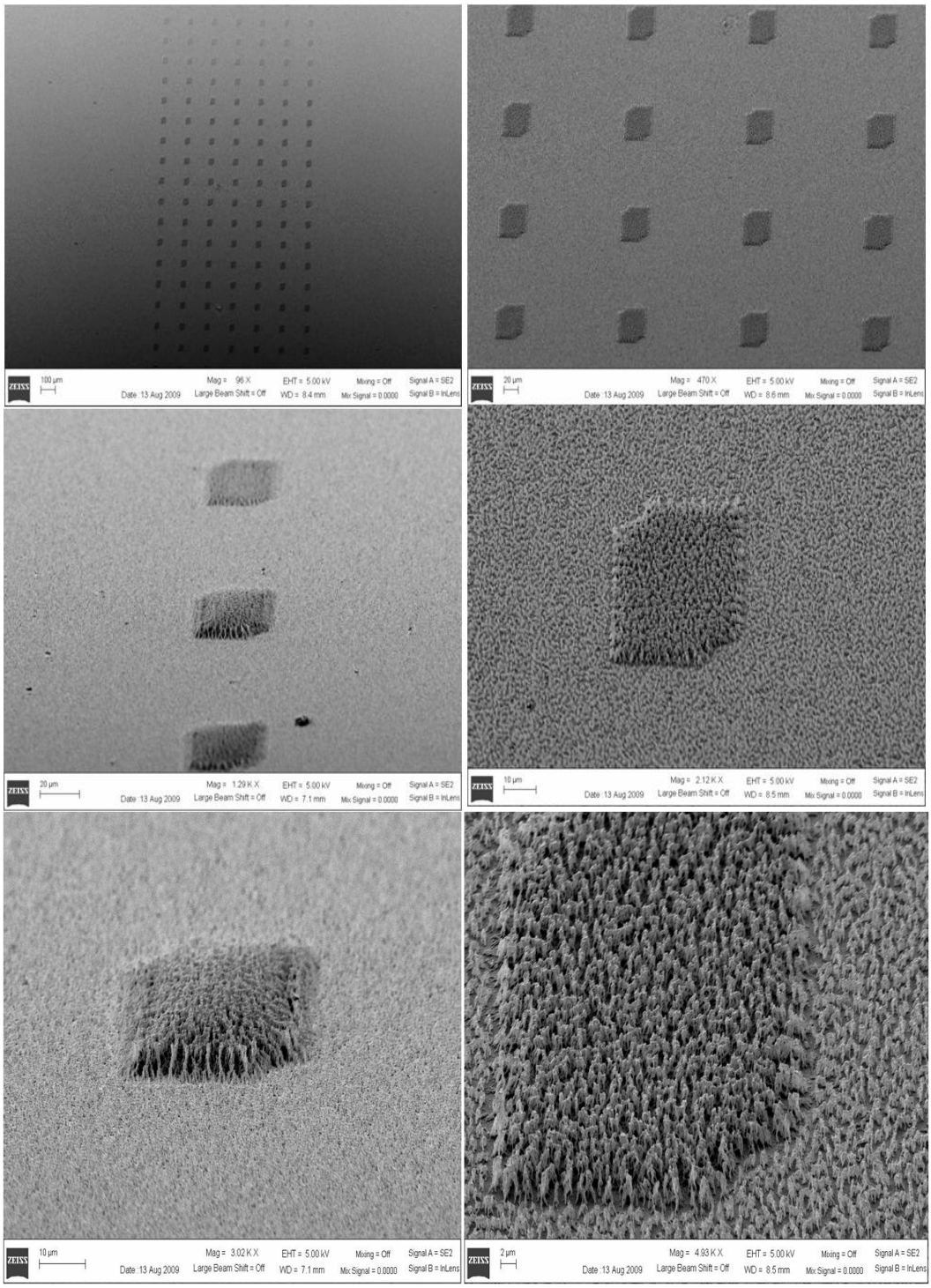

Figure 3.5: SEM images of roughness of a polyimide pattern arrays due to over etch by oxygen plasma dry etching using reactive ion etching (RIE).

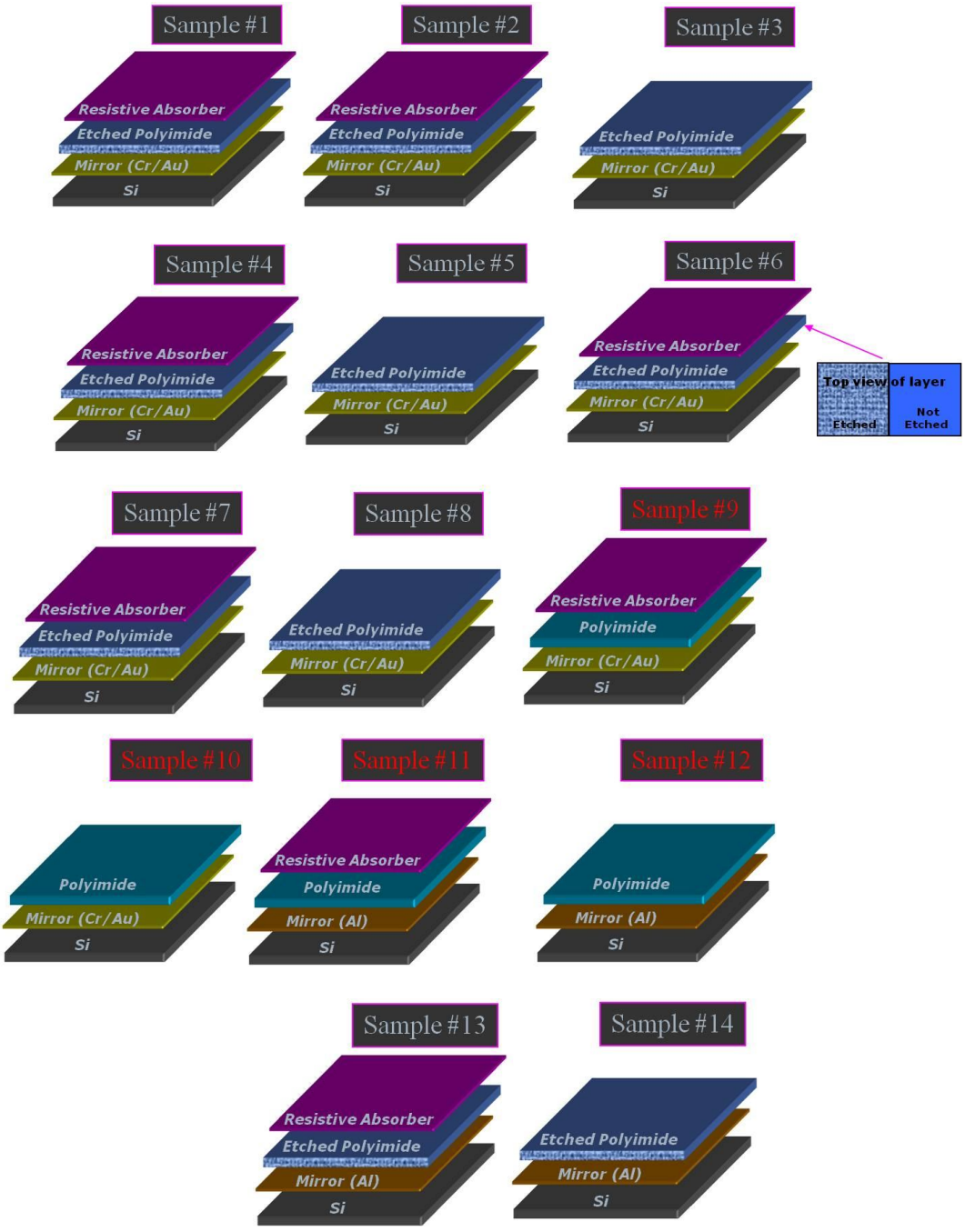

Figure 3.6: Illustration of the fourteen polyimide dielectric Salisbury screen samples fabricated for infrared spectral characterization using vacuum Fourier transform infrared spectroscopy (FTIR).

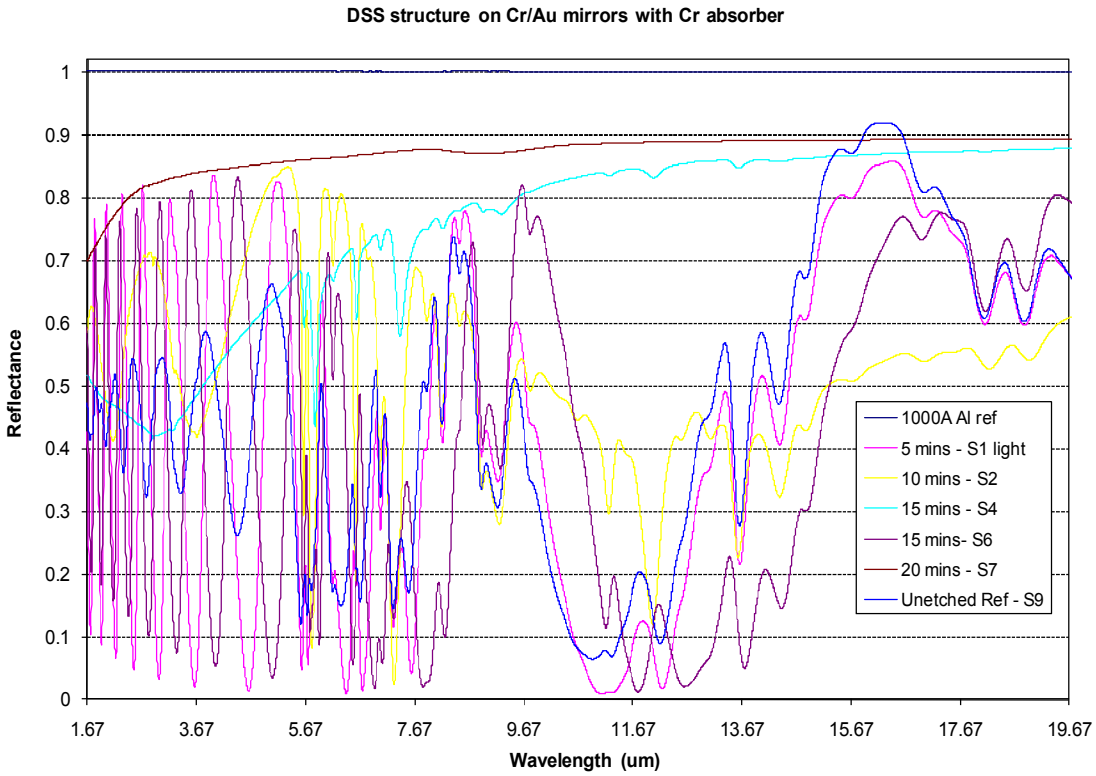

Figure 3.7: FTIR reflectance spectra for polyimide supported Salisbury screen (un-etched sample S9) compared to roughed polyimide samples (S1, S2, S4, S6, and S7, where increasing number indicates greater roughening of the polyimide, FTIR measurement by Ani Weling, Fost-Miller).

The reflectance measurements using FTIR (Figure 3.7 and Figure 3.8) indicate that the polyimide has a number of strong infrared absorption bands beyond wavelength of ~ 5.5 um that largely match published spectra [25]. Below this wavelength, the polyimide acts as a low-loss dielectric spacer layer with varying thickness, depending on the etch time. They were all measured with a 5 mm infrared beam aperture using the Aluminum (1000Å) on Si as reference.

However, the textured samples did not exhibit enhanced absorption or spectrally selective properties in the infrared region.

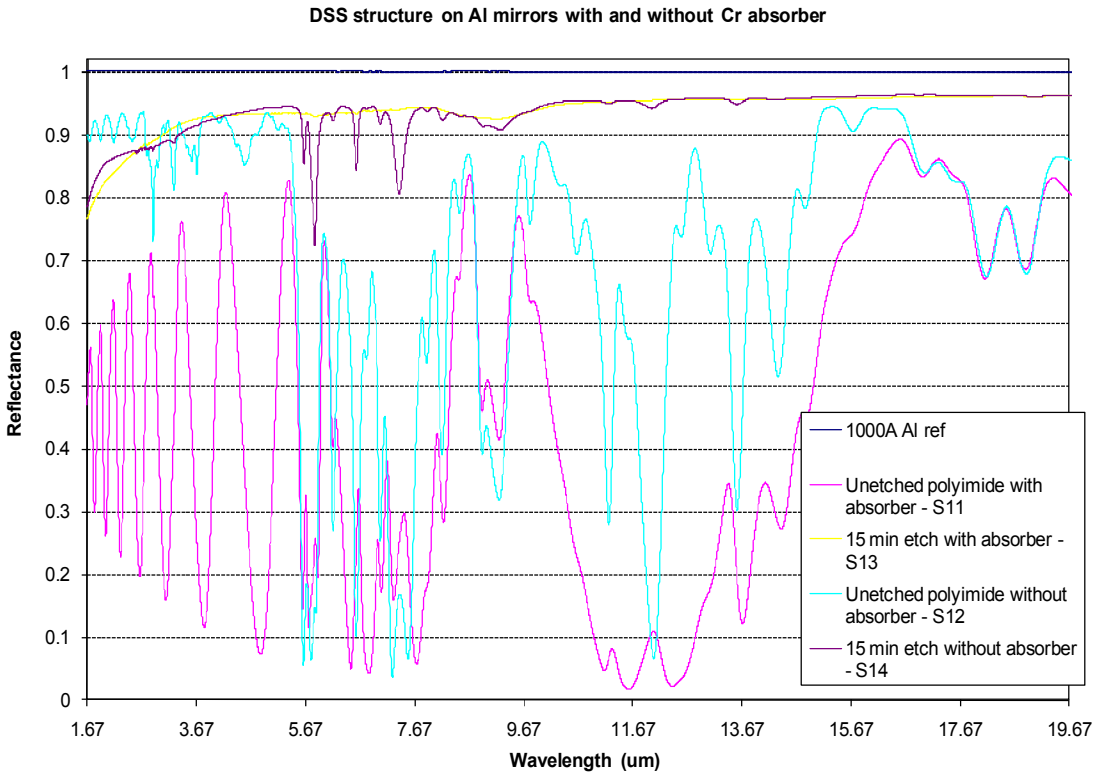

Figure 3.8: FTIR reflectance spectra for polyimide without absorber (un-etched sample S12), with an absorber (un-etched sample S11) compared to roughed polyimide samples (S13 and S14), FTIR measurement by Ani Weling, Fost-Miller.

3.1.3 Process of Photoresist Masking Layer for Thick Polyimide Etching

In order to pattern the thick polyimide (PI 2611: over 5μm), AZ 9260 was employed instead of silicon dioxide mask layer. The reason is that photoresist mask process is relatively simple and it is an easy to remove mask layer after polyimide etching process. Thick photoresist (AZ 9260) is designed for more demanding higher resolution requirements and it provides superior aspect ratio, wide focus and exposure latitude as well as good sidewall profiles of patterns. This photoresist is available in four viscosity levels for expected film thickness, from 2 μm to 24 μm. For the thick polyimide mask layer, photoresist was applied in two steps. In the first step, it was spin coated with a soft bake at 90°C for 5min using hot plate. In the second step, it was again spin coated with another soft bake at 115°C for 1 min using convection oven and rehydration for 20min. UV exposure is followed by development in AZ 400K (1:4) for 210 sec and a rinse in DI water for 1 min. The substrate was then dried with nitrogen gas. Figure 3.9 shows optimization of thick polyimide film thickness control using PI2611 and results of optimized photoresist mask layer (film thickness: 17 μm) are shown in Figure 3.10.

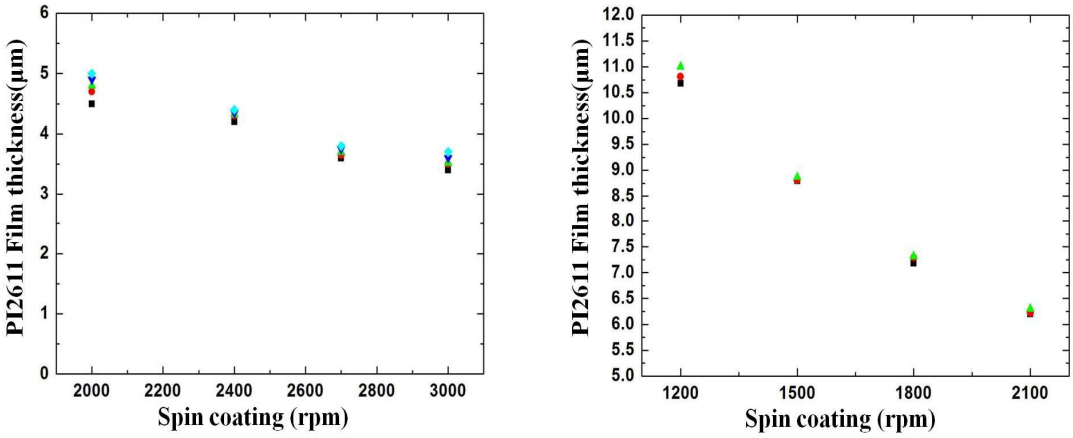

Figure 3.9: Thickness control for thick polyimide using PI2611 (polyimide film thickness: 4μm to 11 μm).

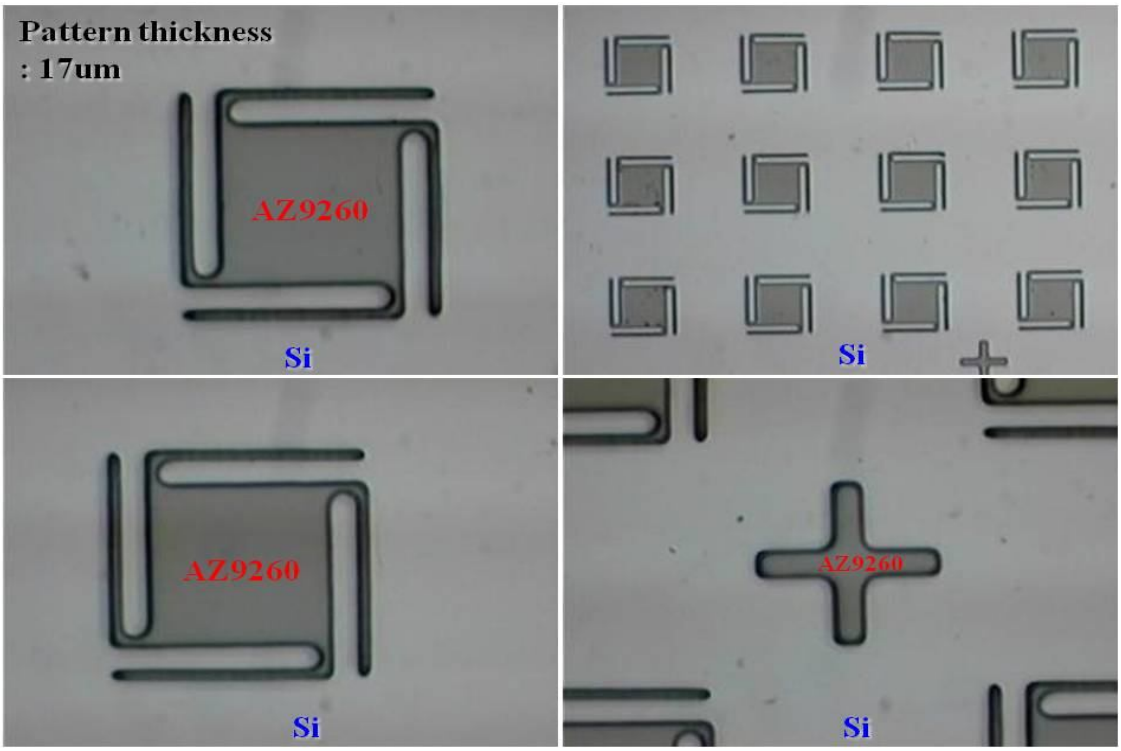

Figure 3.10: SEM images of photoresist mask layer for thick polyimide patterning (photoresist thickness: 17 μm using AZ 9260, exposure time: 310 sec±5sec).

3.2 THE PROCESS FOR GERMANIUM DIELECTRIC STRUCTURAL LAYER

The advantage of using only Germanium as both the interference layer for wavelength selectivity in the dielectric coated Salisbury screen and the structural layer is electromagnetic improvement, as Germanium is low loss and dispersion less in the long wavelength infrared as well as fabrication process simplicity. Germanium as structural layer is evaporated by e-beam evaporator (target thickness: 3000Å and 6250Å, deposition rate: 1.2 Å/sec, chamber pressure: 10^{-6} Torr or lower pressure) and then photoresist patterning as mask layer is performed using photolithography.

Finally, the Germanium layer is etched using reactive ion etching (RIE) for CF_4 gas with 50sccm flow rate. The power density of RIE is usually 200W and vacuum pressure is in the range of 200 mTorr. After plasma dry etching it may be necessary to clean the pattern of residuals. Results of Germanium layer patterning are shown in Figure 3.11.

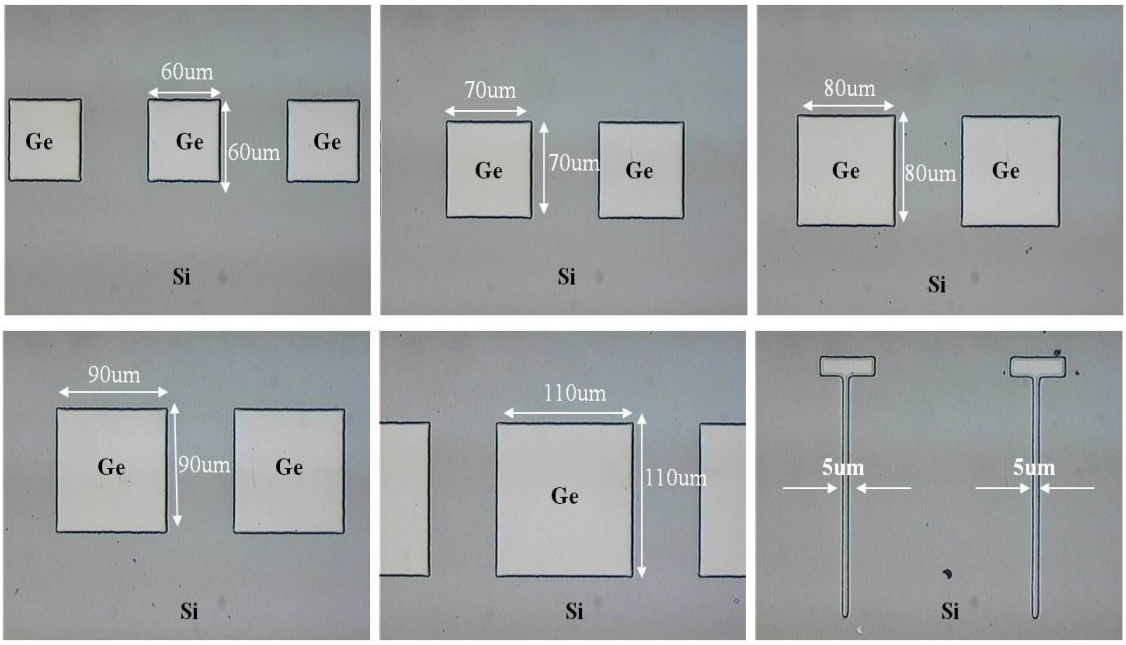

Figure 3.11: Microscopic images of Germanium layer patterning (60 µm by 60 µm, 70 µm by 70 µm, 80 µm by 80 µm, 90 µm by 90 µm, and 110 µm by 110 µm square pattern array, 5 µm line width).

3.3 THE PROCESS FOR AIR GAP FORMATION USING OXYGEN PLASMA ASHING

3.3.1 Process Evaluation of Oxygen Plasma Ashing using Cantilever Structure

In this section, the cantilever structures used to evaluate the polyimide undercut etch process using an oxygen plasma ashing process and undercut inspection after oxygen plasma ashing process, will be discussed.

The process flow is patterning of the Germanium layer and removal of the polyimide as sacrificial layer. The first step is the formation of sacrificial layer using polyimide PI2610 (Targeted thickness of sacrificial layer: 2.0 μm). The second step is the deposition of Germanium as structure using e-beam evaporator (Deposition rate: 2.0 Å/sec, e-beam power: 34%, targeted thickness of Germanium structure: 6000Å). The third step is plasma dry etching of Germanium as structural layer using RIE (Etch rate: 0.0004 μm/sec, power: 150W, CF_4 gas flow rate: 50sccm). The fourth step is oxygen plasma ashing process of polyimide as sacrificial layer (Chamber pressure: 1270 mTorr, Power: 292W, oxygen flow rate: 50sccm, undercut rate: 0.012 μm/sec).

Figure 3.12 shows the top view of fabricated Germanium cantilever structure arrays (Air gap: 2.0 μm). During oxygen plasma ashing process, polyimide surface roughness was measured by using Atomic Force Microscopy (AFM), as shown in Figure 3.13. The area of polyimide surface scanned using AFM, is 30 μm by 30 μm.

Typically, undercut inspection in microbolometer fabrication process is challenging due to relatively thin air-gap space (2.0 μm to 2.5 μm). For this reason, one of the popular microbolometer designs employ etched hole patterns in the active area, to enhance undercut process performance during oxygen plasma ashing process.

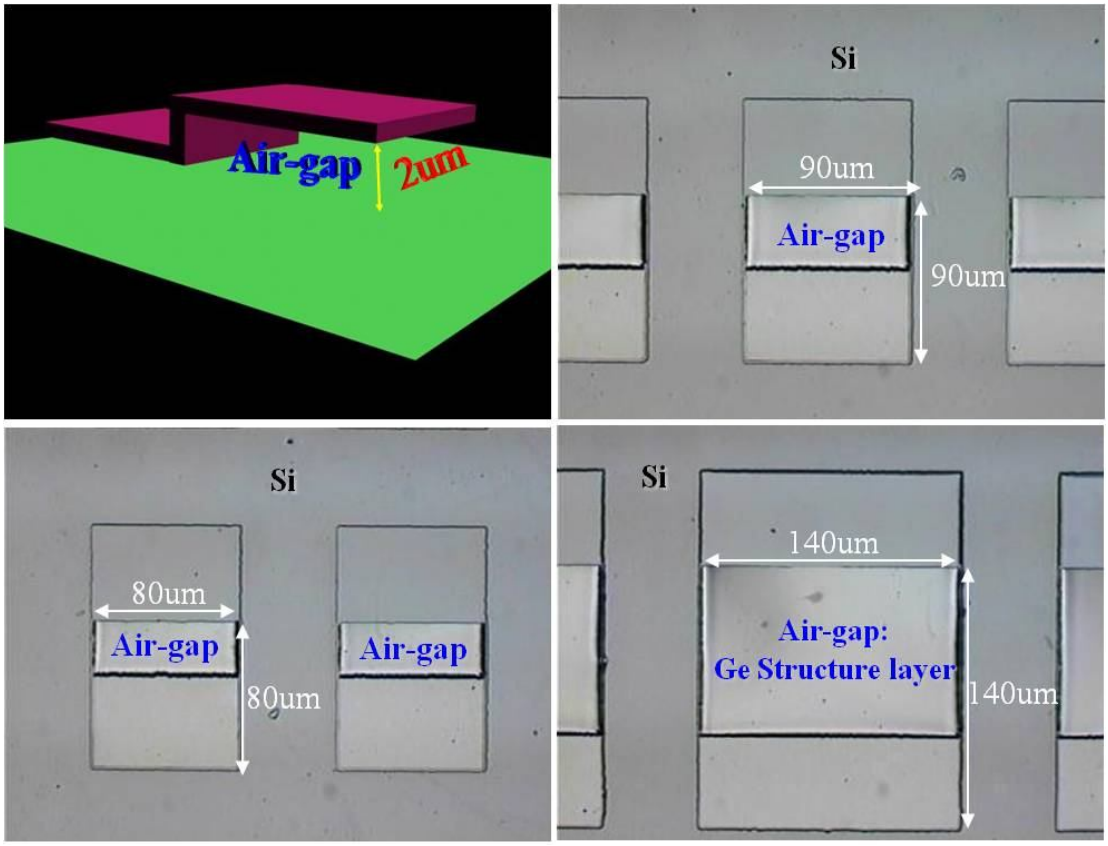

Figure 3.12: Illustration and Microscopic images of fabricated Germanium cantilever structure arrays with air gap (2.0 μm).

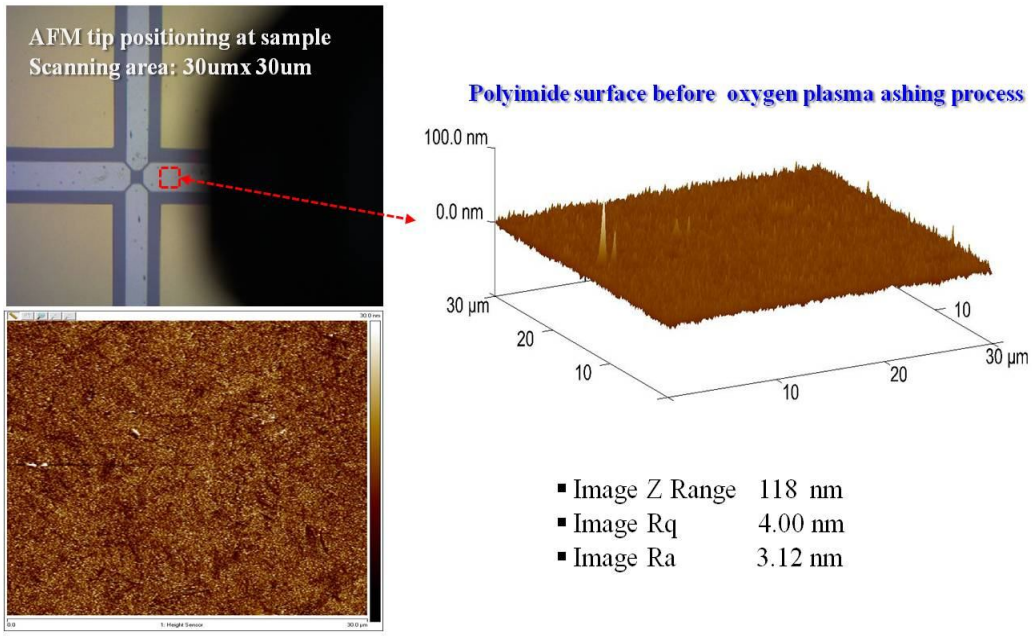

(a)

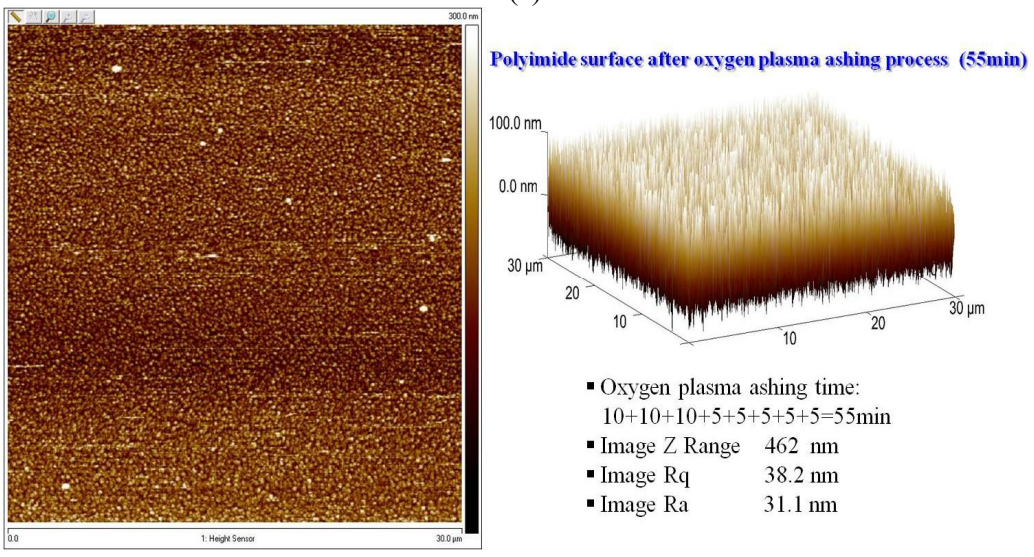

(b)

Figure 3.13: Polyimide surface roughness image using Atomic Force Microscopy (AFM): (a) surface morphology before oxygen plasma ashing (b) after 55min oxygen plasma ashing process.

Demonstration of fabricated Germanium as structural layer with air gap is shown in Figure 3.14. As can be seen, the polyimide sacrificial layer was completely removed from below the Germanium structural layer, using oxygen plasma ashing process. The targeted thickness of Germanium structure is about 6000Å and the air gap is about 2.0 μm. Fabricated Germanium cantilever structures arrays are smooth, flat and robust.

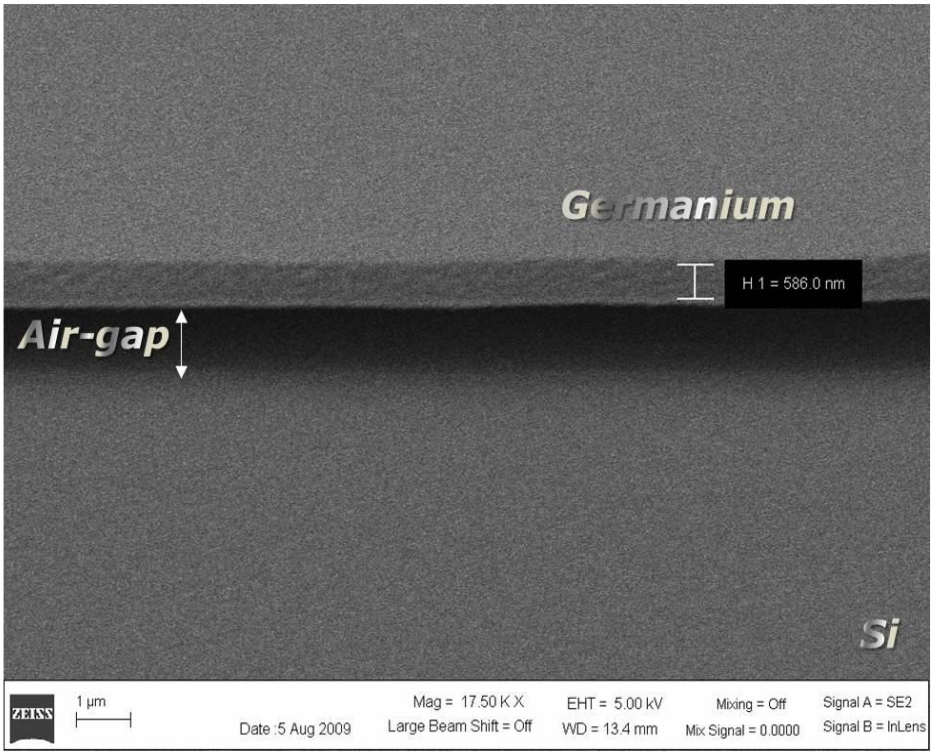

Figure 3.14: SEM image of air gap formation below Germanium structural layer after complete removal of sacrificial layer using an oxygen plasma ashing process.

3.3.2 Polyimide Residue and Structure Deformation under the Oxygen Plasma Ashing Process

In this section, the issues of undercut etch process in oxygen plasma potentially influencing the shape of suspended microstructure and sacrificial residue will be discussed. In order to fabricate the optical resonance cavity and for thermal isolation, the formation of air gap space below the structure layer is one of the key processes in wavelength selective microbolometer fabrication.

Cantilever structures are used to evaluate the polyimide undercut etch process using an oxygen plasma ashing process. However, these process steps have faced several challenging fabrication issues during the oxygen plasma ashing process.

The first issue is related to the polyimide residue due to uncontrolled undercut etch process in Figure 3.15. Second issue is deformable structure layer after completion of the oxygen plasma ashing process in Figure 3.16 and Figure 3.17. The third issue is related to the electrical contact pad damage, which is discussed in the section 3.5.

In general, structure deformation is strongly reduced by lowering the temperature. However, in this study, oxygen plasma undercut processes require over 300 min, where the optimized total release time depends on device design.

The flexural deformation of the released cantilever beam occurs after oxygen plasma ashing process. In order to maintain stable oxygen plasma ashing process conditions, the optimal process time is experimentally determined around 5 min. On the other hand, a continuous single ashing process without break-times results in large plastic deformation of the structure.

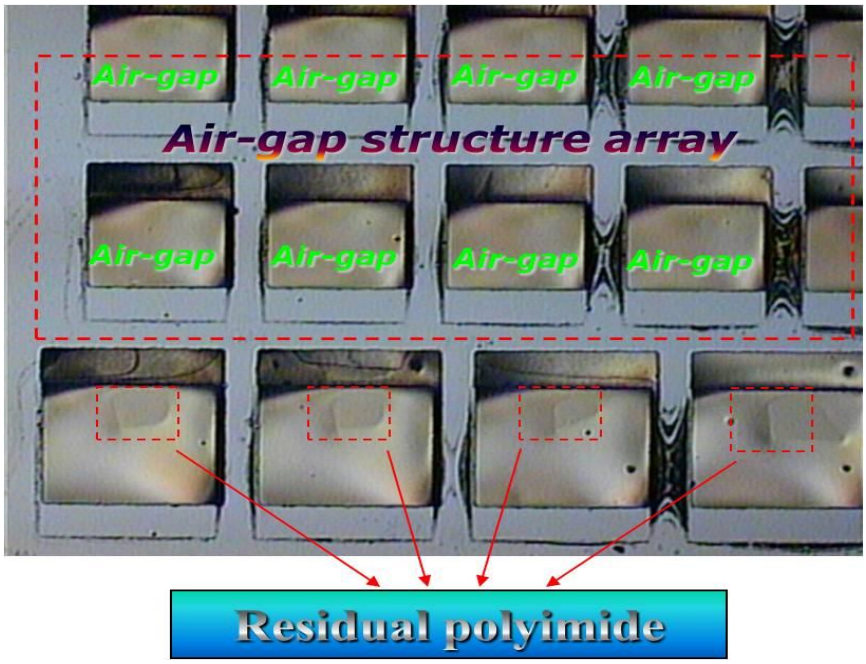

(a)

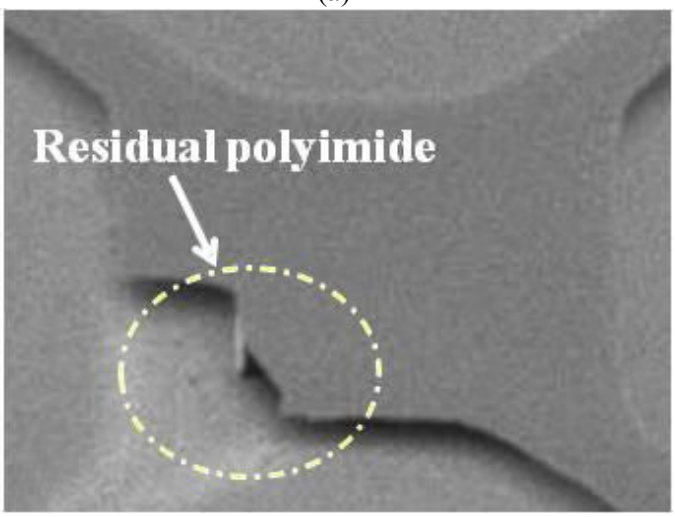

(b)

Figure 3.15: Released structure layer using oxygen plasma ashing process: (a) Formation of air gap and residue of polyimide under structure layer (b) Residual polyimide due to insufficient undercut etch process.

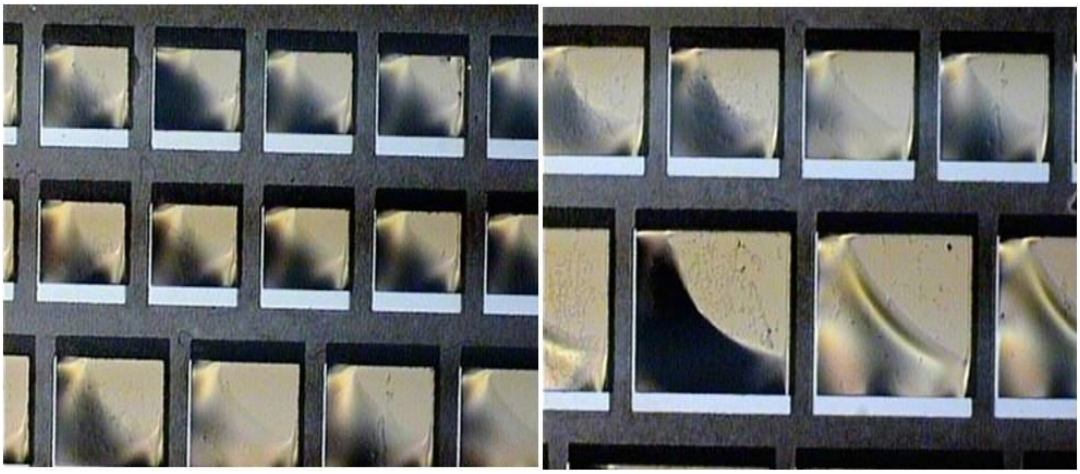

(a)

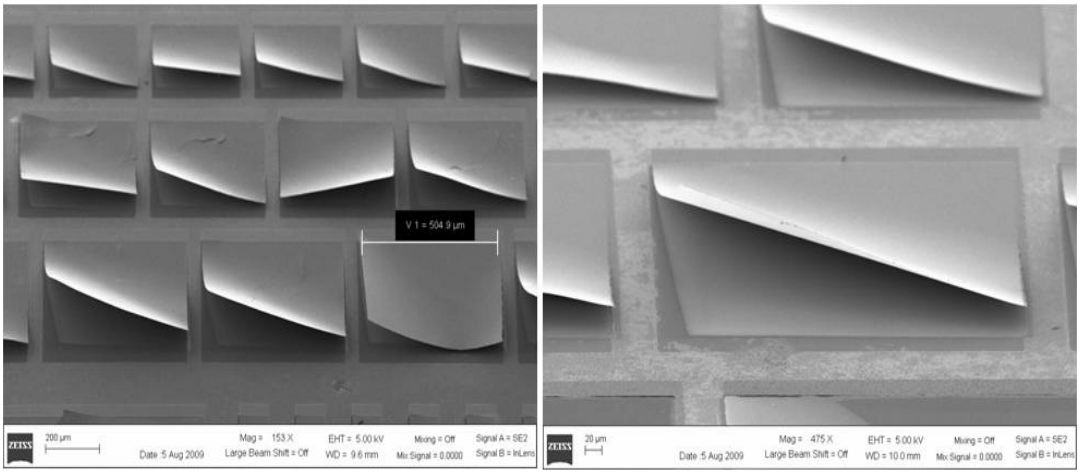

(b)

Figure 3.16: Stress of the cantilever structure arrays during sacrificial layer undercut etch process using oxygen plasma (a) Microscopic images, (b) SEM images.

The oxygen plasma generated during the plasma ashing process can increase the ambient temperature inside the asher chamber, which generates thermal deformation of

the structure. For this reason, in this study the experimental methods of oxygen plasma ashing process consist of a plasma exposure time for undercut and a break time to decrease the temperature of oxygen plasma asher chamber.

Experimental approaches of continuous or long oxygen plasma exposure without break time for air gap formation, can lead to several fabrication issues; especially that of large and incontrollable deformation on practically all structures.

Consequently, a stable oxygen plasma ashing process condition followed by a fixed break time, cyclically repeated until the sacrificial layer is completely removed, results in successful air gap structure formation.

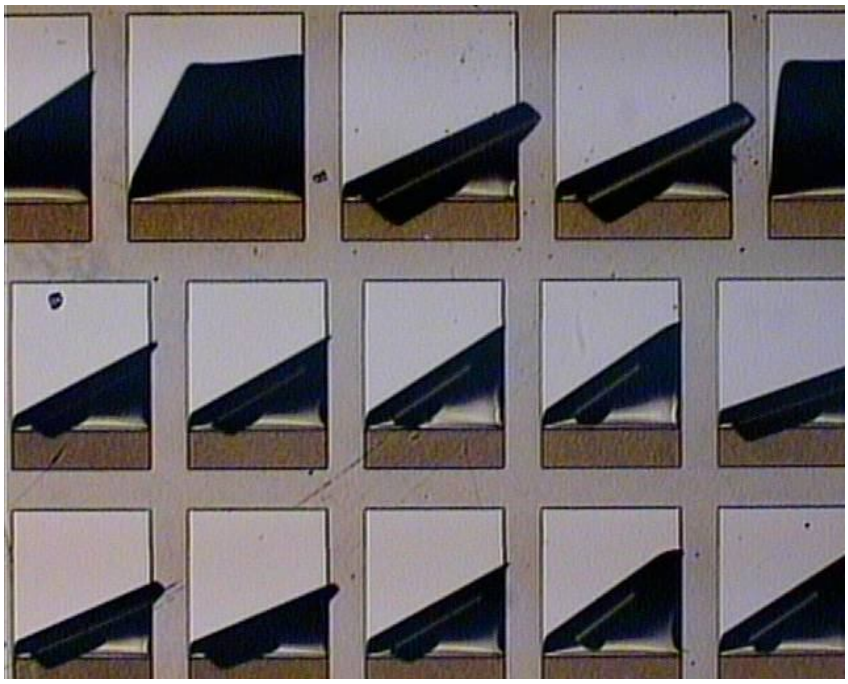

Figure 3.17: Damage to Germanium layer during polyimide undercut etch process using oxygen plasma when exposed for more than 360min. The dark areas are curled layers of Germanium.

3.4 THE PROCESS FOR X SHAPE WAVELENGTH SELECTIVE GERMANIUM DIELECTRIC SALISBURY SCREEN MICROBOLOMETERS

In this section, fabrication of X shape wavelength selective Germanium dielectric Salisbury screen microbolometer will be discussed. Fabrication process flow is shown in Figure 3.18.

The complete process begins with aluminum deposition of a highly reflective mirror layer on a silicon substrate. Next, a controlled thickness polyimide layer is spin-deposited and cured, followed by a photolithography step and an etch step to define a pattern region of polyimide. After which, a controlled thickness germanium structural layer is vacuum deposited over the polyimide sacrificial layer, patterned via normal photolithography and dry etch processes. Then, the sacrificial layer is removed by an oxygen plasma ashing process. Finally, the resistive absorber Cr layer with the appropriate sheet resistance is deposited. Wavelength selective dielectric coated Salisbury screen (DSS) single pixel patterns fabricated with approximately 50μm x 50 μm active areas supported using legs are shown in Figure 3.19.

Fabricated X shape Germanium dielectric coated Salisbury screen (DSS) pixels had good yield. In this fabrication of completed devices the air gap (set by the polyimide thickness) is approximately, 1.8μm, 2μm, and 2.5μm respectively and the germanium structural/interference layer thickness is approximately 0.4 μm, 0.5μm, and 0.6 μm respectively [26].

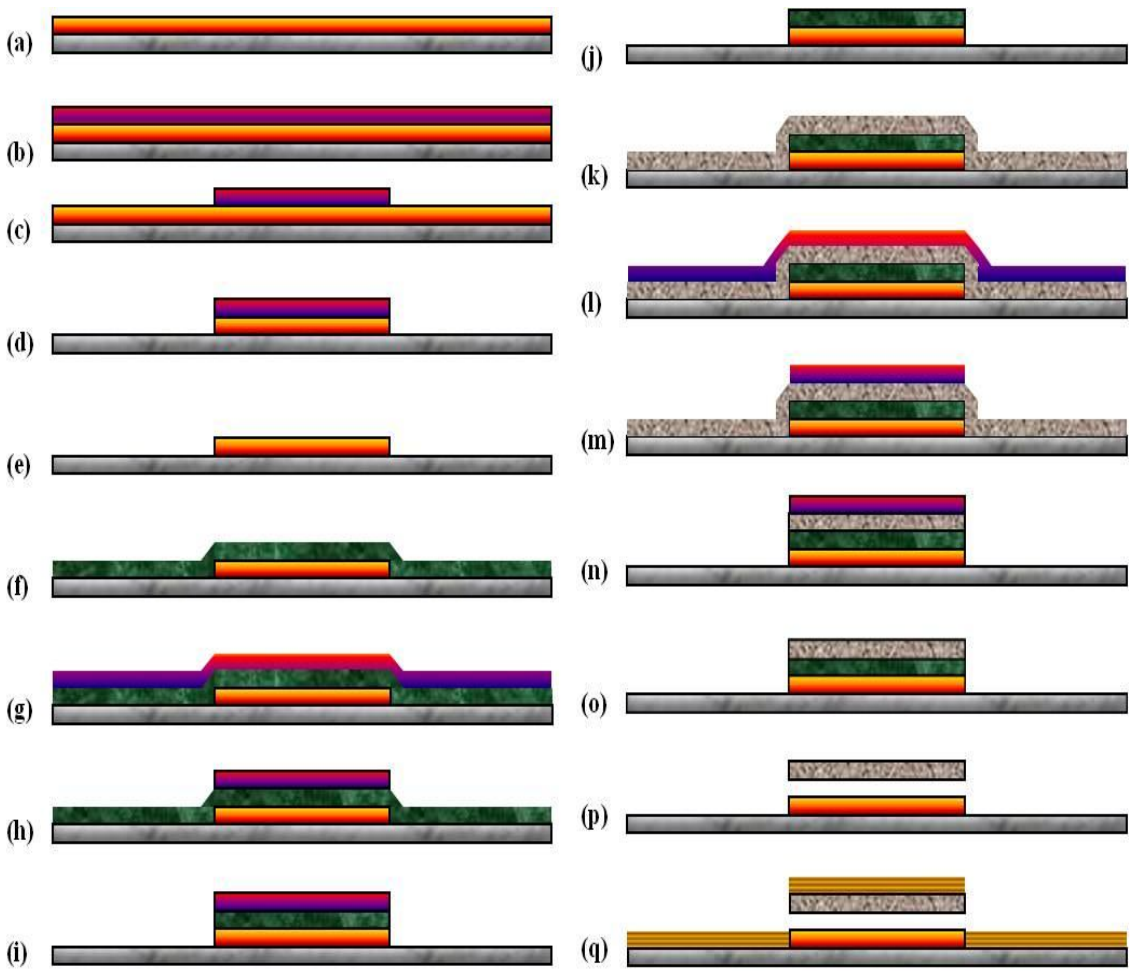

Figure 3.18: Fabrication process flow of X shape wavelength selective Germanium dielectric supported Salisbury screen microbolometers: 1. Formation of reflective mirror layer, (a) to (e), 2.Formationof sacrificial layer, (f) to (j), 3. Formation of Germanium structure layer: (k) to (o), 4. Formation of Airgap, (p) and 5.Formation of absorber layer, (q).

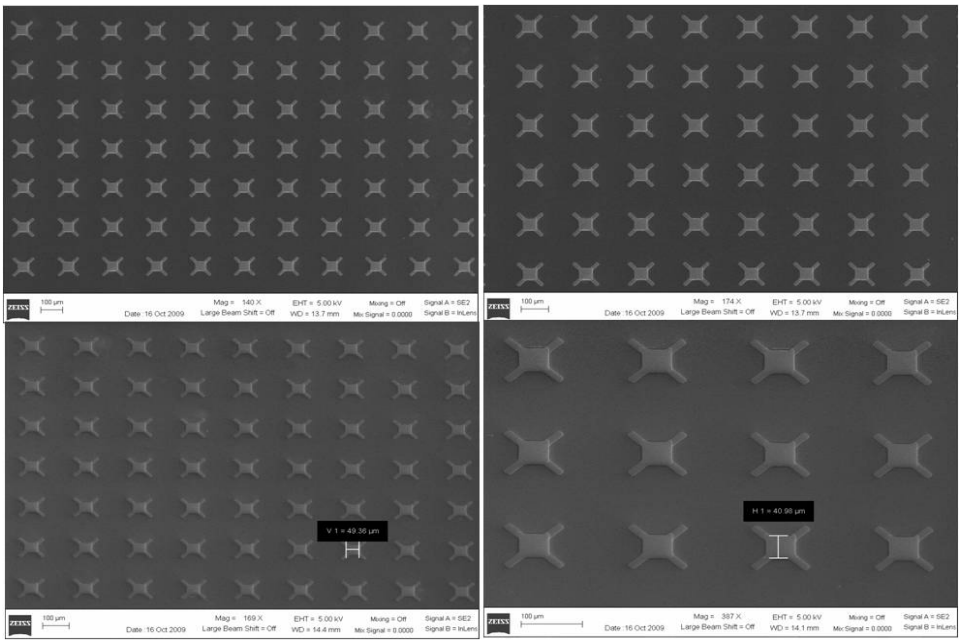

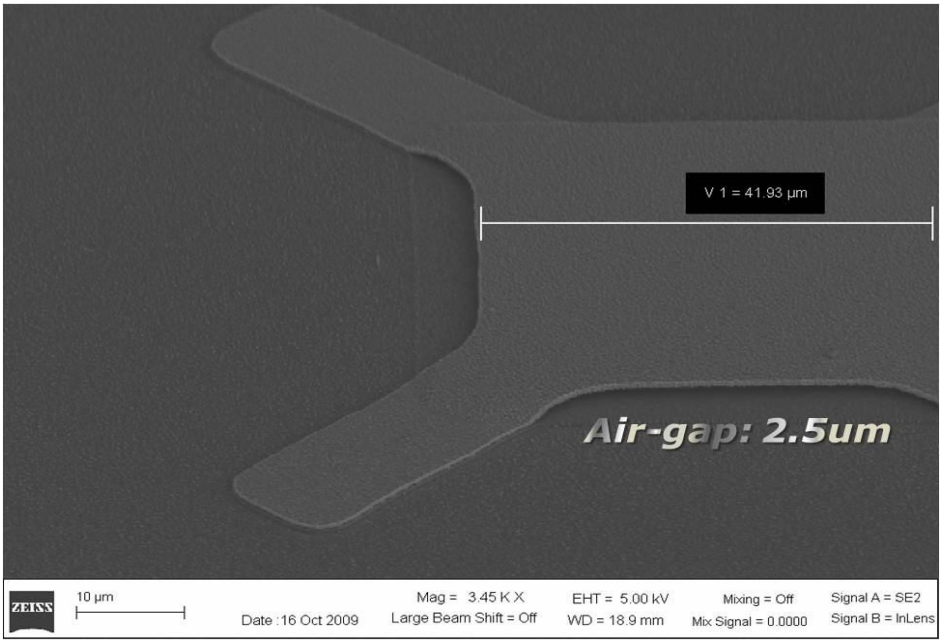

Figure 3.19 SEM image of X shape wavelength selective Germanium dielectric Salisbury screen (DSS) microbolometer (Air-gap: 2.5µm).

3.5 THE PROCESS FOR ELECTRICAL CONTACT PADS

3.5.1 Process of Bi-Layer Lift-off Metallization

In this section, formation of electrical contact pads using bi-layer lift-off process for wavelength selective Germanium dielectric coated Salisbury screen microbolometer will be discussed. Figure 3.20 shows fabricated wavelength selective Germanium dielectric coated Salisbury screen microbolometer whose metallic absorber layer also functioned as an electrical contact pads.

Common methods used for metallization or oxide layer patterning in microfabrication are lift-off process and etching process. Lift-off process is different compared to etching process, in that a sacrificial photoresist layer is exposed using an inverse mask pattern in the lift-off process. Any material which was deposited on the sacrificial layer is removed, while any material which was in direct contact with the substrate remains. However, depending on the lift-off material used, retention typically can occur and unwanted metal pattern may remain on the substrate. Another typical problem in lift-off process is that the metal may get ripped away from the substrate and leaves behind a ragged pattern. All such cases are shown in Figure 3.21.

In this study, bi-layer lift-off method using LOR2A/PGMI is employed as a critical level lift-off process where precise undercut is required as well as an enhanced lift-off process for the formation of electrical contact pads.

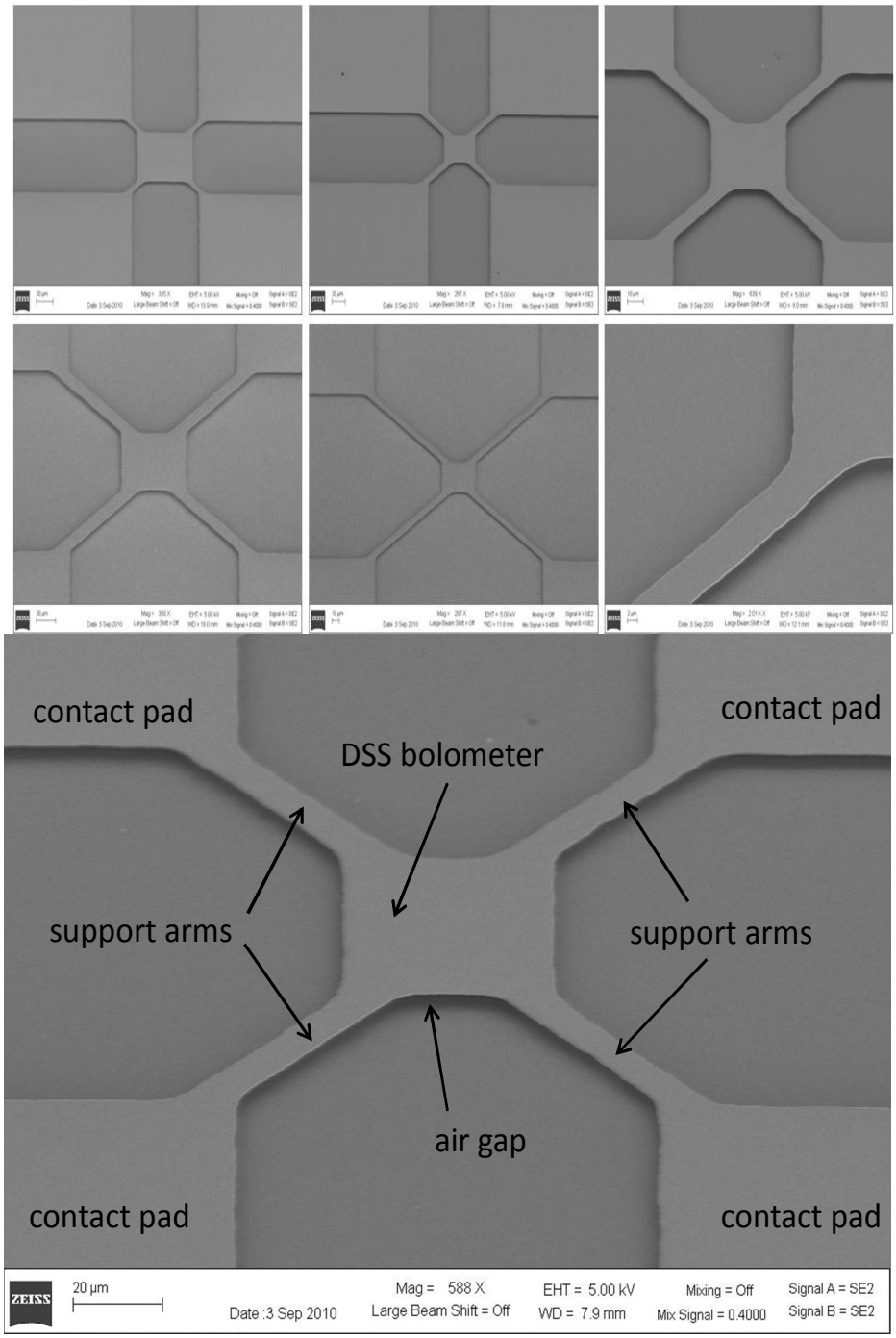

Figure 3.20: SEM images of wavelength selective Germanium dielectric coated Salisbury screen microbolometer arrays using self aligned process: single metallic layer functioned absorber and contact pads.

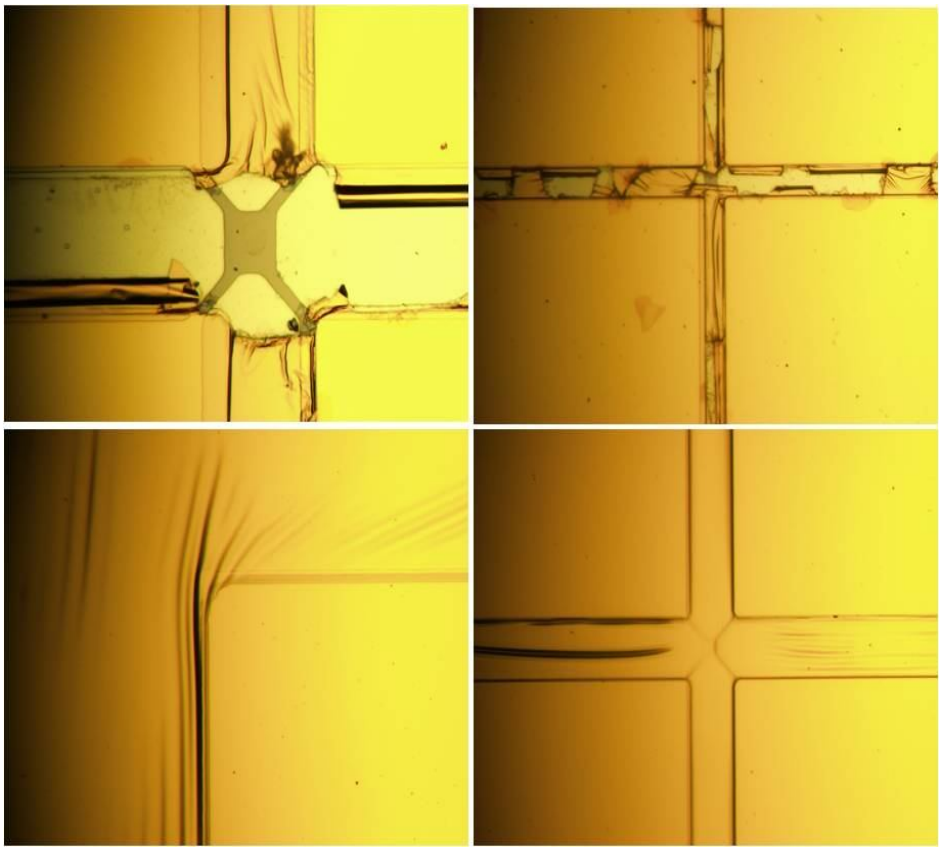

Figure 3.21: Microscopic images of general lift-off process for electrical contact pads with Ti (adhesion layer, 200 Å)/Au (1500Å).

The process flow is shown in Figure 3.22. This bi-layer lift-off process uses Lift Off Resist (LOR) 2A/Polydimethylglutarimide (PMGI), manufactured by Microchem.

These materials are not photosensitive and freely soluble in conventional Tetramethylammonium hydroxide (TMAH) developers.

A general experimental approach to bi-layer lift-off process is to coat the LOR/PMGI on the substrate, followed by photoresist spin coating, which is then developed simultaneously.

If the photoresist is fully developed, the developer continues to dissolve the LOR/PGMI layer. The dissolution rate of developer is isotropic, but can be precisely controlled to undercut edges of the resist profile. The experimental results of bi-layer lift-off process are shown in section 3.6.

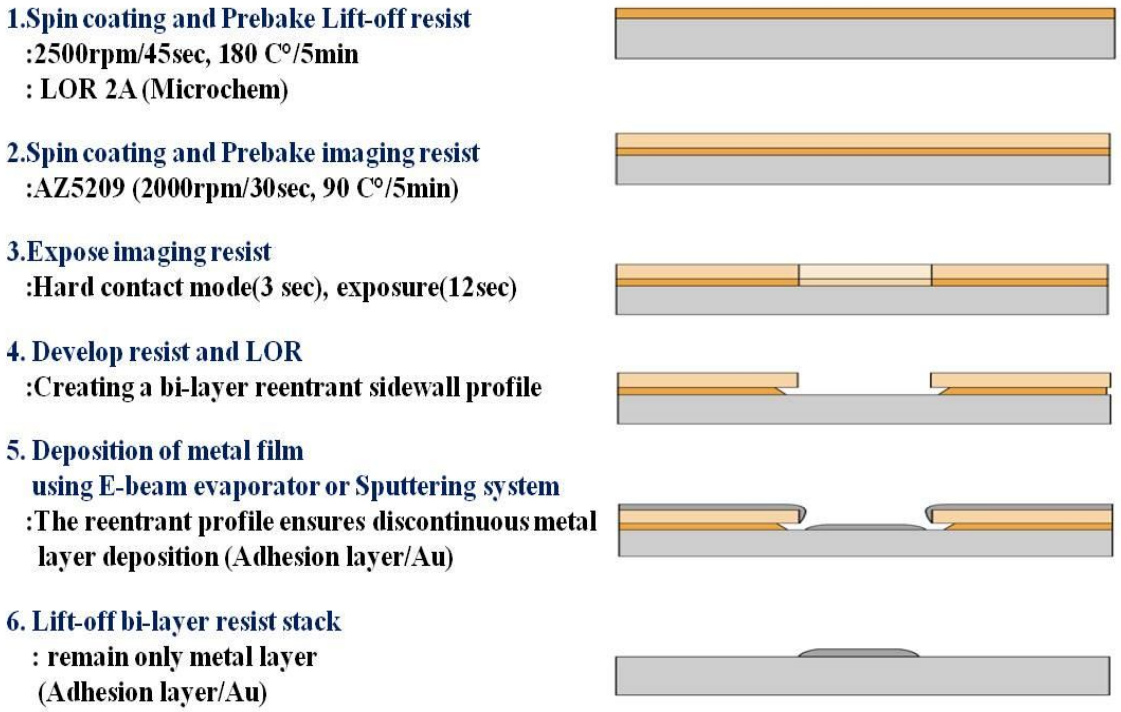

Figure 3.22: Process flow of bi-layer lift-off using LOR2A/PMGI for electrical contact pads of wavelength selective Germanium dielectric coated Salisbury screen microbolometer.

3.5.2 Oxygen Plasma Damage in Adhesion Layer of Electrical Contact Pads

In this section, damage to electrical contact pads of wavelength selective Germanium dielectric coated Salisbury screen microbolometer during oxygen plasma ashing process will be discussed.

In order to form a good electrical contact to a device, good adhesion of metal to the device is an important parameter in microelectronics. Poor adhesion of the metal contact pad layer can result due to thermo-mechanical effects or intrinsic stresses from deposition using sputtering or evaporation process. If a contact metal doesn't have good adhesion to the device surface, an adhesion layer of another metal should be deposited before the contact metal. The most commonly used metals as an adhesion layer for Au in microfabrication are Chromium (Cr), Titanium (Ti), Palladium (Pd) and Ni (Nickel).

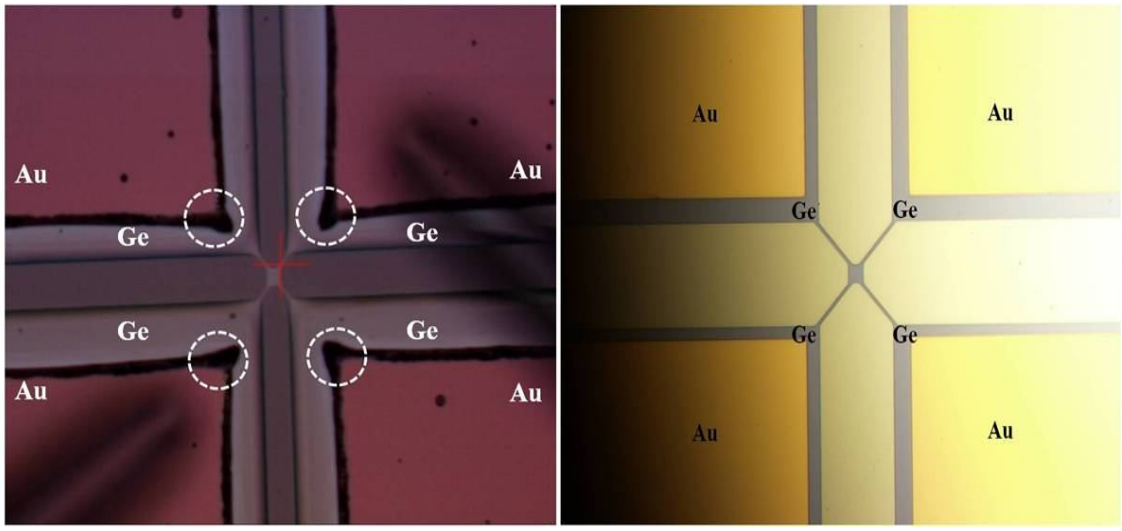

(a) (b)

Figure 3.23: Microscopic image of damage to electrical contact pads after long oxygen plasma ashing process: deposited materials of contact pads (a) Cr/Au, (b) Ti/Au.

If Chromium and Titanium are used as adhesion layers, Au needs to be deposited straight after the adhesion metal is deposited without breaking vacuum, since Cr and Ti oxidize readily forming a surface oxide (native oxide) between the adhesion and contact layers, resulting in increased resistance.

In this study, the additional layer is used to promote adhesion between the Au and Germanium structural layer. In addition, adhesion layers prevent Au from diffusing into Ge. Figure 3.23 shows damage to electrical contact pads (Cr/Au) after long oxygen plasma ashing process. We expect this damage is induced during oxygen plasma ashing process. It should be considered that ions and radicals in the oxygen plasma damage the Cr adhesion layer in electrical contact pads. Illustration of damage models is shown in the Figure 3.24.

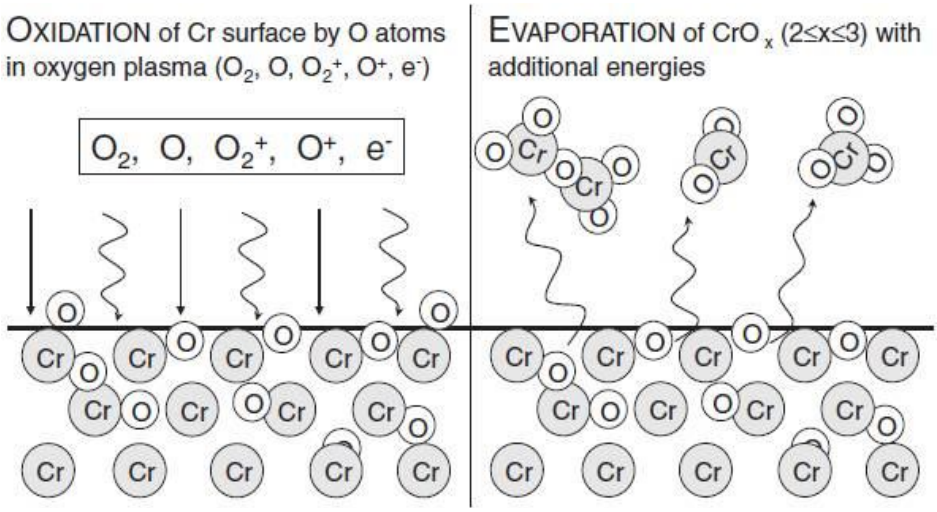

Figure 3.24: Damage model of electrical contact pad under relatively long oxygen plasma exposure time during the ashing process [27].

To overcome the damage to metal contact pads, Titanium and Nickel were chosen instead of Chromium as adhesion layer. These metals can survive under electrical contact pads in a long oxygen plasma ashing process. Figure 3.25 shows top view and cross section view of fabricated electrical contact pads using Ti/Au for wavelength selective Germanium dielectric coated Salisbury screen microbolometer.

To verify fabricated electrical contact pad using Ti (film thickness: 20nm, evaporation rate: 0.3Å/sec) /Au (film thickness: 120nm, evaporation rate: 0.5Å/sec), 3D optical surface profilometer by Veeco-Wyko (NT 9100 Optical Profiler system) was used. We can confirm experimental parameters of fabricated contact pad film and surface morphology after long oxygen plasma ashing process, as seen in Figure 3.26.

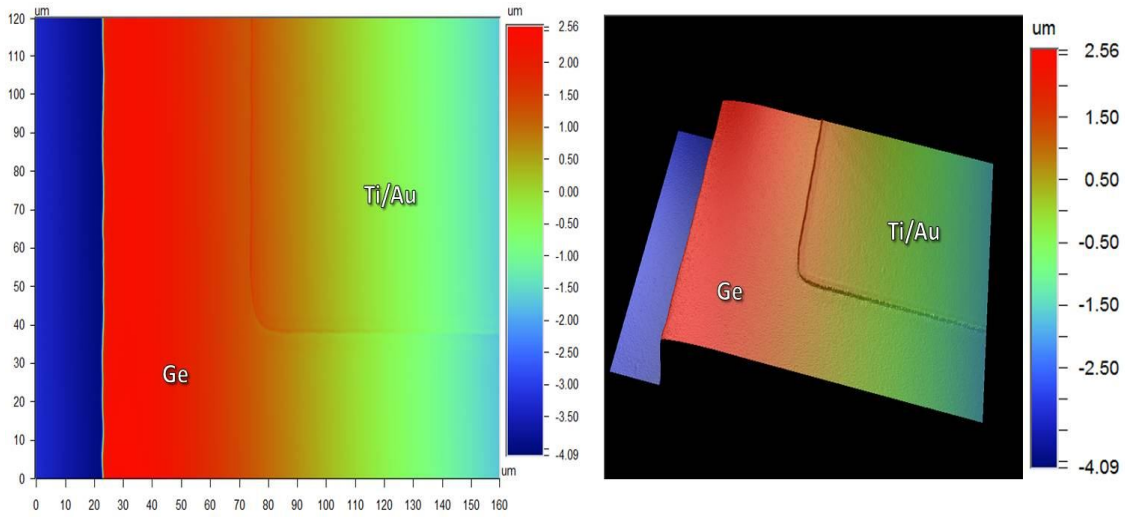

(a) (b)

Figure 3.25: 3D optical surface profilometer images of electrical pads using Ti/Au for wavelength selective Germanium dielectric coated Salisbury screen microbolometer: (a) top view, (b) cross section view.

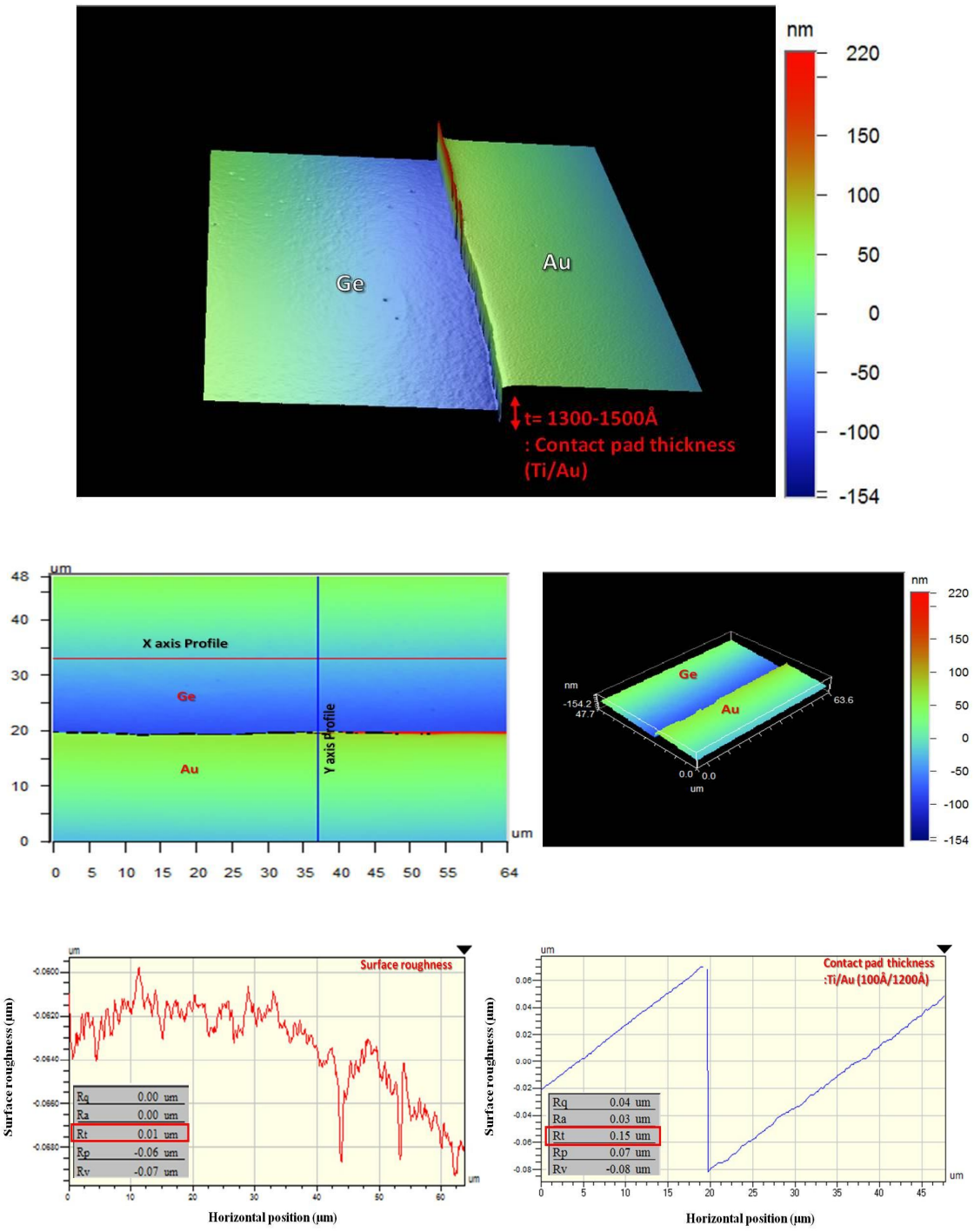

Figure 3.26: 3D optical surface profilometer images of electrical contact pads (Ti/Au) and Germanium structure layer after relatively long oxygen plasma exposure time during the ashing process.

3.6 THE PROCESS FOR WAVELENGTH SELECTIVE GERMANIUM DIELECTRIC SALISBURY SCREEN MICROBOLOMETERS USING SELF ALIGN PROCESS

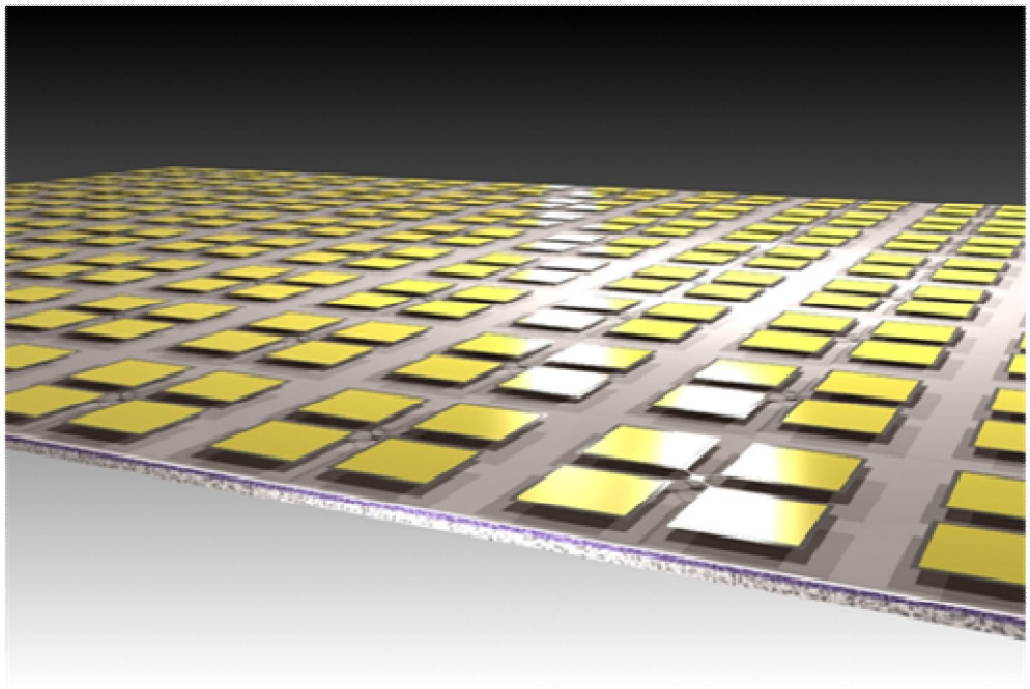

Figure 3.27: Illustration of wavelength selective Germanium dielectric coated Salisbury screen microbolometer arrays using self aligned process.

In this section, fabrication of wavelength selective Germanium dielectric coated Salisbury screen microbolometer using a self aligned process will be discussed.

Figure 3.27 shows the illustration of wavelength selective Germanium dielectric coated Salisbury screen microbolometer arrays using a planar self-aligned process [28]. The novel fabrication process helps produce much flatter, more robust device structure by using an un-patterned sacrificial layer to produce device legs that hold the central structural layer above the reflective mirror supported by a completely flat sacrificial layer with sufficient thermal isolation to allow microbolometer operation.

The fabricated wavelength selective Germanium dielectric coated Salisbury screen microbolometer using a self aligned process consist of a metal resistive sheet of 400Ω/□ as an infrared absorber layer, dielectric Germanium structure layer for structure/interference layer, reflective mirror layer and electrical contact pads. The configuration of device is shown in Figure 3.28.

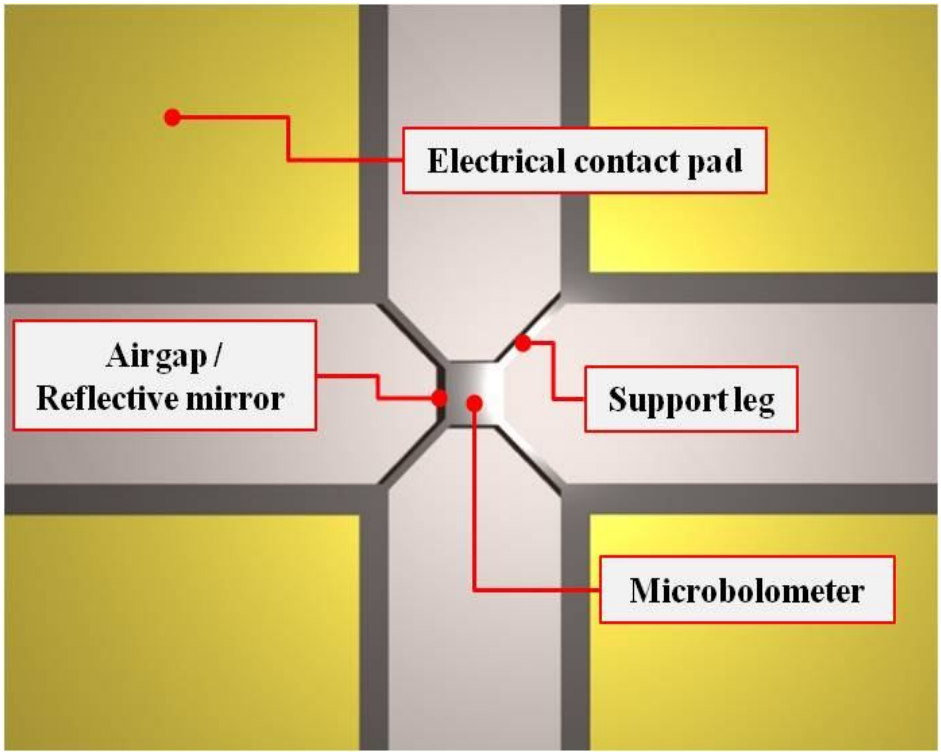

Figure 3.28: Configuration of wavelength selective Germanium dielectric coated Salisbury screen microbolometer using self aligned process.

The critical step in this fabrication process is the undercut removal of the sacrificial layer that creates the air gap under the structural layer as well as undercutting the support leg providing thermal isolation for the microbolometer. This process also

undercuts the edges of the contact pad, forming a shadow mask which produces self-aligned formation of electrical contact to the infrared absorber/microbolometer layer. In general, process of sacrificial layer patterning is considered to be one of the important steps in conventional microbolometer fabrication due to produce thermal isolation structure.

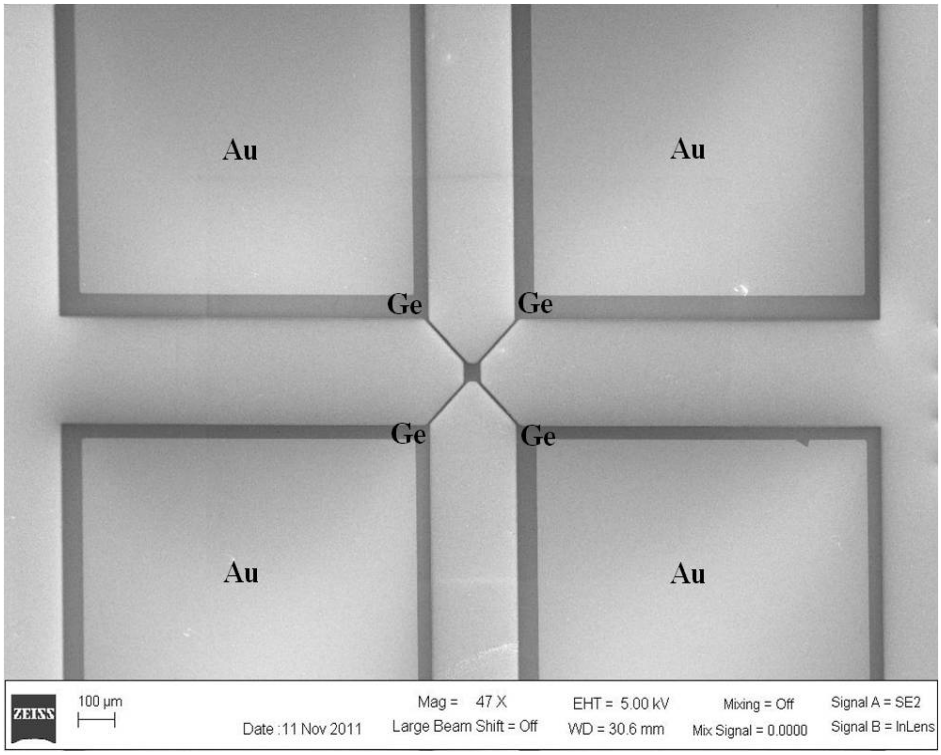

Figure 3.29: SEM image of wavelength selective Germanium dielectric coated Salisbury screen microbolometer arrays using self aligned process.

Figure 3.29 shows fabricated wavelength selective Germanium dielectric coated Salisbury screen microbolometer using a self aligned process. Microbolometer dimension is 50µm by 50µm with 15µm leg width, and 150µm leg length. Complete removal of the

sacrificial layer and highly flattened structure of the fabricated device can be seen in Figure 3.30.

In this study, different design devices were fabricated with different device active areas, leg lengths and leg widths (Figure 3.31). For device absorber materials, metal bolometer absorbers (Ni, Ti, Cr, and TaN) were employed. Mask design parameters are shown in Table 3.1.

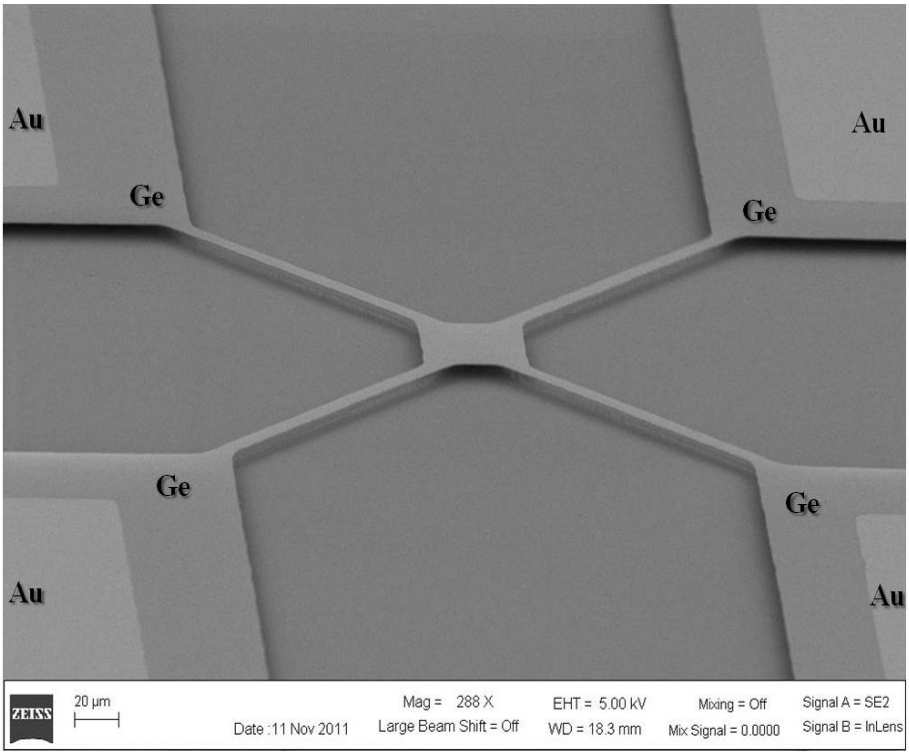

Figure 3.30: SEM images of wavelength selective Germanium dielectric coated Salisbury screen microbolometer arrays using self aligned process.

	Active area (µm)	Leg width (µm)	Leg length (µm)
1	**30x30**	**10**	**25**
2	**30x30**	**10**	**50**
3	**30x30**	**10**	**100**
4	**50x50**	**10**	**20**
5	**50x50**	**10**	**40**
6	**50x50**	**15**	**50**
7	**50x50**	**15**	**100**
8	**50x50**	**15**	**150**
9	**70x70**	**10**	**20**
10	**70x70**	**20**	**50**
11	**70x70**	**20**	**100**
12	**70x70**	**20**	**150**
13	**100x100**	**15**	**50**
14	**100x100**	**20**	**100**
15	**100x100**	**20**	**150**
16	**150x150**	**15**	**100**
17	**150x150**	**20**	**200**

Table 3.1: Mask design parameters of wavelength selective Germanium dielectric coated Salisbury screen microbolometer.

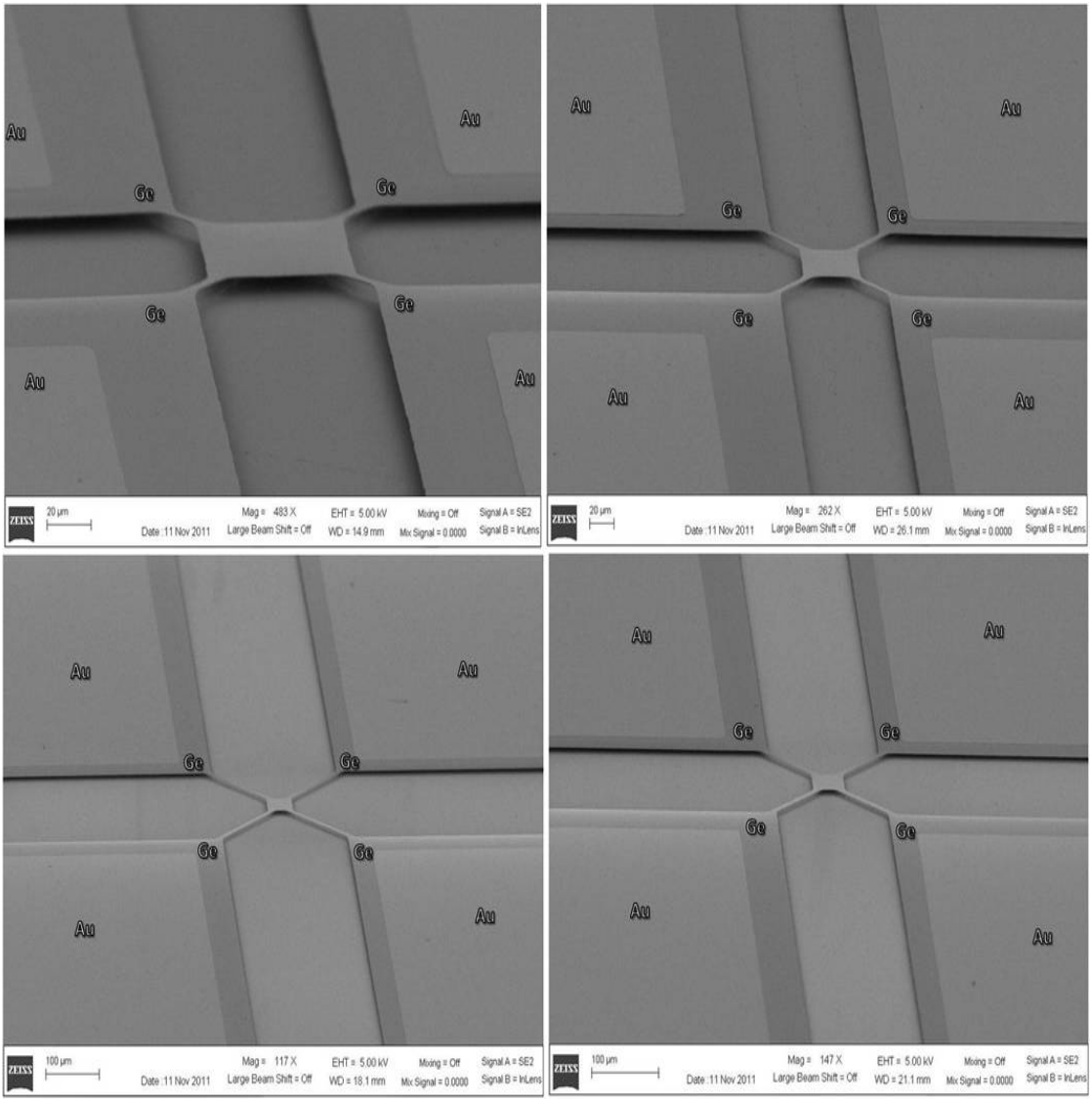

Figure 3.31: SEM image of fabricated different devices with different microbolometer active area, leg length and width, and different metallic absorber materials.

Figure 3.32 shows the device fabrication process flow that simultaneously forms self-aligned contact pads and produces flat support legs.

The process starts with thermal oxidation: the substrate (Si) is thermally oxidized to achieve an insulation layer with a thickness 0.7μm. The next step in the process is formation of infrared reflective mirror layer on a silicon dioxide layer: Lift-off process technique using photolithography and e-beam evaporation of Aluminum (film thickness: 150nm, evaporation rate: 0.5Å/sec).

Next, a controlled thickness "polyimide sacrificial" layer is coated and cured using programmable temperature controlled vacuum oven. This is one of the critical steps, since if this process is unstable, it is hard to achieve specific air gap space based on design parameters of the resonant cavity ($t_{air} = \lambda/2$; t=space of air gap, λ=target wavelength).

A controlled thickness Germanium structural layer is then deposited using e-beam evaporator over polyimide sacrificial layer ($t_{Ge\ Structure} = \lambda/4n$; t=thickness of Germanium structural layer, n=index of refraction of structural layer, λ=target wavelength).

The formation of Germanium structural layer by photolithography and dry etching process with a CF_4 using reactive ion etching (RIE) is shown in Figure 3.32 (a). In the next step, for the formation of metal contact pads, bi-layer lift-off process was chosen instead of standard lift-off technique, as shown in Figure 3.32 (b) to Figure 3.32 (c).

Since double lift-off layers are used to create a more stable lift-off process of the metal layer for contact pads, Titanium (film thickness: 20nm, evaporation rate: 0.3Å/sec) and Au (film thickness: 150nm, evaporation rate: 0.5Å/sec) were deposited by e-beam evaporation as materials of contact pads.

The sacrificial layer was then removed, to form the air gap below the microbolometer structural layer using an oxygen plasma ashing process, as shown in Figure 3.32 (d).

Finally, the resistive absorber layer with the appropriate sheet resistance is deposited using sputtering systems or e-beam evaporation systems depend on absorber material in Figure 3.32 (e).

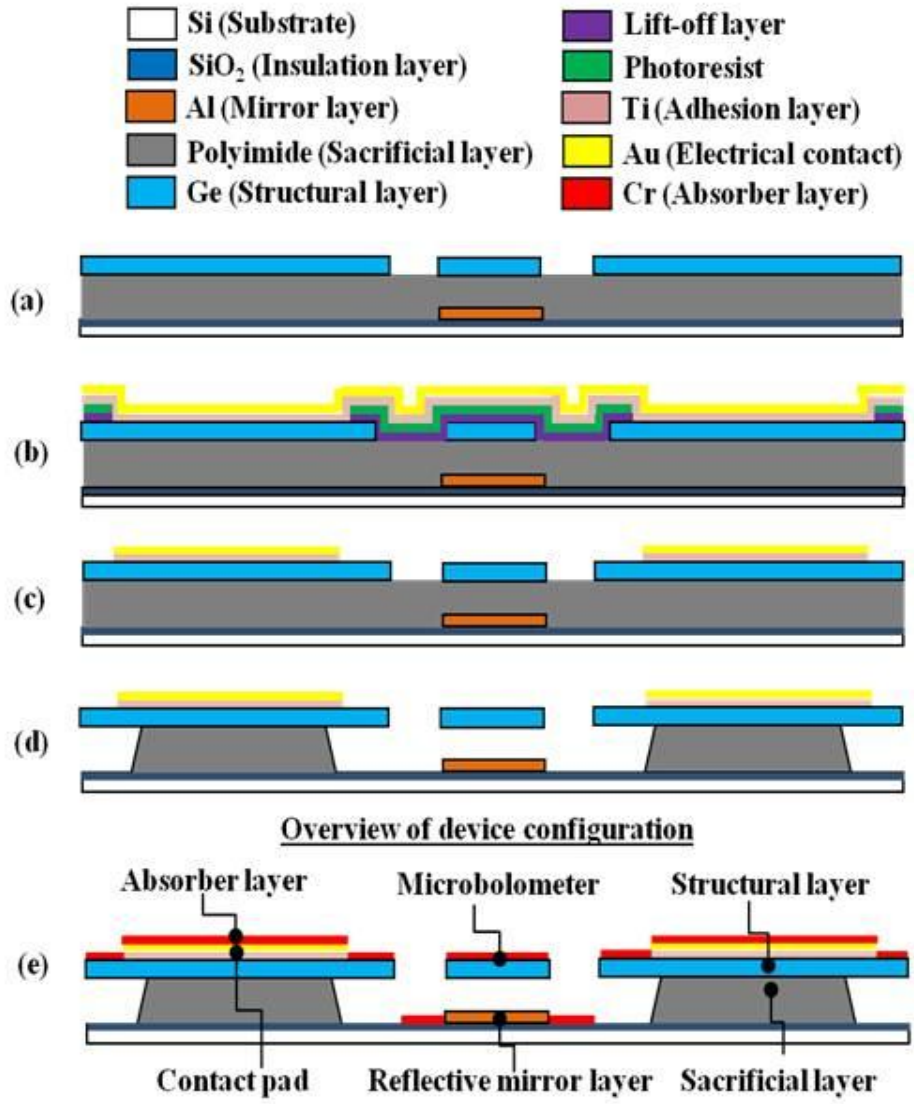

Figure 3.32: Simplified fabrication process flow of wavelength selective Germanium dielectric coated Salisbury screen microbolometer arrays using self aligned process.

Chapter 4: Device Characterization

In this chapter, several characteristics of the fabricated devices are evaluated. The characterization includes 3D optical surface profilometer and infrared optical measurement of the spectral responses of wavelength selective Germanium dielectric Salisbury screen microbolometer using Fourier transform infrared spectroscopy (FTIR). Electrical measurements were also performed, including IV curve, RP plot, thermal impedance and Temperature Coefficient of Resistance (TCR).

4.1 Optical Measurement of Wavelength Selectivity using Fourier Transform Infrared Spectroscopy (FTIR)

4.1.1 Spectral Responses of Wavelength Selective Germanium Dielectric Salisbury Screen Microbolometer using Self align Process: Wavelength Selectivity in the Long Wavelength Infrared (LWIR) Region

To characterize the spectral response of the wavelength selective Germanium dielectric Salisbury screen microbolometer using self align process, Fourier transform infrared (FTIR) microscopy measurements were taken on a number of the fabricated devices using Nicolet ^{TM} 6700 FTIR spectrometer.

This FTIR spectrometer employs a cooled HgCdTe (MCT) detector with a spectral resolution of ~0.09 cm^{-1} and Nicolet TM imaging system at room temperature in a standard lab atmosphere. In order to produce the maximum power absorption, the sheet resistive absorber layers of the Salisbury screen need to have sheet resistance R_S=377 Ω/□, by controlling the thickness of the absorber layer (In Section 4.1, Tantalum nitride (TaN) and Chromium (Cr) is used as absorber layer). To verify the DC sheet resistance of the absorber layer, four point probe measurement is performed.

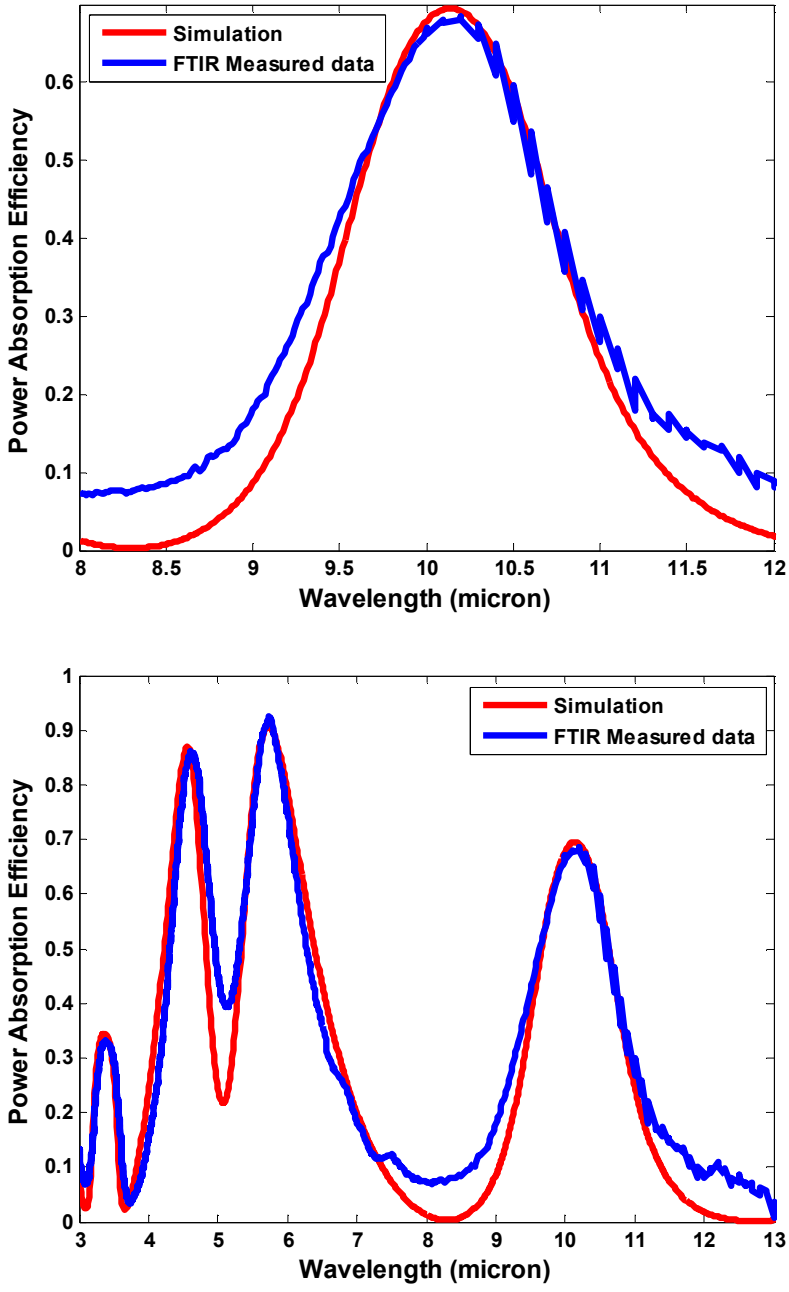

Figure 4.1: Numerical simulation of infrared spectral responses (red curve) and FTIR measured infrared spectral responses of Germanium dielectric coated Salisbury screen microbolometer for wavelength selectivity in long wave infrared region (blue curve): Targeted wavelength absorption peak: 10μm.

Figures 4.1, 4.2, and 4.3 show a comparison between simulation results (red curve) and measured spectral responses (blue curve) using FTIR for wavelength selective Germanium dielectric Salisbury screen microbolometer using self align process (Chromium: Cr as absorber layer). To achieve wavelength selectivity in the long wavelength infrared (LWIR) region, three different devices were designed and fabricated, for three different wavelengths (9μm, 10μm, 11μm). Figures 4.1, 4.2 and 4.3 show the comparison for the different device parameters, for different target wavelengths, i.e., 10μm, 9μm and 11μm, respectively.

In Figure 4.1, the fabricated device parameters are as follows: Germanium thickness is around 0.6μm (experimental target thickness: 0.625μm), air gap is 5μm, sheet resistance of Cr absorber layer is 400Ω/□. The target wavelength peak is 10μm.

In Figure 4.2, the fabricated device parameters are Germanium thickness: around 0.6μm (experimental target thickness: 0.625μm), air gap: 4.5μm, sheet resistance of Cr absorber layer: 400Ω/□. The target wavelength peak is 9μm.

In Figure 4.3, the fabricated device parameters are Germanium thickness: around 0.6μm (experimental target thickness: 0.625μm), air gap: 5.5μm, sheet resistance of Cr absorber layer: 400Ω/□. The target wavelength peak is 11μm and measured maximum power absorption is over 90%.

Using Chromium (Cr) absorber layer in the device, the FTIR measured spectral responses and numerical simulation results show excellent agreement in LWIR region.

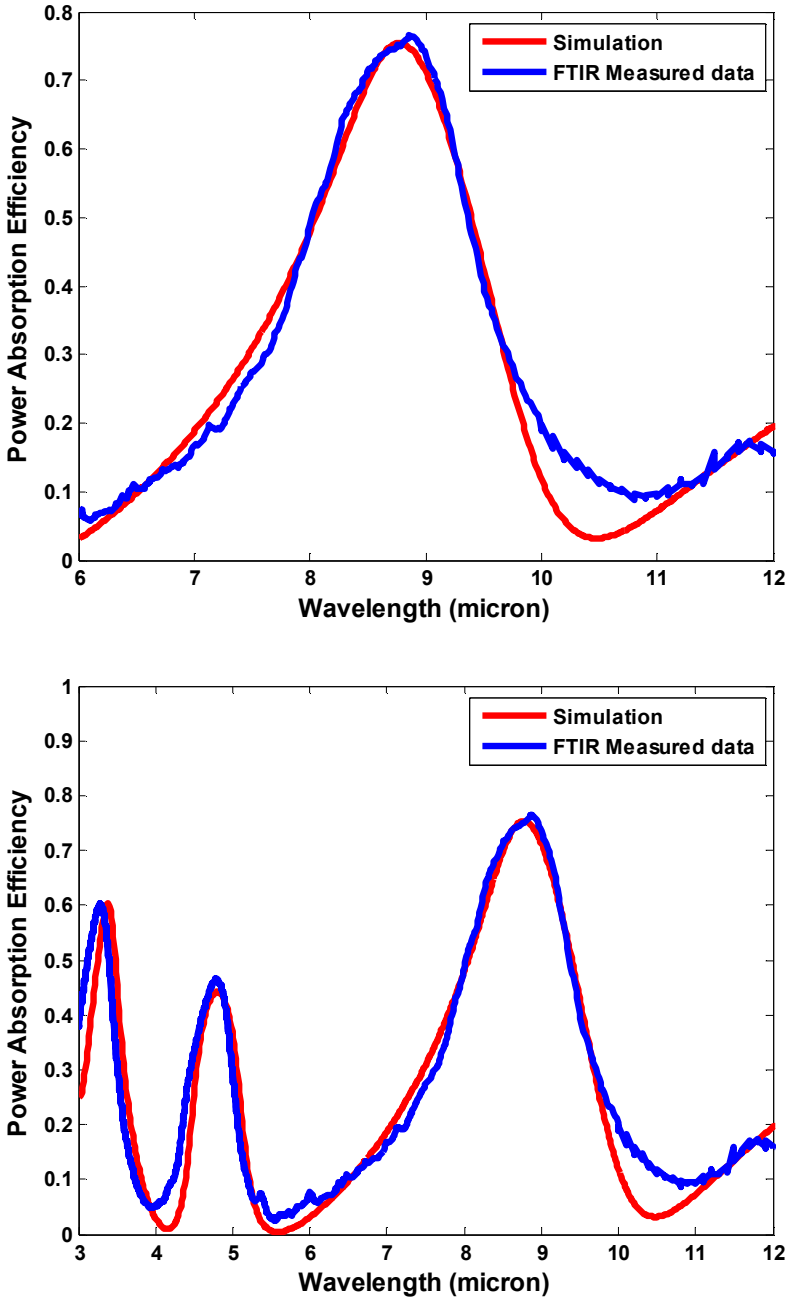

Figure 4.2: Numerical simulation of infrared spectral responses (red curve) and FTIR measured infrared spectral responses of Germanium dielectric coated Salisbury screen microbolometer for wavelength selectivity in long wave infrared region (blue curve): Targeted wavelength absorption peak: 9μm.

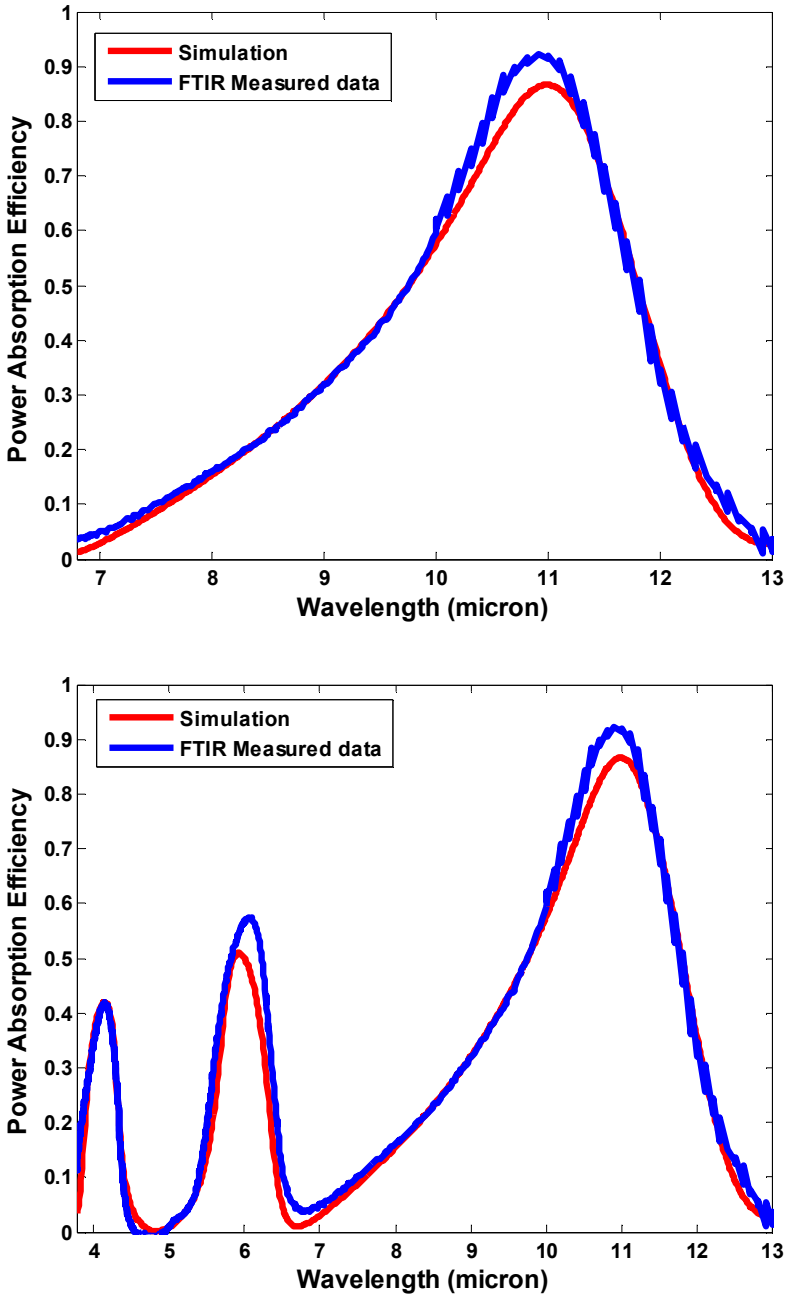

Figure 4.3: Numerical simulation of infrared spectral responses (red curve) and FTIR measured infrared spectral responses of Germanium dielectric coated Salisbury screen microbolometer for wavelength selectivity in long wave infrared region (blue curve): Targeted wavelength absorption peak: 11μm.

Another set of devices were designed and fabricated, with a different absorber layer, namely Tantalum nitride (TaN). Simulation and measured results have also been compared for these devices in the following figures.

Figures 4.4 and 4.5 show the comparison between simulation results (red curve) and measured spectral responses (blue curve) using FTIR for wavelength selective Germanium dielectric Salisbury screen microbolometer using self align process, with Tantalum nitride TaN as absorber layer.

In Figure 4.4, the fabricated device parameters are Germanium thickness: around 0.6 μm (experimental target thickness: 0.625μm), air gap: 4.5μm, sheet resistance of Cr absorber layer: 400Ω/□. The target wavelength peak is 9μm.

In Figure 4.5, the fabricated device parameters are Germanium thickness: around 0.6 μm (experimental target thickness: 0.625μm), air gap: 5μm, sheet resistance of TaN absorber layer: 400Ω/□. The target wavelength peak is 10μm.

Both of the target wavelengths (9μm and 10μm) in the long wavelength infrared (LWIR) using Tantalum nitride as absorber layer, the FTIR measured spectral responses show excellent agreement with numerical simulation results.

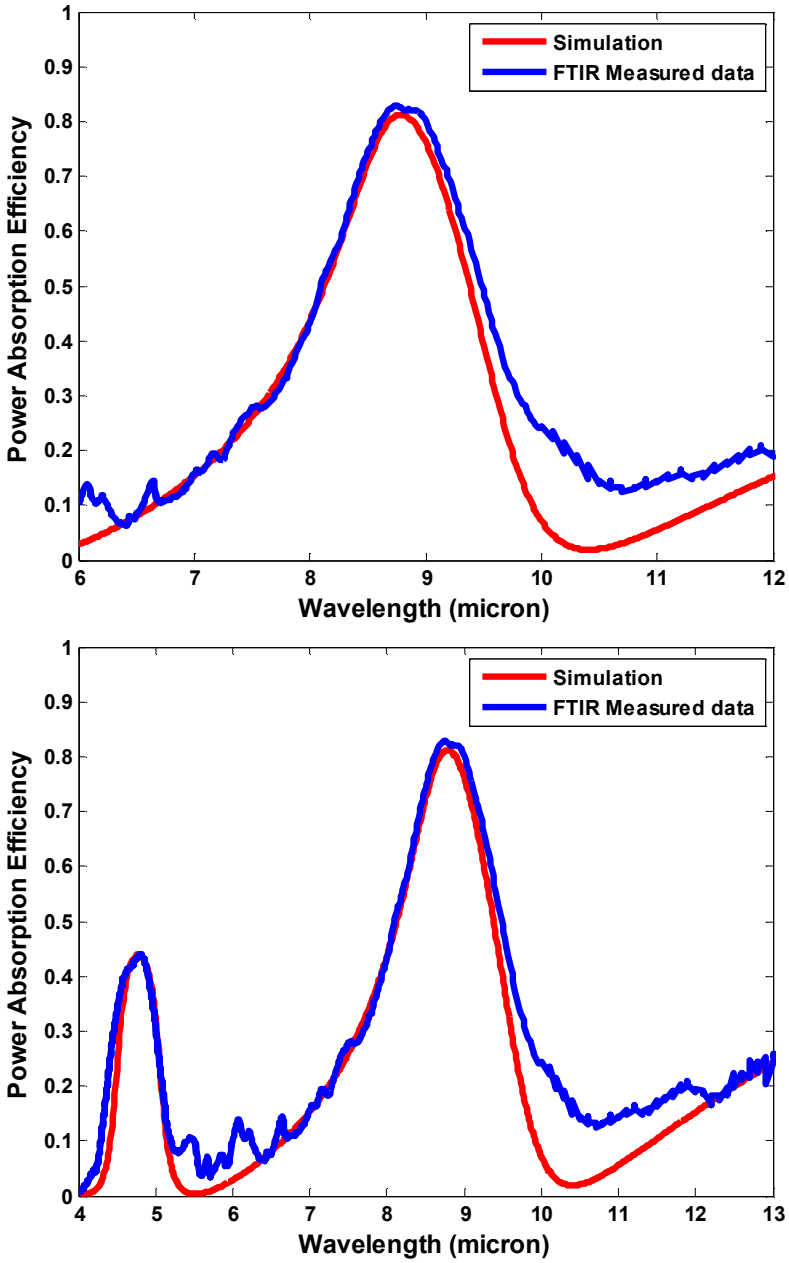

Figure 4.4: Numerical simulation of infrared spectral responses (red curve) and FTIR measured infrared spectral responses of Germanium dielectric coated Salisbury screen microbolometer for wavelength selectivity in long wave infrared region (blue curve): Targeted wavelength absorption peak: 9μm.

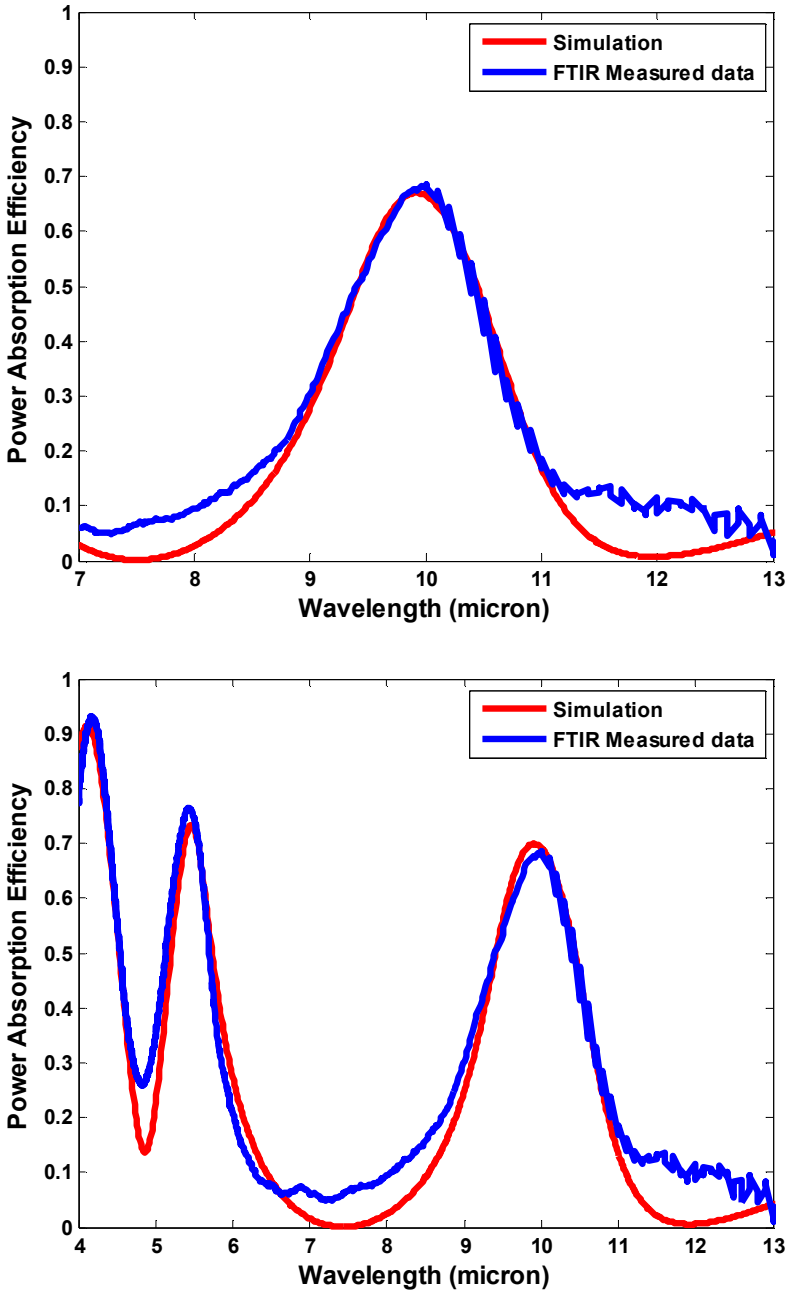

Figure 4.5: Numerical simulation of infrared spectral responses (red curve) and FTIR measured infrared spectral responses of Germanium dielectric coated Salisbury screen microbolometer for wavelength selectivity in long wave infrared region (blue curve): Targeted wavelength absorption peak: 10μm.

4.1.2 Spectral Responses of Germanium Dielectric Salisbury Screen (DSS) with Low Air gap (around 2μm) and Non-Uniform Air gap

To characterize the spectral response of the general Germanium Dielectric Salisbury Screen (DSS) devices (discussed in the Chapter 3), FTIR microscope measurements were taken on a number of the fabricated devices. In this section, FTIR-microscope data were collected by QinetiQ North America and Ani Weling, Fost-Miller. They were all collected in reflectance with a 30 x 30 μm FOV using a gold slide reference.

Figure 4.6 shows typical measured FTIR microscope absorption data (blue curve) for a DSS pixel (with an air gap) with a Germanium layer of physical thickness of 0.3μm, as measured by a crystal monitor. The air gap physical thickness is set by the polyimide sacrificial layer thickness, and is measured using an Alpha Step profilometer to be 1.7μm. The TaN absorber layer is approximately 25nm thick and has a measured DC sheet resistance of R_s = 400Ω/□. Figure 4.6 also compares the measurement with numerically simulated result. The numerical simulation uses thicknesses obtained from a best fit of the location of the peaks along the wavelength axis. It should be noted that in the plane wave model the layer thicknesses and indices of refraction primarily affect the behavior along the wavelength axis (i.e., position of absorbance resonance), while the sheet resistance of the absorber primarily determines the heights of the absorption peaks (although the indices of refraction do somewhat affect the peak heights).

The fabricated DSS device has a measured sheet resistance of R_s = 400Ω/□; the measured data should thus agree with the simulation with R_s = 400Ω/□ (red curve). The location of the absorption resonance along the wavelength axis for the fabricated DSS device matches well with the simulation results. However, the fabricated device shows less absorption than the simulation with R_s = 400Ω/□.

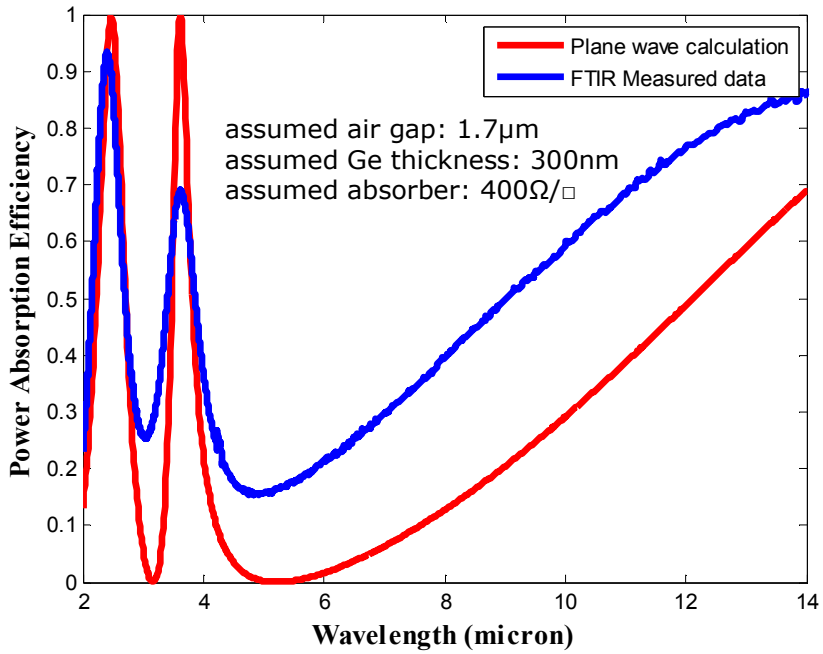

Figure 4.6: FTIR microscope measured absorption data (blue curve) for DSS microbolometer with thickness of Ge $d_1 = 0.3\mu m$, air gap thickness $d_2 = 1.7\mu m$, and TaN absorber layer ($R_s = 400\Omega/\square$) compared to plane wave calculations for the same structure with sheet resistances $R_s = 400\Omega/\square$ (red curve).

As discussed above, the DSS with sheet resistance $R_s = 400\Omega/\square$ of TaN absorber layer should have produced better absorption than the measured data shown in Figure 4.6. One possibility is that the infrared absorption properties of the TaN sheet are different from the DC measurement. To illustrate the effect of changing sheet resistance, Figures

4.7 and 4.8 show the simulated spectral response compared to measured results for two assumed sheet resistances: lower sheet resistances (Figure 4.7) than the ideal sheet resistance R_s = 400Ω/□, and higher sheet resistance (Figure 4.8). It is possible to fit the height of one peak, but the other peak is not well matched. Also the spectral width for the high resistance value is narrower than the measured result. As discussed above, these differences suggest that a discrepancy in R_s is not the cause of the discrepancy between the simulation model and FTIR measurements.

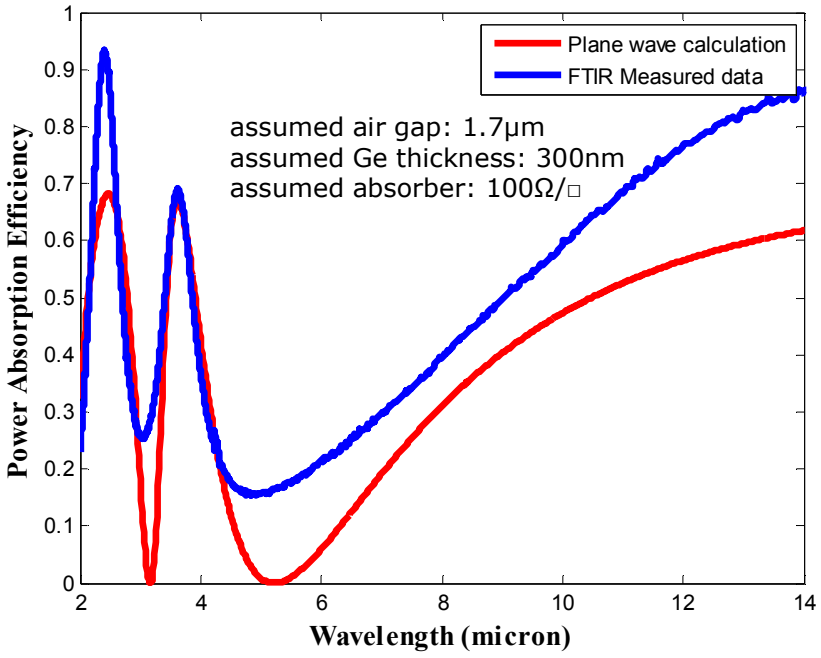

Figure 4.7: FTIR-microscope-measured absorption data (blue curve) for DSS compared to plane wave calculated power absorption curve (red) for a sheet absorber with sheet resistance R_s = 100Ω/□.

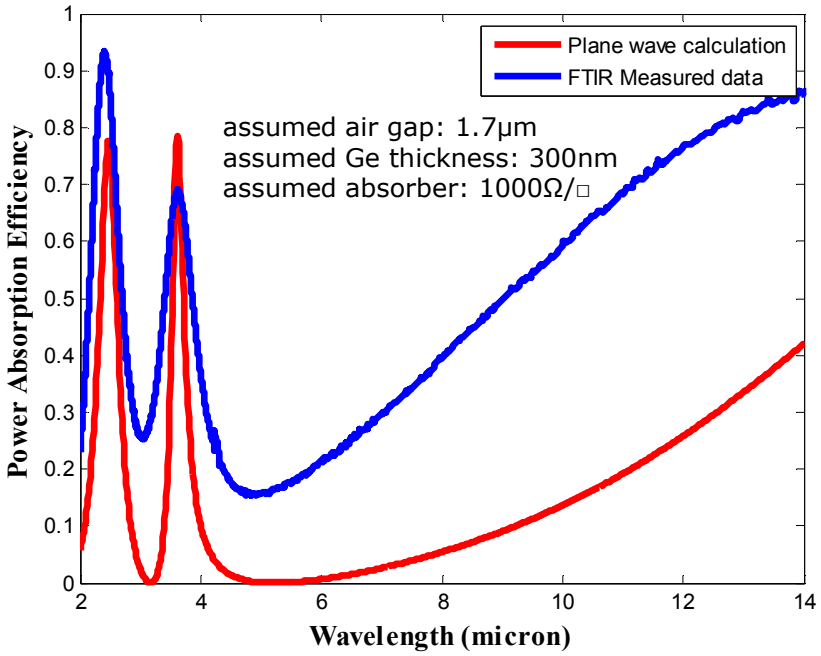

Figure 4.8: FTIR-microscope-measured absorption data (blue curve) for DSS compared to plane wave calculated power absorption curve (red) for a sheet absorber with sheet resistance $R_s = 1000\Omega/\square$.

These discrepancies may more likely be caused by non-uniform air gaps, rather than changes in sheet resistance. To examine if this could affect the spectral absorption response, a known variation in air gap thickness is assumed to exist across the DSS pixel.

Figure 4.9 shows the FTIR measured data (blue curve) for the DSS with a Ge thickness $d_1 = 0.3\mu m$, nominal air gap thickness $d_2 = 1.7\mu m$, and TaN absorber layer ($R_s = 400\Omega/\square$). Also shown is the plane-wave simulation result when averaged over air gaps varying over the range $1.7\mu m \pm 0.06\mu m$, i.e., by 3.5%. For a perfectly uniform air gap, the peak of the absorption curve is very resonant (i.e., ~100%) while its position is quite sensitive to the specific value of the air gap. However, when the pixel response is

averaged over many air-gap values, it leads to an overall drop in the peaks of the absorption curve.

Figure 4.10 shows the FTIR-measured data (blue curve) for the DSS compared to the simulation result when averaged over air gaps varying over a range of 8% (red curve). Both absorption peak heights appear to align well, suggesting that non-uniformity of air gap is a likely cause of the change in response (observed in Figure 4.6).

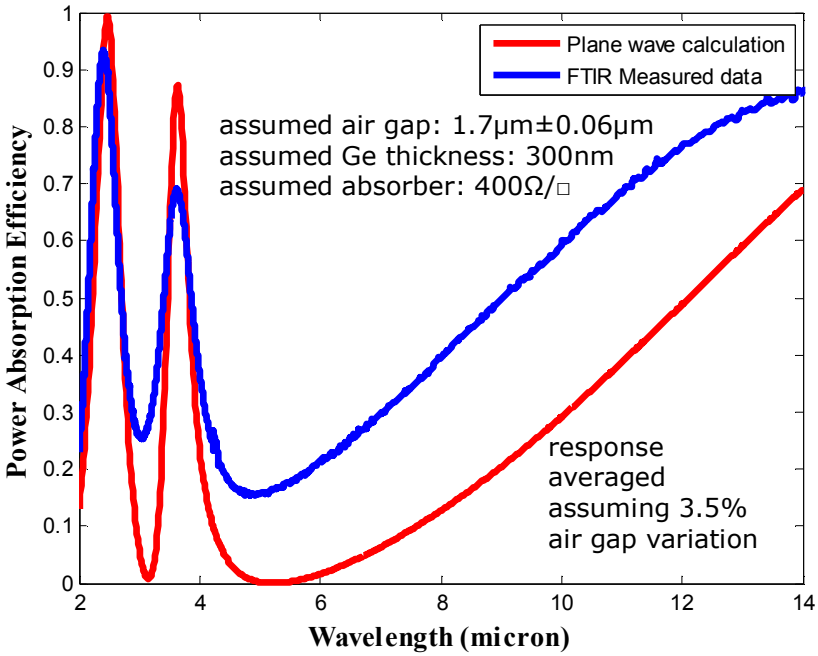

Figure 4.9: FTIR-microscope-measured absorption data (blue curve) for DSS with thickness of Ge d_1 = 0.3μm, air gap thickness d_2 = 1.7μm, and TaN absorber layer (R_s = 400Ω/□) compared to plane wave calculation averaging over air gap thicknesses varying by 3.5% (red).

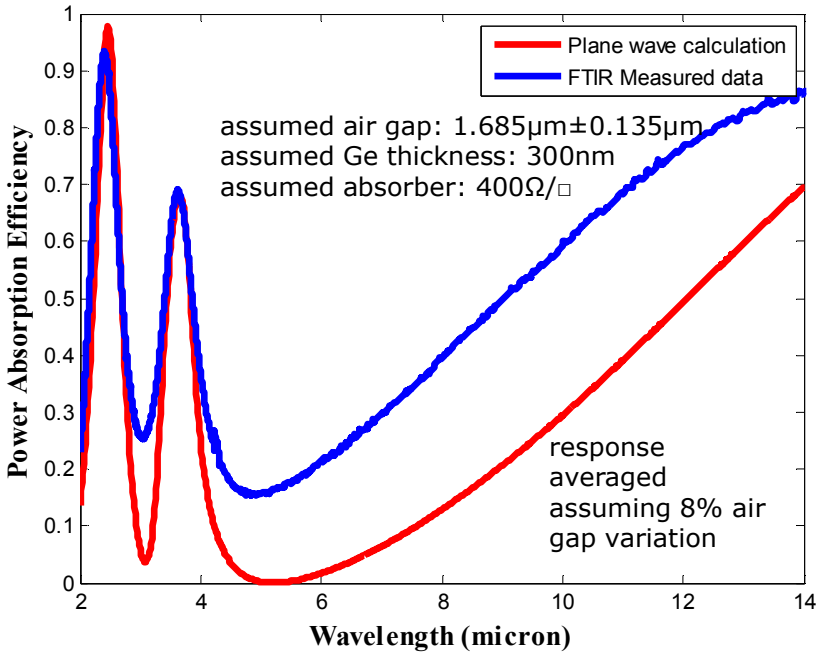

Figure 4.10: FTIR-microscope-measured absorption data (blue curve) for modified DSS with thickness of Ge d_1 = 0.3μm, air gap thickness d_2 = 1.7μm, and TaN absorber layer (R_s = 400Ω/□) compared to plane wave calculation averaging over air gap thicknesses varying by 8% (red).

4.2 DEVICE STRUCTURE CHARACTERIZATION USING 3D OPTICAL PROFILOMETER

To characterize the low deformation membranes, 3D optical surface profilometry has been used to measure the surface shape of devices. These measurements were made using a Veeco-Wyko NT 9100 Optical Profiler system. Figure 4.11 shows 3D device structure profile result obtained from the Veeco system. Each leg is 150µm long and 15µm wide, and the area of absorber is 50 µm by 50µm, in the fabricated device. Figure 4.12 shows that there is excellent agreement between the X and Y cross sectional profiles, obtained along the indicated axes in Figure 4.12(a). The cross sectional profiles are shown in Figure 4.12 (b) and Figure 4.12 (c). This confirms that the structural layer is a low deformation (high flatness) membrane with a uniform air gap. The flatness of the structure is a key parameter, which improves the performance of the microbolometer leading to enhanced infrared absorption.

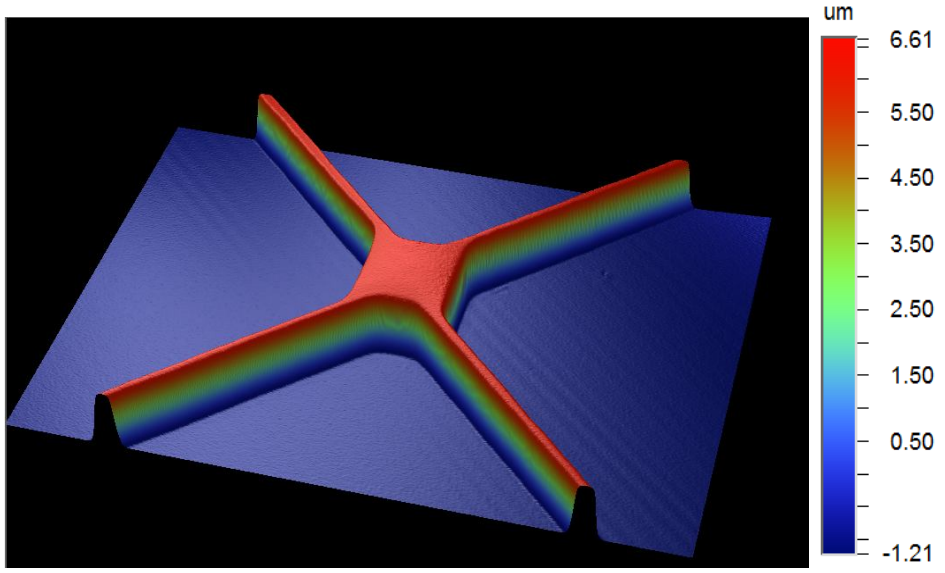

Figure 4.11: 3D profile image of fabricate wavelength selective Germanium dielectric coated Salisbury screen microbolometer using a Veeco-Wyko NT9100 optical profiler.

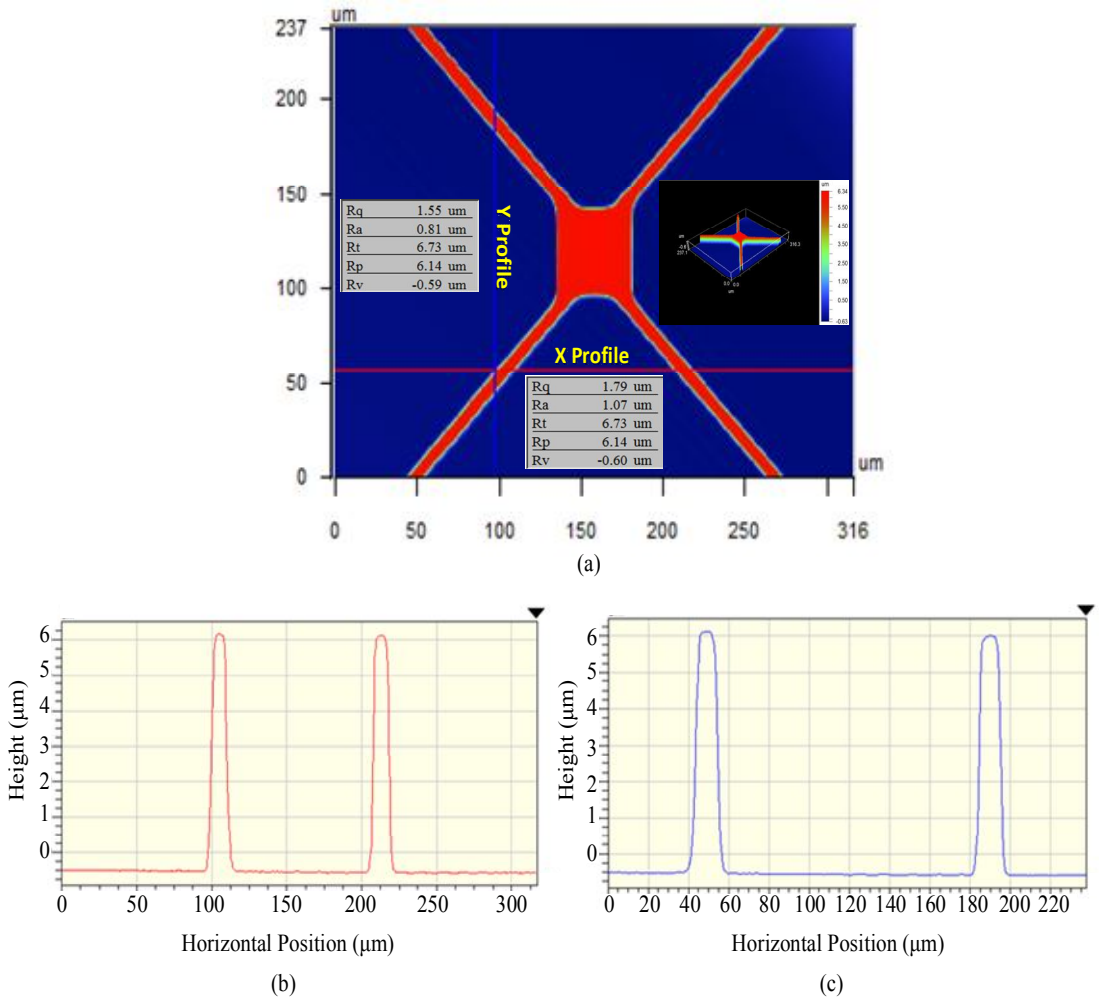

Figure 4.12: 3D optical profiler image of fabricated wavelength selective Germanium dielectric coated Salisbury screen microbolometer for low deformation membrane: (a) Top view of structure profile, (b) cross sectional profile of X axis, (c) cross sectional profile of Y axis.

4.3 SHEET RESISTANCE CONTROL WITH THICKNESS OF THIN FILM METAL ABSORBER

The sheet resistance of the resistive absorber layer is one of the major design parameters. Matching of the sheet resistance to free space (377Ω/□) leads to enhanced power absorption in the wavelength selective Germanium dielectric Salisbury screen microbolometer. The sheet resistance can be controlled by the thickness of the deposited thin film metal absorber.

Figures 4.13, 4.14, and 4.15 show experimental results of the sheet resistance variation with thin film thickness in Nickel (Ni), Titanium (Ti) and Chromium (Cr), which are typically used metal absorbers in microbolometers. The thin films were deposited using e-beam evaporation.

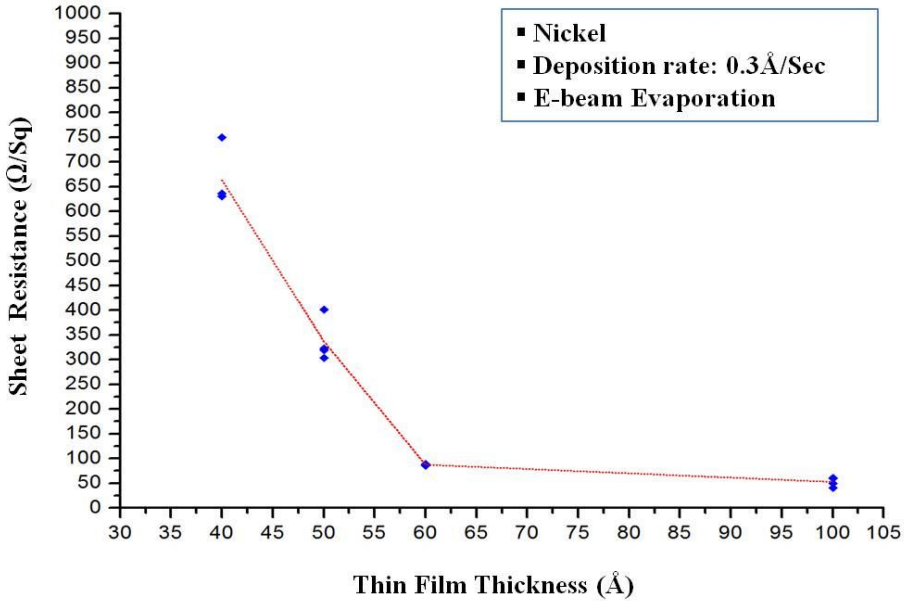

Figure 4.13: Sheet resistance vs. Metal absorber layer thickness (Nickel: Ni).

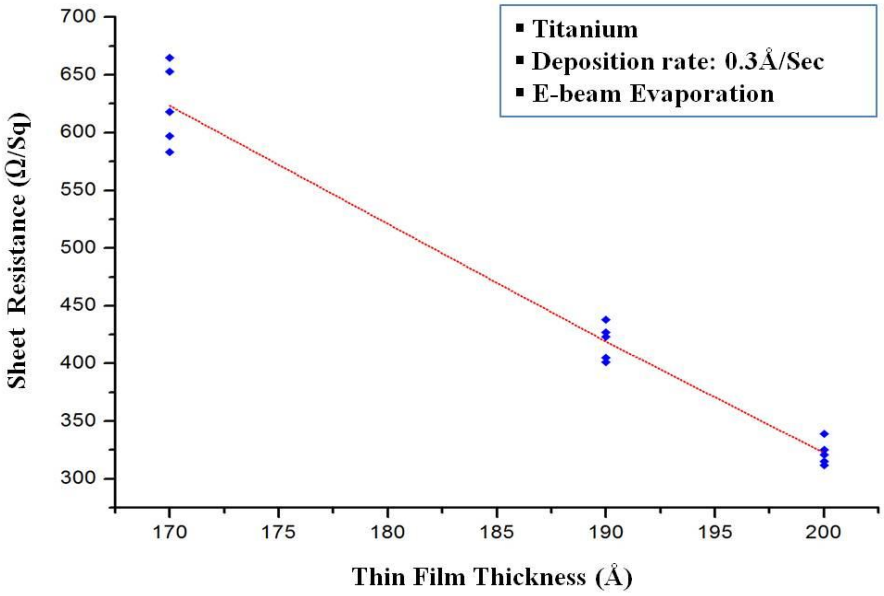

Figure 4.14: Sheet resistance vs. Metal absorber layer thickness (Titanium: Ti).

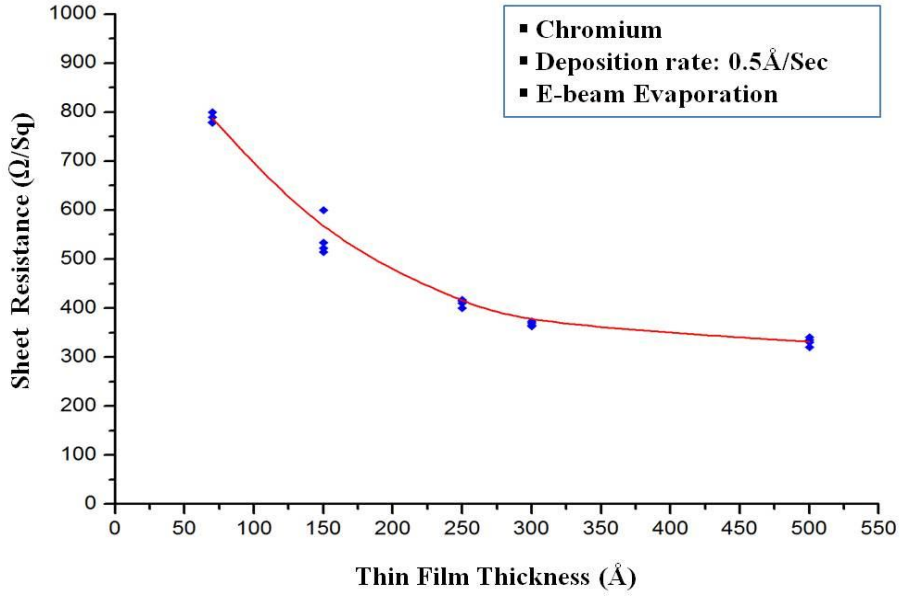

Figure 4.15: Sheet resistance vs. Metal absorber layer thickness (Chromium: Cr).

4.4 PASSIVATION LAYER OF OXYGEN PLASMA EXPOSURE USING GERMANIUM LAYER

In this section, a passivation method for the absorber layer is presented, which is performed during oxygen based plasma ashing process. An important step in the fabrication of thermally isolated structures for the proposed wavelength-selective microbolometer is the ability to define electrical contacts to the Germanium dielectric coated Salisbury Screen (DSS) pixel with Chromium absorber layer. Ideally this should be done lithographically before the Ge-supported membranes are released to define the air gap. Since the Chromium layer has been shown to be oxidized by the plasma ashing required to remove the polyimide sacrificial layer used to define the air gap, the current process flow would have to be changed significantly in order to protect the top Chromium absorber layer during the final membrane release step. A Germanium passivation layer has been developed, which can achieve this without altering the process sequence.

Figure 4.16 illustrates a basic electrical test, which shows that a very thin layer of Germanium deposited above the Chromium absorber layer can protect it from even very long oxygen plasma exposures. Ellipsometer measurements suggest that a layer of oxide is formed on top of the Ge, although this layer is not more than approximately 10nm thick. Nonetheless, the sheet resistance of the Chromium absorber layer is almost unchanged.

Figure 4.17 shows the FTIR reflectance results from a set of Germanium dielectric coated Salisbury screen samples. These samples use a $\lambda/4$ thick (at 10μm) Ge layer deposited directly on top of an Al mirror, with the usual Chromium absorber (sheet resistance ~ 400Ω/□). These are then covered with a final 50nm thick Germanium passivation layer. As can be seen from the data, the thin Germanium passivation layer does not significantly alter the expected reflectance spectra from the DSS structure, but

more importantly, protects this structure even after 10 hours of oxygen plasma exposure. This experimental method is also applicable to 3D stacked microbolometer fabrication for passivation of two absorber layers during oxygen plasma ashing process.

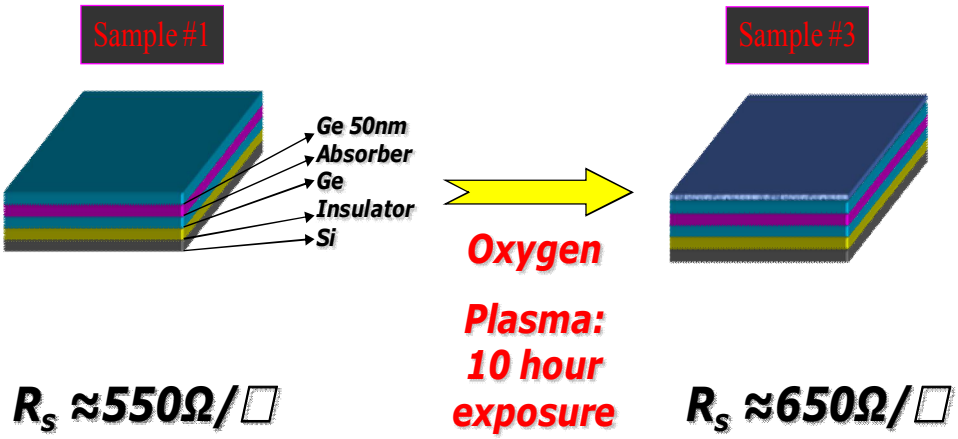

Figure 4.16: Illustration of Passivation of Oxygen plasma exposure using Germanium layer.

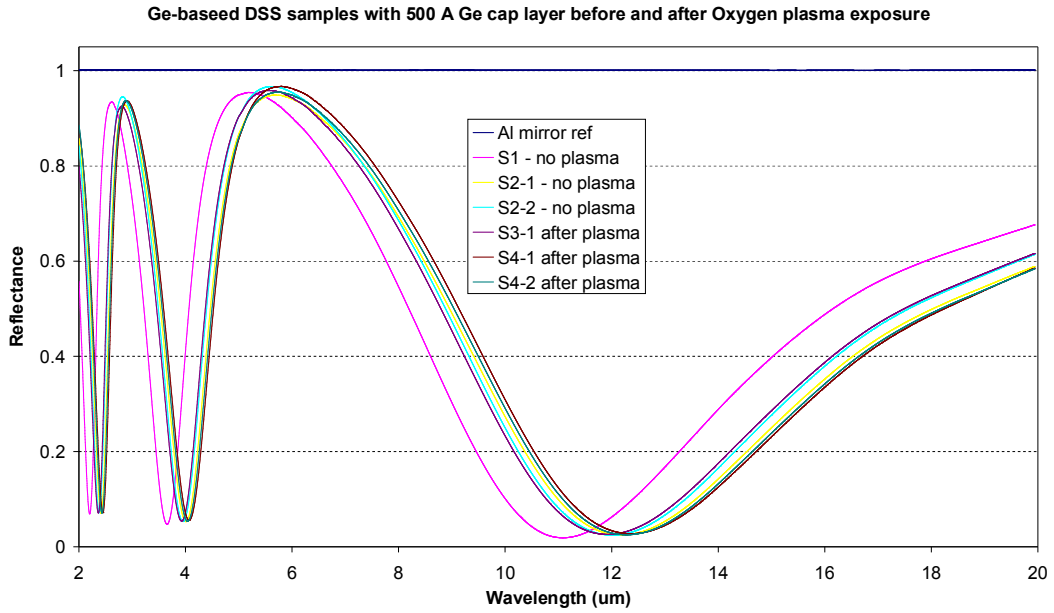

Figure 4.17: FTIR reflectance results of test sample using Germanium Passivation (FTIR measurement by Ani Weling, Fost-Miller).

4.5 ELECTRICAL MEASUREMENT

The simplest way to characterize a microbolometer is through the use of a resistance (R) – power (P) curve. This is most easily seen by considering the temperature dependence of the bolometer resistance R_{bolo} when a small amount of power is applied to the bolometer, causing the bolometer's resistance to change:

$$R_{bolo}(P) = R_o + \frac{dR_{bolo}}{dT}\frac{dT_{bolo}}{dP}\cdot P \qquad \text{Eq.4.1}$$

where R_o is the bolometer resistance at ambient temperature, T_{bolo} is the bolometer temperature, and P is the electrical power applied/dissipated that causes a

bolometer temperature change. The change in bolometer temperature with applied power is just the thermal impedance of the structure:

$$\frac{dT_{bolo}}{dP} = Z_{thermal} \quad . \qquad \text{Eq.4.2}$$

One further simplification can be made by noting that the change in resistance with temperature is related to the bolometer material's temperature coefficient of resistivity (TCR) α, given by:

$$\frac{1}{R_{bolo}} \frac{dR_{bolo}}{dT} = \alpha \quad . \qquad \text{Eq.4.3}$$

Combining these terms, the bolometer resistance R_{bolo} can be conveniently written as (in the small signal approximation):

$$R_{bolo}(P) = R_o + \alpha \cdot R_o \cdot Z_{thermal} \cdot P \quad . \qquad \text{Eq.4.4}$$

By making a simple dc current (I) vs. voltage (V) measurement these parameters can be easily extracted from the bolometer's R-P curve by noting that:

$$\underbrace{\frac{V_{bolo}}{I_{bolo}}}_{R_{bolo}} = \underbrace{R_o}_{intercept\ of\ R\text{-}P\ curve} + \underbrace{\alpha \cdot R_o \cdot Z_{thermal}}_{slope\ of\ R-P\ curve} \cdot \underbrace{\left(V_{bolo} \cdot I_{bolo}\right)}_{P_{bolo}} \quad . \qquad \text{Eq.4.5}$$

DC measurement was performed to do characterization of the electrical properties of the fabricated devices (Device dimension: leg length of 20µm, leg width of 10µm, active area of 70 µm by70 µm and structure thickness of approximately 325nm). The DC Current-Voltage measurements (Hewlett-Packard, Precision Semiconductor Parameter Analyzer: HP4156A) were performed at atmospheric pressure and room temperature. Sixty second holding and long integration time was used to ensure thermal steady measurement.

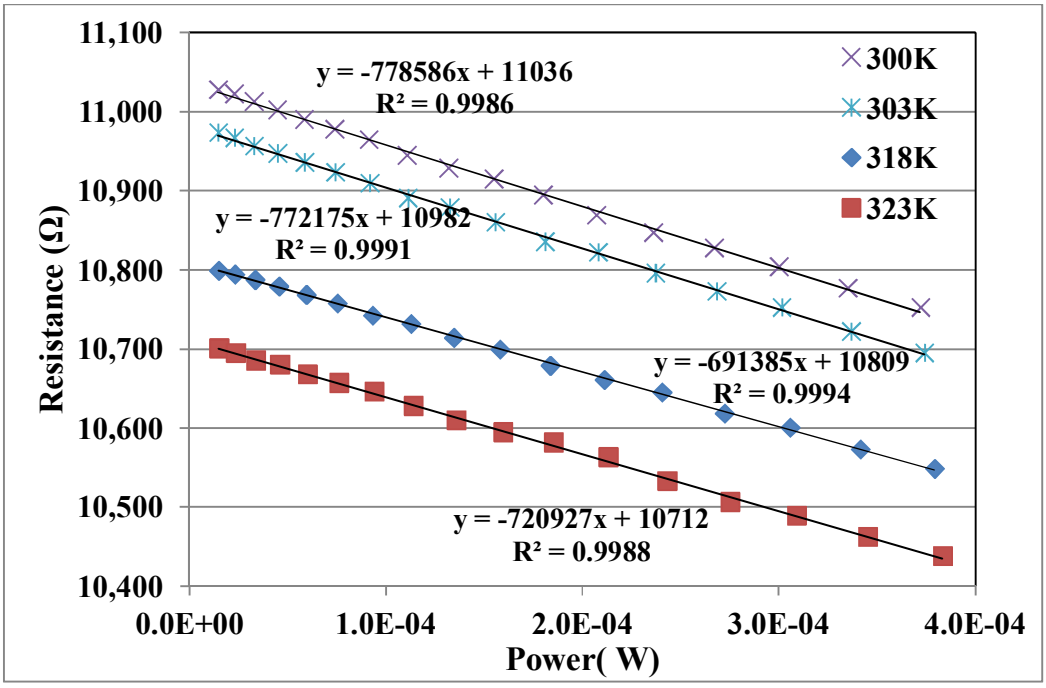

Figure 4.18: Resistance as a function of dissipated power for wavelength selective Germanium dielectric coated Salisbury screen microbolometer at various temperatures, bias voltage (0.1-2V) with step of 0.1V.

The resistance -power (R-P) plots resulting from the I-V measurements is shown in Figure 4.18. The resistance decreases as a function of increasing dissipated power

suggesting a negative Temperature Coefficient of Resistance (TCR). This desirable characteristic as it avoids the problems associated with thermal runaway and can be used in the construction of a true bolometric device. The linearity in the spacing of the curves in the R-P plot suggests a fairly constant slope (dR/dP) over the measured temperature range. The slope of the R-P plots obtained by linear regression (coefficient 0.998) yields dR/dP= 0.753 (Ω/μW), a reasonably constant value. Thus the DC responsivity can be calculated, at 100μA bias current, as 75.3V/W.

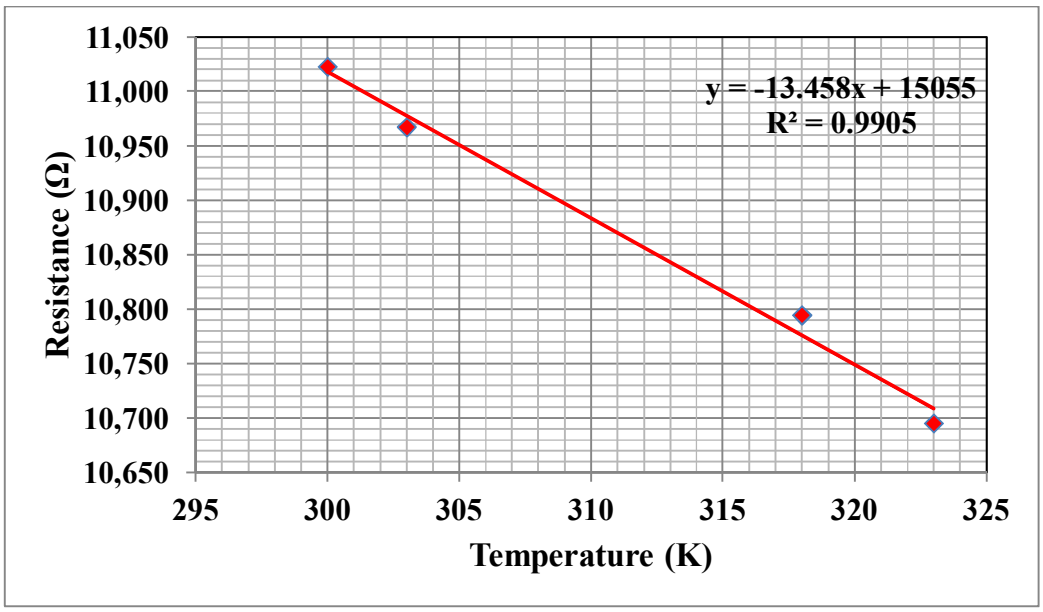

Figure 4.19: Temperature dependence of resistance for the microbolometer at a bias voltage of 0.5V.The slope yields dR/dT which can be used to estimate TCR (α).

The temperature dependence of the resistance (R-T plot) obtained from the IV measurements is shown in Figure 4.19 The slope of the R-T plot obtained by linear

regression is dR/dT = -13.458 which is a material property. The TCR for deposited TaN is calculated to be -0.0008/K. (TCR value by IBM: -0.0003/°C) [29]. The thermal impedance of the device using the estimated dR/dP and dR/dT was determined to be approximately 5.81 x 10^4 K/W.

Chapter 5: Novel 3D Stacked Microbolometers

In this chapter, the design and fabrication of novel 3D stacked microbolometer with two infrared absorbers and Germanium dielectric structural layers using self aligned process, which enables two color uncooled infrared detector, is covered.

5.1 INTRODUCTION

Conventional Fabry-perot resonant cavity based uncooled microbolometers (Air gap: 2 to 2.5μm) have limited design parameters due to multicolor narrow band spectral response. In this study, a feasible device fabrication method for novel 3D stacked microbolometer is demonstrated for multispectral uncooled infrared detector that can achieve tunable narrowband absorption in mid-wave infrared (MWIR) and long-wave infrared (LWIR) spectral range. An illustration of the novel device is shown in Figure 5.1.

In recent years, multispectral (multicolor, multichannel) infrared systems have been extensively investigated for numerous critical applications as discussed in Chapter 2. The primary spectral bands for infrared imaging are 3 to 5μm and 8 to 12μm, since atmospheric transmission is highest in these bands. Both the bands, however, differ dramatically with respect to contrast, scene characteristics, atmospheric transmission, background signal under optical aperture constraints and diverse weather conditions.

These complex combinations of system performance metrics require ideal dual band (multicolor, multichannel) operation devices. At present, as discussed in Chapter 2, commercial platforms of multispectral infrared detectors are relatively complex and have bulky components. They also require more complicated device fabrication leading to high cost and large scale systems.

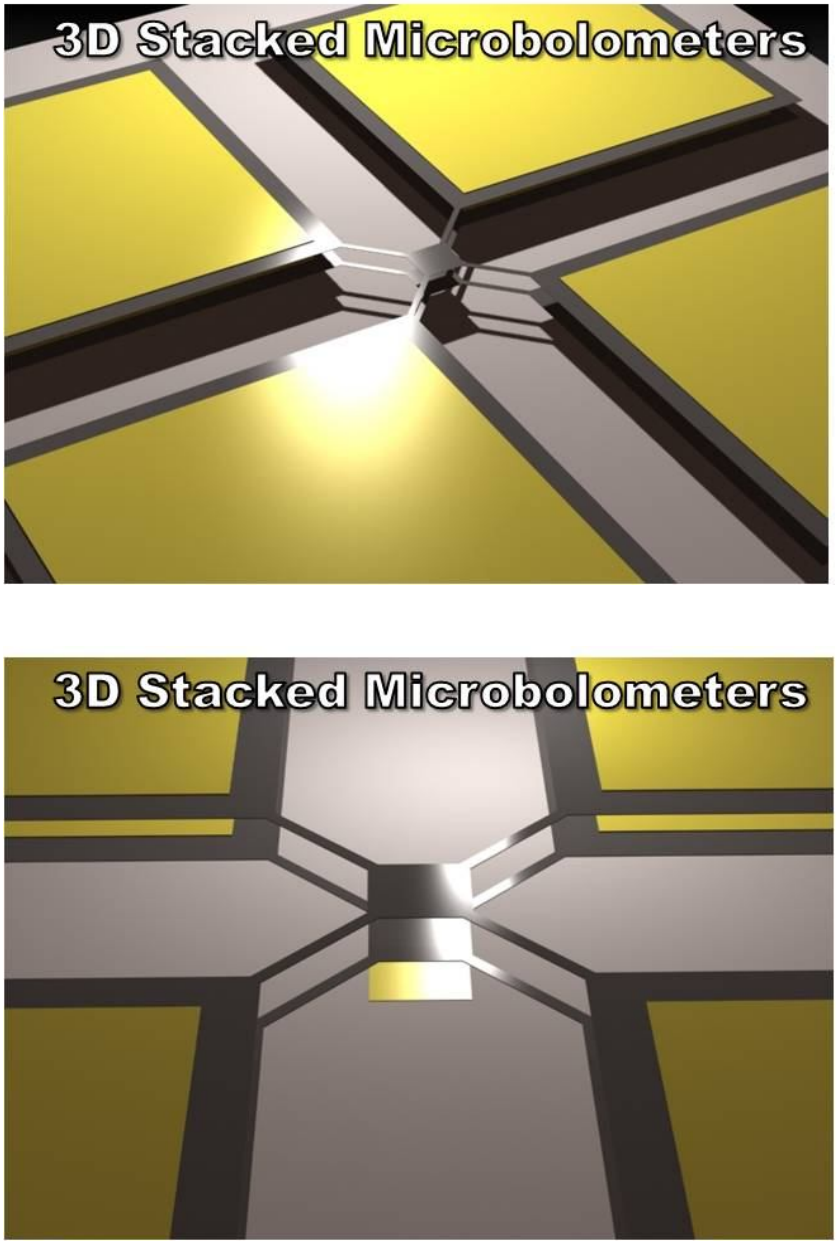

Figure 5.1: Illustration of Novel 3D stacked microbolometers.

5.2 REVIEW OF TWO COLOR UNCOOLED MICROBOLOMETERS

Recently, a few device concepts for achieving two color infrared using uncooled detector have been reported. One of the reported device concepts achieves two wavelengths responses by tuning the optical resonant cavity using switching MOEMS micro mirror between two positions, by an applied electrostatic actuation, as shown in Figure 5.2. However, currently none of the proposed device designs for two color uncooled microbolometer have been fabricated.

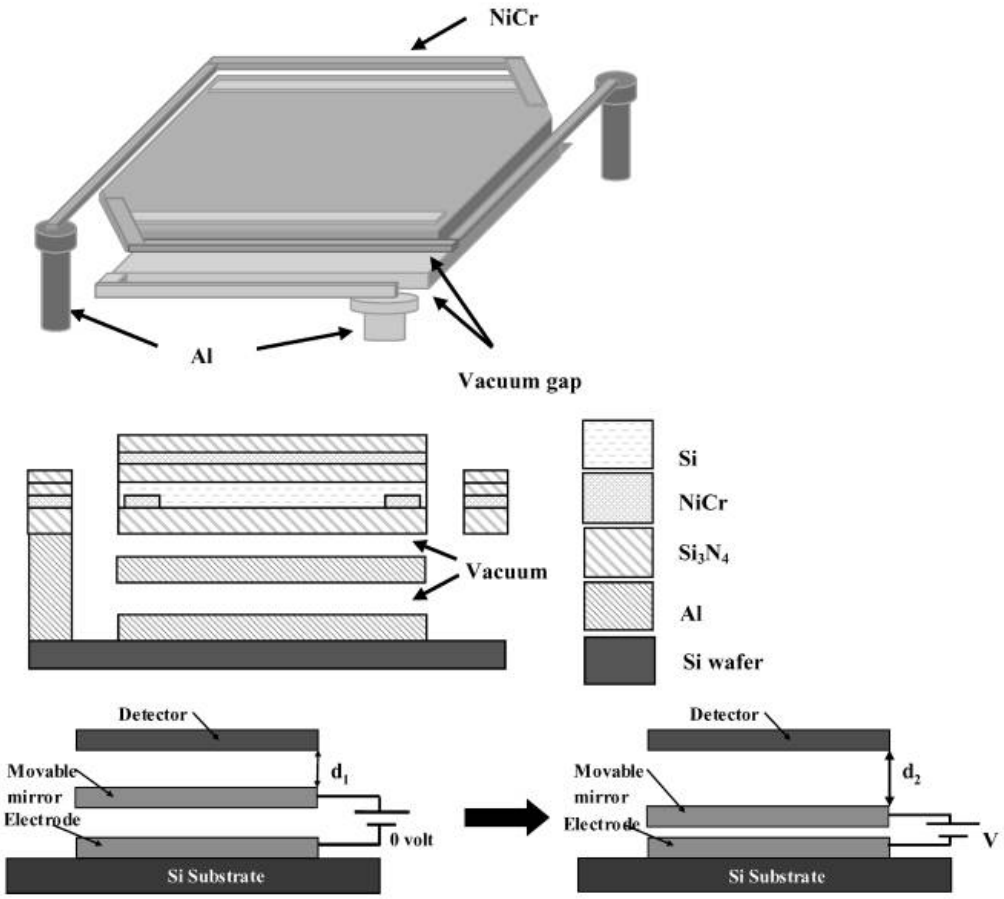

(a)

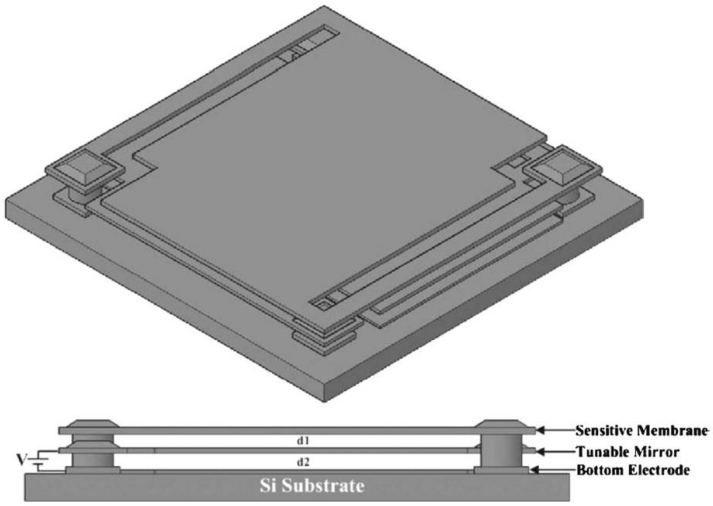

(b)

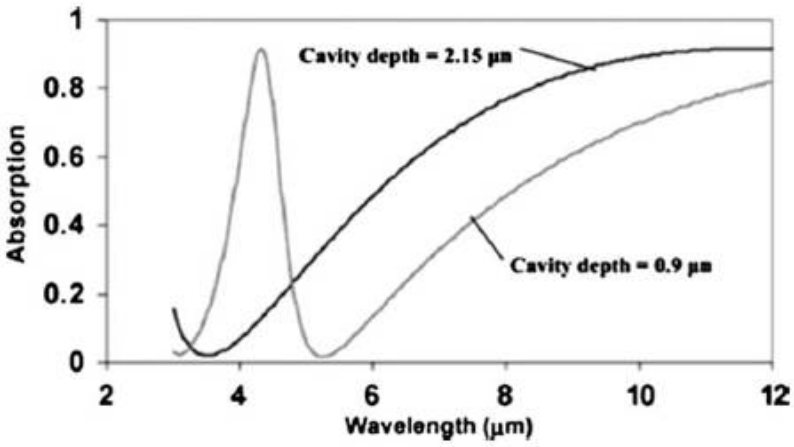

(c)

Figure 5.2: Design of two color microbolometer using tunable mirror actuation [30], [31]: (a) Amorphous type (b) Si3N4 type (c) Calculated absorption spectra.

Another proposed concept employs a smart material based infrared detector used for wavelength selectivity in the long wavelength infrared (LWIR) band. This design proposes a modification in the depth of the optical resonant cavity between the suspended thermistor material and a mirror on the substrate, using a smart mirror. This smart mirror

is made of VO_2, which has a phase transition from semiconductor to metallic state triggered at 68°C. This phase transition alters its optical and electrical as well as semiconductor material properties from the properties at room temperature. Before transition, VO2 is in the semiconducting phase and is transparent to infrared. As and when the temperature increases to 68°C, VO_2 undergoes phase transition and it reflects infrared in the metallic phase, effectively reducing the cavity gap. The calculated absorption coefficients in the dual bands were 59% and 65% respectively (Figure 5.3).

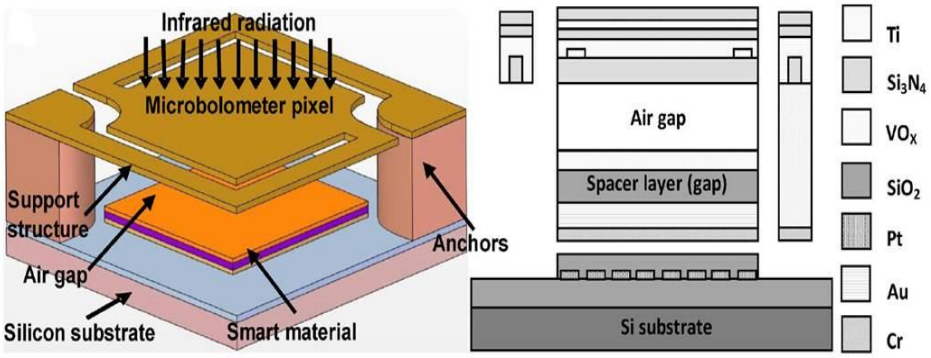

(a)

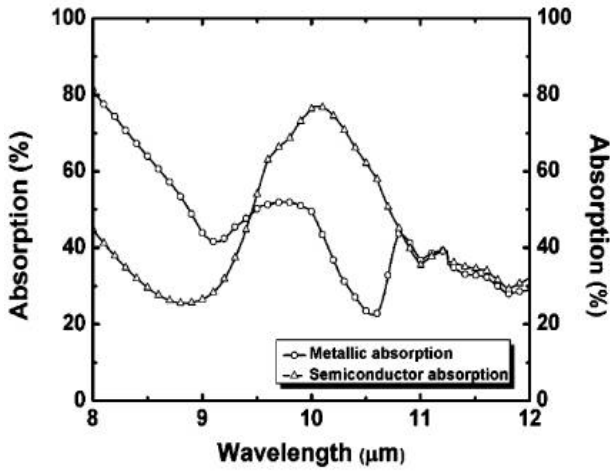

(b)

Figure 5.3: Design of dual band uncooled infrared microbolometer using smart mirror material [32]: (a) Schematic of device, (b) Calculated optical absorption.

5.3 Design of 3D Stacked Microbolometers for Two Color Infrared Detection

The 3D stacked microbolometer enables a separate spectral response for each targeted wavelengths, using dielectric coated Jaumann Absorber. Vertically stacked wavelength selective device pixels can save space and provide enhanced resolution compared to varying air gap based dielectric coated Salisbury screen microbolometer. This device consists of two Germanium dielectric structural layers, two resistive sheets as infrared absorber layers above each Germanium dielectric structural layer, two air gap spaces and a reflective mirror layer for enhanced infrared absorption power efficiency, as shown in Figure 5.4.

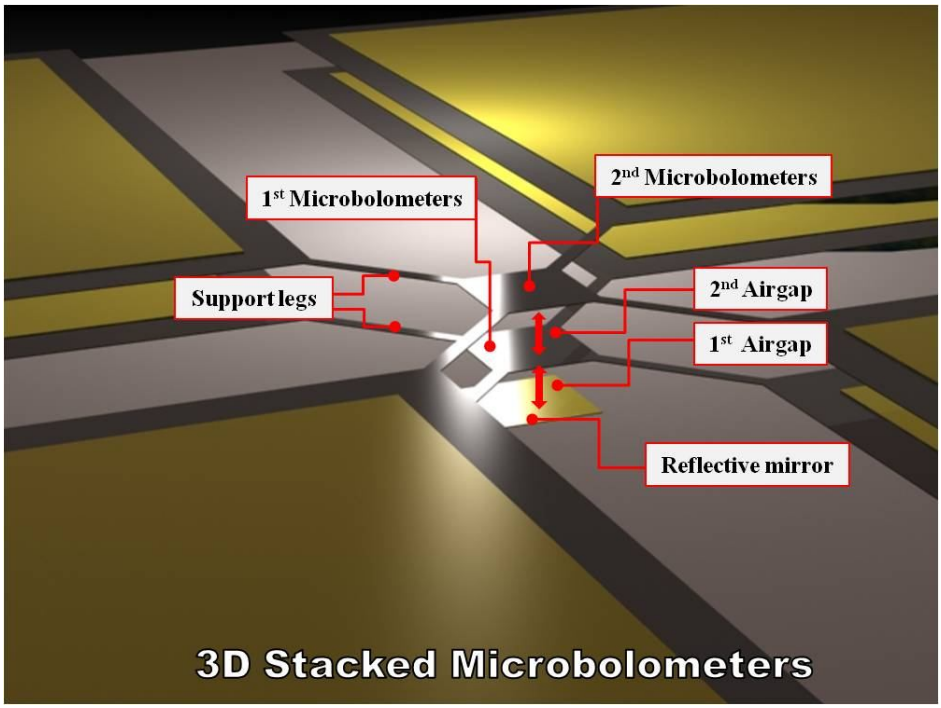

Figure 5.4: Illustration of configuration of 3D stacked microbolometers.

5.3.1 Two Color Wavelength Selectivity in Long Wavelength Infrared (LWIR)

The device design is approached such that each absorber layer in stacked microbolometer responds to the specific wavelength with narrow band absorption. Our group has set up design parameters such as sheet resistance of absorbers, thickness of Germanium dielectric structural layers, and air gap spaces.

Figure 5.5 shows the result of two color wavelength selectivity in long wave length infrared (LWIR). The design parameters are sheet resistance of top absorber layer: 1100Ω/□, thickness of top structural layer: 1.02μm, 2nd air gap: 2.0 μm, sheet resistance of bottom absorber layer: 2200Ω/□, thickness of bottom structural layer: 0.54μm and 1st air gap: 0.27 μm.

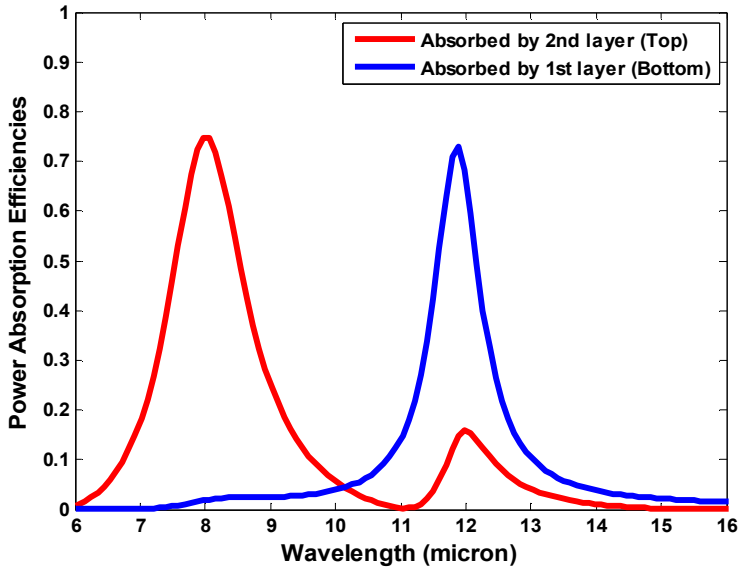

Figure 5.5: Design of two color wavelength selectivity in long wavelength infrared (LWIR: 8 μm and12 μm) region.

5.3.2 Variation of Two Color Spectral Responses with Sheet Resistance of Absorber

In this section, results of variation of two color spectral responses with sheet resistance as a parameter (from the results of section 5.2.1) are presented. Figure 5.6 shows simulation results of two color spectral response by doubling the sheet resistance of the 1st absorber. The design parameters are sheet resistance of top absorber layer: 2200Ω/□, thickness of top structural layer: 1.02μm, 2nd air gap: 2.0 μm, sheet resistance of bottom absorber layer: 2200Ω/□, thickness of bottom structural layer: 0.54μm and 1st air gap: 0.27 μm.

Figure 5.7 shows simulation result by halving the sheet resistance of the 2nd absorber. The design parameters are sheet resistance of top absorber layer: 2200Ω/□, thickness of top structural layer: 1.02μm, 2nd air gap: 2.0 μm, sheet resistance of bottom absorber layer: 1100Ω/□, thickness of bottom structural layer: 0.54μm and 1st air gap: 0.27 μm. Figure 5.8 shows the simulation result by now lowering the sheet resistance of 1st absorber. The design parameters are sheet resistance of top absorber layer: 550Ω/□, thickness of top structural layer: 1.02μm, 2nd air gap: 2.0 μm, sheet resistance of bottom absorber layer: 1100Ω/□, thickness of bottom structural layer: 0.54μm and 1st air gap: 0.27 μm.

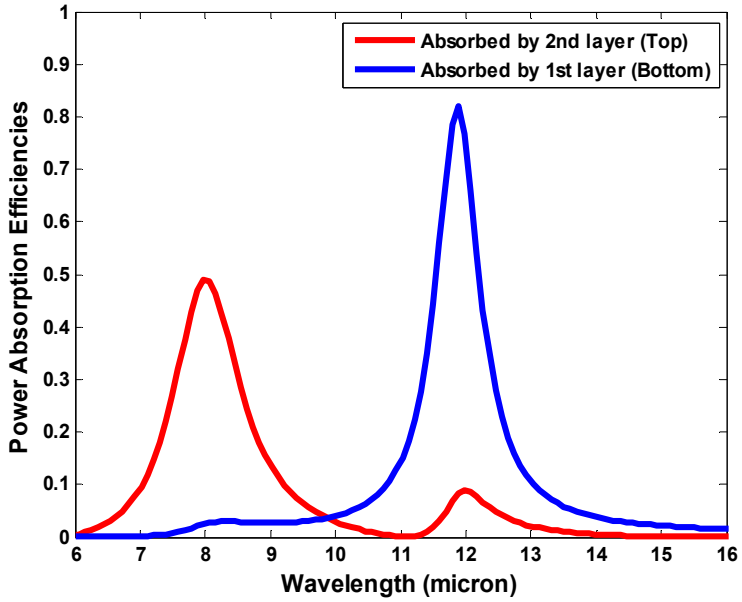

Figure 5.6: Variation of two color responses with sheet resistance of 1st absorber layer: 2200Ω/□.

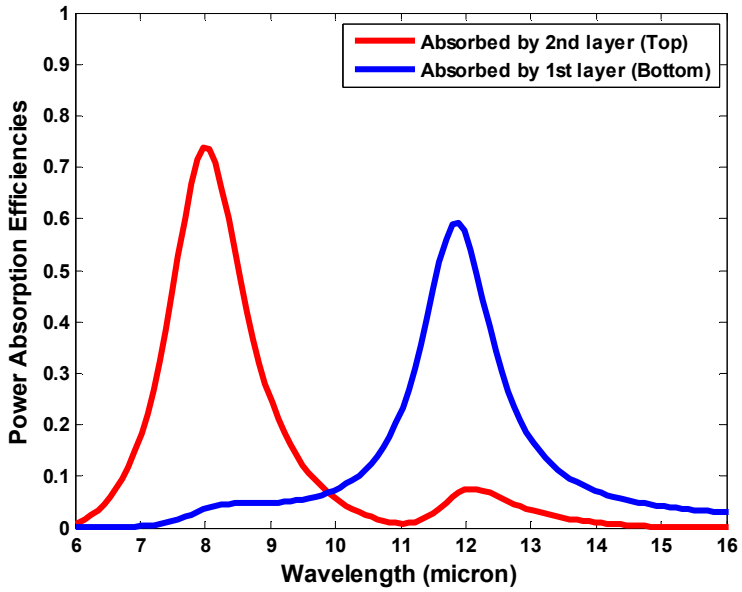

Figure 5.7: Variation of two color responses with sheet resistance of 2nd absorber layer: 1100Ω/□.

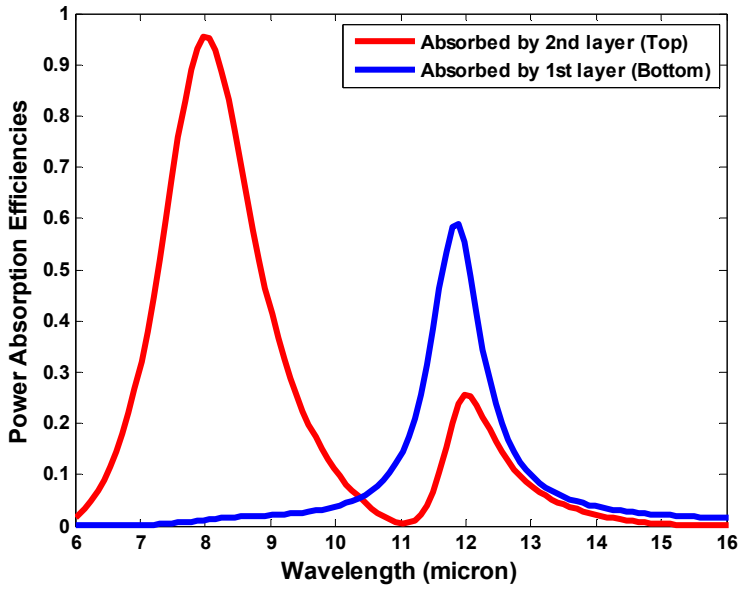

Figure 5.8: Variation of two color responses with relatively low sheet resistance of 1st absorber layer: 550Ω/□.

5.3.3 Variation of Two Color Spectral Responses with Air gap

In this section, results of variation of two color spectral responses with air gap as a parameter (from the results of section 5.2.1) are presented. Figure 5.9 shows simulation results of two color spectral responses by halving the space of the 2nd air gap. The design parameters are sheet resistance of top absorber layer: 1100Ω/□, thickness of top structural layer: 1.02μm, 2nd air gap: 1.0μm, sheet resistance of bottom absorber layer: 2200Ω/□, thickness of bottom structural layer: 0.54μm and 1st air gap: 0.27 μm. Figure 5.10 shows the simulation result, instead by increasing the space of the 2nd air gap. The design parameters are sheet resistance of top absorber layer: 1100Ω/□, thickness of top structural

layer: 1.02μm, 2nd air gap: 3.0 μm, sheet resistance of bottom absorber layer: 2200Ω/□, thickness of bottom structural layer: 0.54μm and 1st air gap: 0.27 μm.

Figure 5.11 shows simulation result by changing both the spaces of the 1st and 2nd air gaps. The design parameters are sheet resistance of top absorber layer: 1100Ω/□, thickness of top structural layer: 1.02μm, 2nd air gap: 3.0 μm, sheet resistance of bottom absorber layer: 2200Ω/□, thickness of bottom structural layer: 0.54μm and 1st air gap: 0.54 μm.

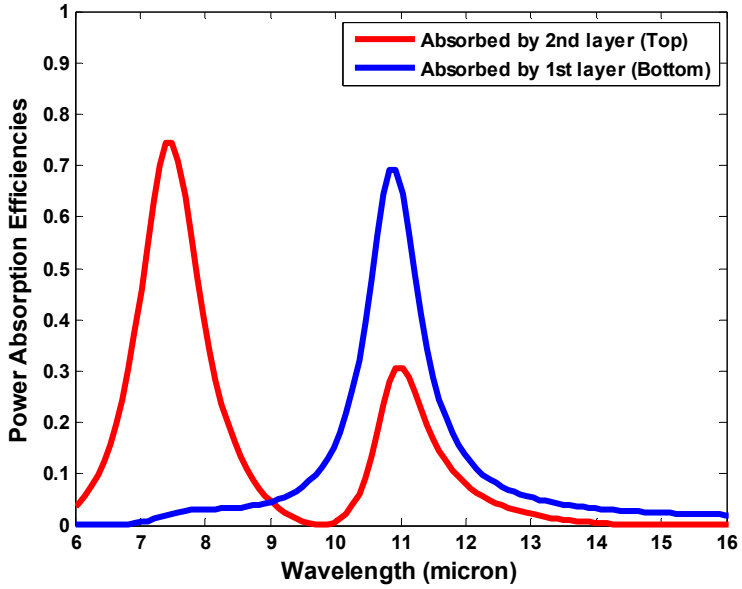

Figure 5.9: Variation of two color responses with space of 2nd air gap: 1.0μm.

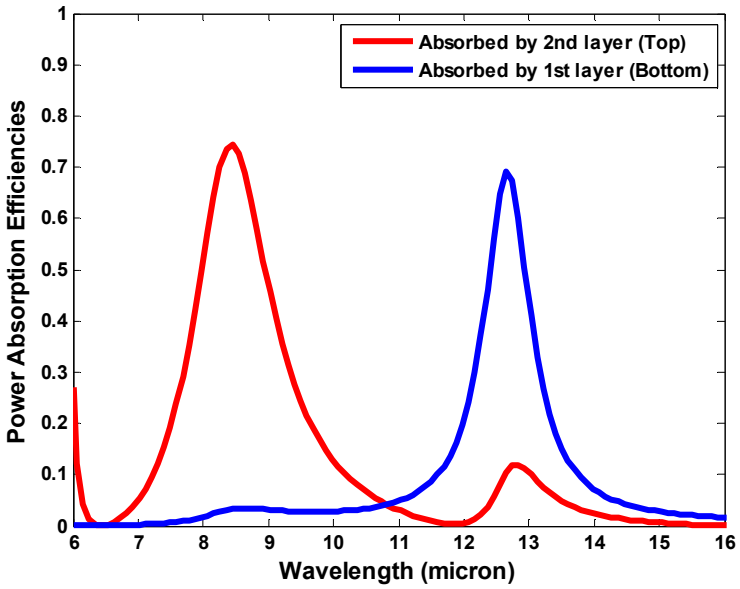

Figure 5.10: Variation of two color responses with space of 2nd air gap: 3.0μm.

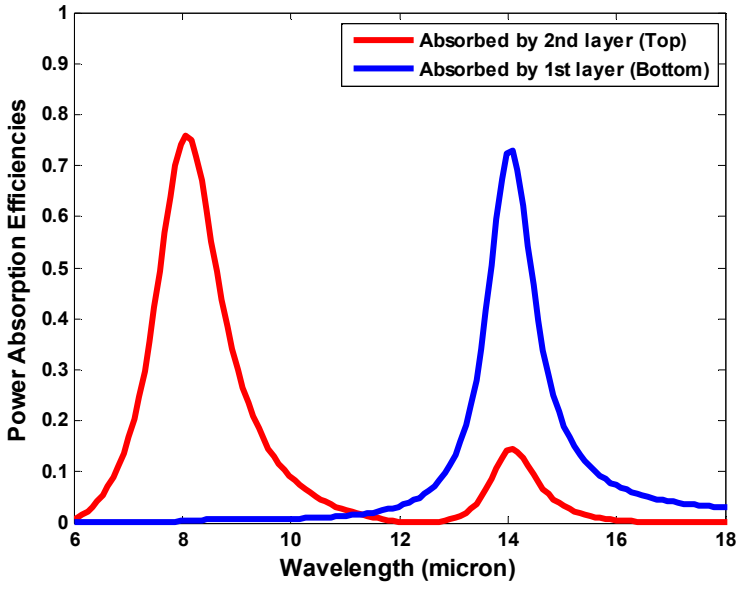

Figure 5.11: Variation of two color responses by changing the space of both 1st and 2nd air gap: 0.54μm, 3.0μm respectively.

5.3.4 Two Color Spectral Responses with Experimental Parameters

In this section, simulation results using experimental parameters are discussed. The design parameters are extracted from a fully fabricated device, previously discussed in Chapter 3, namely the Wavelength selective Germanium dielectric Salisbury screen microbolometer. The design parameters are sheet resistance of top absorber layer: 1100Ω/□, thickness of top structural layer: 1.02μm, 2nd air gap: 3.0 μm, sheet resistance of bottom absorber layer: 2200Ω/□, thickness of bottom structural layer: 0.54μm and 1st air gap: 1.0 μm. These results are shown in Figure 5.12. Figure 5.13 shows the result with design parameters of sheet resistance of top absorber layer: 1100Ω/□, thickness of each structural layer: 0.6μm, 2nd air gap: 5.0 μm, sheet resistance of bottom absorber layer: 1000Ω/□ and 1st air gap: 2.0 μm.

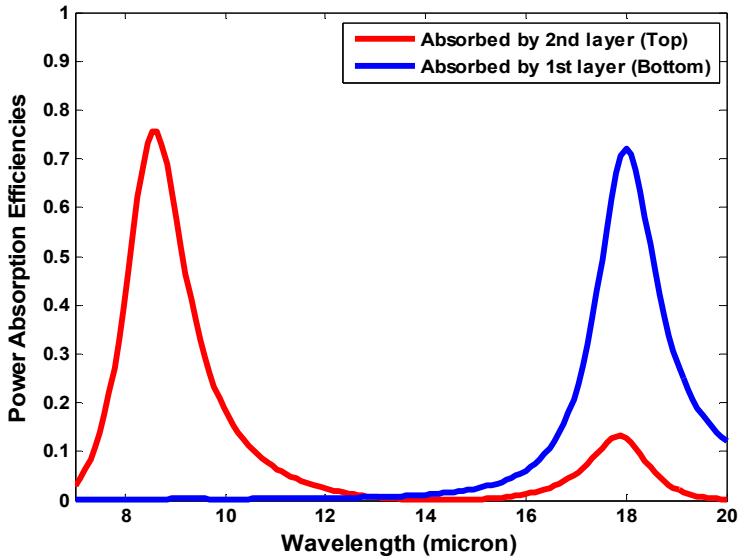

Figure 5.12: Two color spectral responses using experimental parameters: Space of air gap (1st air gap: 1.0 μm, 2nd air gap: 3.0 μm).

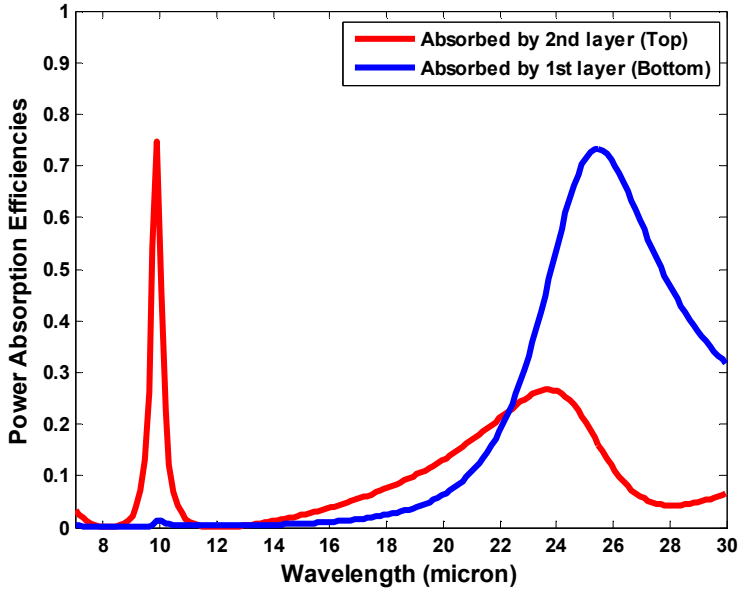

Figure 5.13: Two color spectral responses using experimental parameters: Thickness of Germanium structural layer (1st Ge structure: 0.6 µm, 2nd Ge structure: 0.6 µm), space of air gap (1st air gap: 2.0 µm, 2nd air gap: 5.0 µm).

5.4 DEMONSTRATION OF 3D STACKED MICROBOLOMETER FABRICATION

We demonstrate a feasible fabrication of the novel 3D stacked uncooled microbolometers using self-alignment process. The fabricated devices have different active area, leg lengths and widths. This device enables two color narrow band infrared power absorption. The simulation results show efficient two color infrared detection using vertically stacked infrared absorber layers. This design also promises to produce tunable narrowband absorption in the mid-wave infrared (MWIR) and long-wave infrared (LWIR) spectral region.

Two Germanium structural layers have been adopted above the two polyimide sacrificial layers, instead of silicon nitride structural layer as in conventional

microbolometers. This design uses the same materials as the ones used in wavelength selective Germanium dielectric coated Salisbury screen microbolometer, previously discussed in Chapter 3. By using Germanium as both the interference layer for wavelength selectivity and the structural layer, the problems associated with highly infrared absorbing and dispersive silicon nitride layers can be avoided. To form the thermally isolated free-standing device structure in uncooled microbolometers, most commonly used microfabrication methods employs a high-temperature stable polyimide as the sacrificial layer, with patterning process. We use a self-aligned process without a polyimide patterning process, which helps eliminate deformation and stress in the two infrared absorbers/structural membranes and leads to cost effective device fabrication due to reduced fabrication process flow.

Briefly, the fabrication process starts with infrared reflective mirror layer formation. Second step in the process is the formation of the 1^{st} sacrificial layer. Third step is the formation of 1^{st} Germanium structure layer. Fourth step is the formation of 1^{st} absorber layer. Fifth step is the formation of 2^{nd} sacrificial layer. Sixth step is the formation of 2^{nd} Germanium structure layer. Seventh step is the formation of 2^{nd} absorber layer. Finally, the sacrificial layer is then removed, to form the air gap below the two structural layers. Figures 5.14 and 5.15 show the first feasible demonstration of fabricated 3D stacked microbolometer devices.

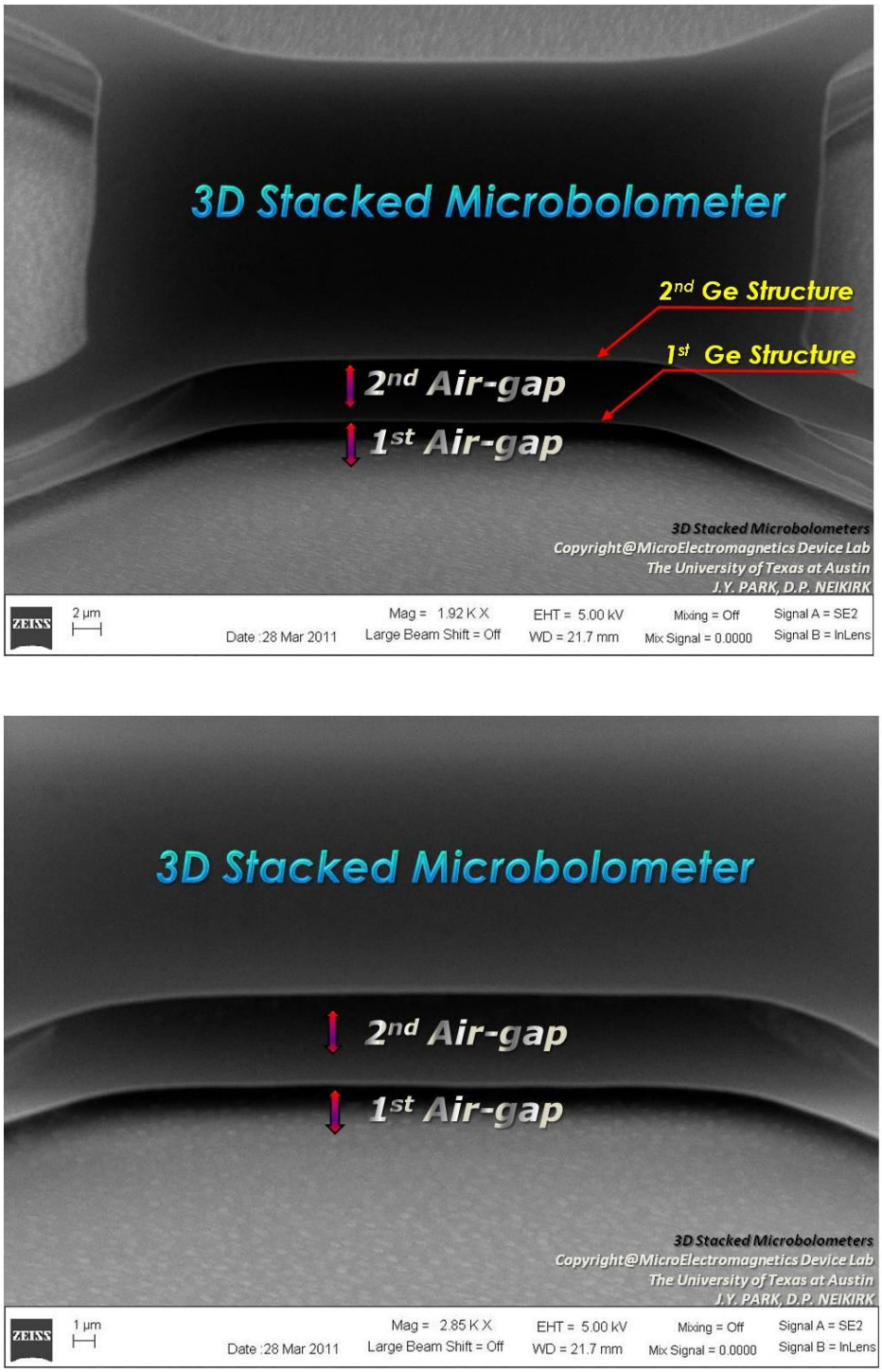

Figure 5.14: SEM images of demonstrated 3D stacked microbolometers.

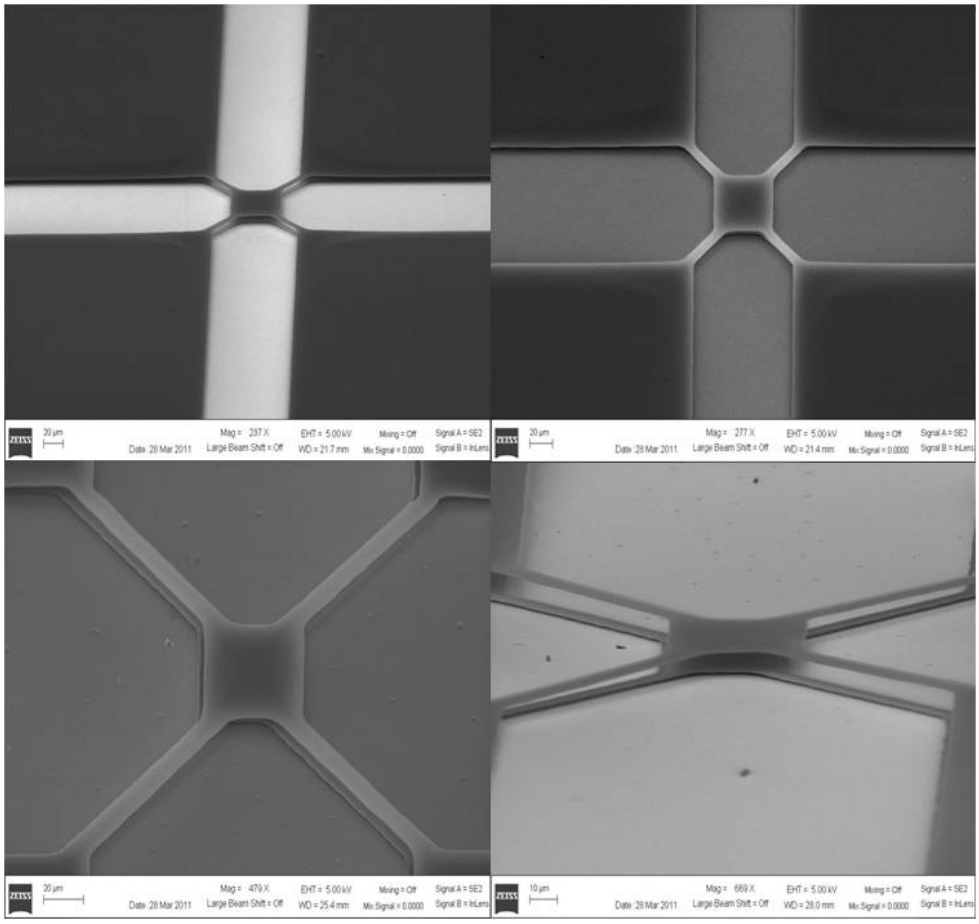

Figure 5.15: SEM images of fabricated 3D stacked microbolometers with different active areas, leg lengths and widths.

Chapter 6: Conclusions

A study of fabrication and characterization of wavelength selective Germanium dielectric coated Salisbury screen and novel 3D stacked microbolometer, for multispectral infrared detection, has been presented in this work.

Wavelength selective Germanium dielectric coated Salisbury screen microbolometer using self aligned process has been demonstrated. The fabricated device consists of a metal resistive sheet of 400Ω/□ as an infrared absorber layer, dielectric structural layer, reflective mirror layer and electrical contact pads. Dielectric Germanium was used as structure/interference layer. Devices have been fabricated with different microbolometer active areas, leg lengths and widths, and different metallic absorber layer materials (Ni, Ti, Cr, and TaN).

The novel fabrication process leads to a flat and robust device structure. This is achieved by using an un-patterned sacrificial layer to produce device legs that hold the central structural layer above the reflective mirror supported by a completely flat sacrificial layer with sufficient thermal isolation to allow microbolometer operation.

To characterize the spectral response of the wavelength selective Germanium dielectric Salisbury screen microbolometer using self align process, Fourier transform infrared (FTIR) microscopy measurements were taken on a number of the fabricated devices using Nicolet ^{TM} 6700 FTIR spectrometer. The FTIR measured spectral responses and numerical simulation results show excellent agreement with wavelength selectivity (9μm, 10μm, 11μm) in long wave infrared (LWIR) region. Electrical measurements were also performed, including IV curve, RP plot, thermal impedance and Temperature Coefficient of Resistance (TCR).

Recently, a few device concepts for achieving multicolor infrared detection using uncooled detector have been reported. However, currently none of the proposed device designs for the two color uncooled microbolometer have been fabricated. Moreover, commercial Fabry-perot resonant cavity based uncooled microbolometers (Air gap: 2 to 2.5μm) have limited design parameters due to multicolor narrow band spectral response.

In this study, a feasible device fabrication method for novel 3D stacked microbolometer is demonstrated for multispectral uncooled infrared detector that can achieve tunable narrowband absorption in mid-wave infrared (MWIR) and long-wave infrared (LWIR) spectral regions.

The 3D stacked microbolometer enables a separate spectral response for each of the targeted wavelengths, using dielectric coated Jaumann Absorber. Vertically stacked wavelength selective device pixels can save space and provide enhanced resolution compared to varying air gap based dielectric coated Salisbury screen microbolometers. This device consists of two Germanium dielectric structural layers, two resistive sheets as infrared absorber layers above each Germanium dielectric structural layer, two air gap spaces and a reflective mirror layer for enhanced infrared absorption power efficiency.

Based on experimentally extracted parameters from the fabricated 3D stacked microbolometer devices, numerical simulations for spectral responses have been performed showing two color infrared selectivity. The experimental parameters used in this study are the two air gap spaces, sheet resistance of the two absorber layers and thicknesses of the structural layers.

Possible directions for future work include packaging of wavelength selective Germanium dielectric coated Salisbury screen microbolometers.

Another possibility for future work is the application of novel absorber materials that can lead to enhanced infrared power absorption in the microbolometer. Developmental studies of carbon nanomaterials, such as Graphene or its compounds, can be performed as possible candidates for absorber materials.

One of future developments would be optimizing the novel 3D stacked microbolometers fabrication for multispectral infrared detection. The 3D stacked microbolometer is a useful approach to two color uncooled infrared detectors. Further study of the 3D stacked microbolometer presented here will hopefully provide guidance for novel uncooled multispectral infrared detectors.

Bibliography

[1] E.L. Dereniak, G.D. Boreman, Infrared Detectors and Systems, John Wiley and Sons, 1996.

[2]A. Rogalski, "Novel uncooled infrared detectors",Opto-Electronics Review 18(4),478-492, 2010.

[3] P.W. Kruse, D.D. Skatrud (Eds.), Uncooled Infrared Imaging Arrays and Systems, Semiconductors and Semimetals, vol. 47, Academic Press, New York, 1997.

[4] A. Rogalski, Infrared Detectors, Electrocomponent Science Monographs, Gordon and Breach Science Publishers, 2000.

[5]C.D. Tran, "Infrared Multispectral Imaging: Principles and Instrumentation", Applied spectroscopy reviews, Vol. 38, No. 2, pp. 133–153, 2003

[6] W. Herschel, "Experiments on the refrangibility of the invisible rays of the sun," Philo-sophical Transactions of the Royal Society of London, vol. 90, pp. 284–293, 1800.

[7] "Infrared." Wikipedia, 2005. http://en.wikipedia.org/wiki/Infrared.

[8] R.D.Hudson, Infrared System Engineering, Wiley, New York .1969.

[9] http://www.vision-systems.com/articles.

[10] http://www.flir.com.

[11] http://www.microsystems.metu.edu.tr/bolometer/bolometer.html

[12]R.A. Wood, "Uncooled Thermal Imaging with Monolithic Silicon Focal Arrays," Infrared Technology XIX, Proc. SPIE Vol. 2020, 322-329, 1993.

[13]B.E. Cole, R.E. Higashi, R.A. Wood, Monolithic arrays of micromachined pixels for infrared application Tech. Digest, in: IEEE Int. Electron Devices Meet, 459–462,1998.

[14]A.Rogalski, “Infrared detectors for the future”, Acta Physica Polonica A, Vol 116, 2009.

[15] A.Rogalski, “Infrared detectors: an overview”, Infrared physics & Technology 43, 2002.

[16]http://www.photonics.com

[17]T. Maier, H. Brueckl, ”Multispectral microbolometers for the midinfrared”, OPTICS LETTERS,Vol. 35, No. 22, 2010

[18]M. Sundaram, A.Reisinger, R. Dennis, K. Patnaude, D. Burrows, R. Cook, J. Bundas,” Multi-color IR sensors based on QWIP technology for security and surveillance applications”, Proc. of SPIE Vol. 6203, 620307, 2006.

[19] A. Rogalski, Infrared Detectors, second ed., CRC Press, 2010.

[20]S. V. Bandara; S. D. Gunapala; J. K. Liu; S. B. Rafol; C. A. Shott, “Multi-Band GaAs/AlGaAs Quantum Well Infrared Photodetector (QWIP) Focal Plane Arrays” JPL, 2002.

[21] George M. Williams, A. Barter, “Dual-Band MWIR/LWIR Radiometer for Absolute Temperature Measurements”, Proc. of SPIE Vol. 6205,62050M, 2006.

[22] X. Lu1, J. Vaillancourt, M. J. Meisner,” An Electrically-Controllable Multi-spectral Quantum Dot Infrared Photodetectorwith high Photodetectivity, Proc. of SPIE Vol. 6542, 65420Q, 2007.

[23] HD Microsystems PI-2610, PI-2611 product bulletin, 2008.

[24] United States Patent 4,521,442 Radiant Energy Collector Having Plasma-Textured Polyimide Exposed Surface.

[25]Kawka, P. A. and R. O. Buckius, "Optical Properties of Polyimide Films in the Infrared," International Journal of Thermo physics, 22:2, 517-534, 2002.

[26] J. Y. Park, J. Y. Jung, Dean P. Neikirk, A. S.Weling, William T. Hafer, J. H. Goldie, and P. D.Willson, "Fabrication of Wavelength Selective Germanium Dielectric Supported Microbolometers", Proc. SPIE Vol.7660, 76601C, 2010.

[27] J.Tonotani, S. Ohmi, H Iwai, "Dry etching of Cr2O3/Cr stacked film during resist ashing by oxygen plasma", JJAP, Vol44, no 1A, 114-117, 2005.

[28] J. Y. Park, James E. Gardner, P. Pasupathy, J. W. Suk, R. S. Ruoff, Dean P. Neikirk, "Fabrication and Characterization of Wavelength Selective Microbolometers using a Planar Self-aligned Process for Low Deformation Membranes", Proc. SPIE Vol.8252, 782520Y, 2012.

[29]T.Lee, K. Watson, F. Chen, J.Gill, D. Harmon, T. Sullivan, B.Li, " Characterization and reliability of TaN film resistors", IEEE 04CH37533, International Reliability Physics Symposium, 2004.

[30]Y. Gong, W. Li, H. Cai, Y. Jiang, "Uncooled infrared detection with two-color microbolometers using micro optoelectromechanical systems tunable micromirror", J.Micro/Nanolitho, MEMS MOEMS 9(3), 031005,2010

[31]M. Almasri, "Amorphous silicon two-color microbolometer for uncooled IR detection", IEEE Sensors Journal, Vol 6, No.2, 2006.

[32]Q. Cheng, S. Paradis, T. Bui, M. Almasri, "Design of dual-band uncooled infrared microbolometer", IEEE Sensors Journal, Vol 11, No.1, 2011.